

Development of capacitive deionisation electrodes: optimization of fabrication methods and composition

By

Nafeesah Smith

A thesis submitted in compliance of the requirements for the degree of Magister Scientiae in the Department of Chemistry, South African Institute for Advanced Material Chemistry, University of Western Cape.

Supervisor: Prof Bernard Bladergroen

Co-Supervisor: Mr Bongibethu Hlabano-Moyo

November 2019

Keywords

Activated Carbon

Adsorption

Binder

Carbon Black

Conductivity

Contact Angle

Desalination

Desorption

Electrode

Maximum Salt Adsorption Capacity

Membrane Capacitive Deionisation

Surface Area

Abstract

Membrane Capacitive Deionisation (MCDI) is a technology used to desalinate water where a potential is applied to an electrode made of carbonaceous materials resulting in ion adsorption. Processes and materials for the production of electrodes to be applied in Membrane Capacitive Deionisation processes were investigated. The optimal electrode composition and synthesis approached was determined through analysis of the salt removal capacity and the rate at which the electrodes absorb and desorb ions. To determine the conductivity of these electrodes, the four point probe method was used. Contact angle measurements were performed to determine the hydrophilic nature of the electrodes. N₂ adsorption was done in order to determine the surface area of carbonaceous materials as well as electrodes fabricated in this study. Scanning electron microscopy was utilised to investigate the morphology.

Electrodes were produced with a range of research variables; (i) three different methods; slurry infiltration by calendaring, infiltration ink dropwise and spray-coating, (ii) electrodes with two different active material/binder ratios and a constant conductive additive ratio were produced in order to find the optimum, (iii) two different commercially available activated carbon materials were used in this study (YP50F and YP80F), (iv) two different commercially available electrode substrates were utilised (JNT45 and SGDL), (v) different slurry mixing times were investigated showing the importance of mixing, and (vi) samples were treated at three different temperatures to establish the optimal drying conditions.

Through optimization of the various parameters, the maximum adsorption capacity of the electrode was incrementally increased by 36 %, from 16 mg·g⁻¹ at the start of the thesis to 25 mg·g⁻¹ at the end of the study.

Declaration

Name: Nafeesah Smith

Student number: 3341530

I, Nafeesah Smith, declare that “Development of capacitive deionisation electrodes: optimization of fabrication methods and composition” is my own work, that it has not been submitted for any degree or examination in any other university, and that all the sources I have used or quoted have been indicated and acknowledged by complete references.

A handwritten signature in black ink, appearing to read 'Nafeesah Smith', written over a horizontal dashed line.

Signature

22-11-2019

Date

Acknowledgements

Firstly, I would like to express my gratitude to the Almighty God for granting me the strength and knowledge throughout my educational journey.

It is with profound gratitude and appreciation that I acknowledge my mother for her undying support and encouragement throughout my academic career. Also, to my father, the silent operator, who would at times push me in the right direction spiritually and otherwise. To the rest of family and friends, thank you for all the love, prayers, reassurance and support throughout my educational journey.

To my supervisor, Professor Bernard Bladergroen and co-supervisor Mr. Bongibethu Hlabano-Moyo, thank you for allowing me the opportunity to further my education under your exceptional supervision, for all your support and reassurance throughout my 2-year journey at the South African Institute for Advanced Materials Chemistry (SAIAMC).

To my fellow students, who I have befriended, and all staff members at SAIAMC, thank you for all your assistance, guidance and support.

I would like to acknowledge the National Research Foundation (NRF) and Water Research Commission (WRC) for financially supporting my academic journey for the past two years.

To Ms Hanlie Botha from Stellenbosch University (SU) and Dr. Xandri van Niekerk from the Nelson Mandela University (NMU) for assisting with BET analysis.

Thank you to Dr. Ebrahiem Botha at SAIAMC for assisting with the results obtained in this study and Dr. Cummings at the Electron Microscope Unit (EMU) University of the Western Cape (UWC) for assisting me with Scanning Electron Microscopy (SEM).

Abbreviations

AC	Activated carbon
AEM	Anion Exchange Material
ASAR	Average Salt Adsorption Rate
BET	Brunauer Emmet Teller
BM	Batch Mode
CB	Carbon Black
CC	Constant Current
CDI	Capacitive Deionisation
CEM	Cation Exchange Material
CNTs	Carbon Nanotubes
CV	Constant Voltage
N,N-DMAC	N,N-Dimethylacetamide
ED	Electrodialysis
EDLC	Electric Double Layer Capacitor
HDPE	High Density Polyethylene
HT	High temperature (130 ± 5 °C)
IEM	Ion Exchange Material/Membrane
IE	Ion Exchange
IID	Infiltration Ink Dropwise
MCDI	Membrane Capacitive Deionisation
MED	Multi-Effect Distillation
mSAC	Maximum Salt Adsorption Capacity
NF	Nanofiltration
PET	Polyethylene Terephthalate
PSD	Pore Size Distribution
PVC	Polyvinyl chloride
PVDF	Polyvinylidene Fluoride
RO	Reverse Osmosis
RT	Room Temperature (25 ± 5 °C)
SC	Spray-coating
SIC	Slurry Infiltration
SSA	Specific Surface Area
SAIAMC	South African Institute of Advanced Material Chemistry
SAC	Salt Adsorption Capacity
SP	Single Pass
TDS	Total Dissolved Solids

Contents

Keywords.....	i
Abstract	ii
Declaration.....	iii
Acknowledgements.....	iv
Abbreviations.....	v
Contents.....	vi
List of Figures.....	ix
List if Tables.....	xii
1 Introduction.....	1
1.1 Background and motivation: Sustainable water supply	1
1.2 Increased worldwide water consumption and scarcity	1
1.2.1 Population growth.....	2
1.2.2 Improve human development index.....	2
1.2.3 Industrial activities require water	3
1.3 Change in water supply	3
1.3.1 Impact of industrial pollution on the supply of high quality water	3
1.3.2 Global warming, climate change and its impact on fresh water accessibility.....	4
1.3.3 Water crisis in Cape Town.....	5
1.4 Desalination as a means to meet the demand for adequate quality water.....	6
1.5 Problem statement and the challenge going forward.....	8
2 Literature Review	9
2.1 Types of desalination	9
2.1.1 Thermally driven desalination processes	10
2.1.2 Pressure driven desalination processes	11
2.1.3 Ion-exchange desalination process	14
2.1.4 Electrically driven desalination processes.....	15

2.2	Energy requirements for water desalination and its cost	17
2.3	Capacitive Deionisation	23
2.3.1	CDI history	23
2.3.2	Electrical double layer theory.....	23
2.3.3	Electrode materials.....	25
2.3.4	Operational considerations	28
2.3.5	CDI applications	37
2.3.6	Summary of literature review	38
2.4	Research aims and objectives	39
3	Experimental Methods.....	41
3.1	Electrode production	41
3.1.1	Ink preparation.....	41
3.1.2	Electrode substrates	44
3.1.3	Ink deposition techniques.....	44
3.1.4	Electrode samples	46
3.1.5	Thermal treatment of electrodes	47
3.2	Electrode characterisation	48
3.2.1	Electrode conductivity	48
3.2.2	Contact angle measurements	50
3.2.3	Specific surface area N ₂ adsorption	52
3.2.4	Scanning electron microscopy.....	53
3.2.5	Membrane Capacitive Deionisation Cell Design, Description and Desalination Performance	54
4	Results and Discussion	60
4.1	Electrode Production.....	60
4.1.1	Samples produced.....	60
4.1.2	Thermal treatment of electrodes	62

4.2	Characterisation of electrodes	63
4.2.1	Electrode conductivity	63
4.2.2	Contact angle measurements	65
4.2.3	Specific surface area N ₂ adsorption	68
4.2.4	Scanning electron microscopy.....	75
4.2.5	Electrode salt removal performance	77
5	Conclusion and Future Work.....	84
5.1	Conclusion.....	84
5.2	Future Works	87
6	Bibliography	88
	Appendix A.....	106
	Appendix B.....	107
	Appendix C.....	108
	Appendix D.....	109
	Appendix E.....	110

List of Figures

Figure 1.1: Water usage for high-income and developing countries ⁷	2
Figure 1.2: Volume of freshwater resources for each continent ¹⁸	4
Figure 1.3: Sand and dead tree trunks in a nearly empty reservoir near Cape Town ³⁰	6
Figure 2.1: Percentage of membrane and thermal desalination plants worldwide ⁷ . ED: Electrodialysis, RO: Reverse osmosis, MED: Multiple-effect Distillation, MVC: Mechanical Vapour Compression, MSF: Multi-stage Flash	9
Figure 2.2: Percentage of membrane and thermal desalination plants worldwide and percentage of processed water. MGD: million gallons per day ⁷	9
Figure 2.3: MED Principle ⁵⁴	10
Figure 2.4: MSF Principle ⁵⁴	11
Figure 2.5: RO Diagram ⁵⁸	12
Figure 2.6: How Nanofiltration works ⁶³	13
Figure 2.7: Ion Exchange system ⁷²	14
Figure 2.8: ED Principle ⁵²	16
Figure 2.9: Illustration of CDI device ³⁹	17
Figure 2.10: SWRO desalination plant energy breakdown ⁸⁰	18
Figure 2.11: SWRO desalination CAPEX breakdown ⁹⁵	22
Figure 2.12: Schematic of ion adsorption coupled with ion transport theory in CDI ¹⁰⁷	24
Figure 2.13: Charge distribution in Gouy-Chapman-Stern model ¹⁰⁸	25
Figure 2.14: (A)–(C) CDI architectures using static electrodes, including: (A) flow between electrodes, (B) flow-through electrode and (C) membrane CDI ¹²²	29
Figure 2.15: Schematic of FCDI process ¹⁰⁵	30
Figure 2.16: CDI architectures with flow electrodes, including systems with (D) feed-in electrodes, (E) feed-between electrodes, and (F) membrane flow electrode CDI ¹²²	31
Figure 2.17: A wire-CDI cell ³⁸	32
Figure 2.18: Schematic of desalination process with wires ¹²¹	32
Figure 2.19: Schematic of CDI experimental design ¹⁰⁹	33
Figure 2.20: Comparison of salt adsorption and charge per cycle, and charge efficiency for CDI and MCDI with different CV operational modes ¹⁰⁹	35
Figure 2.21: Effluent salt concentration for CC-mode of CDI and MCDI ¹⁰⁹	36
Figure 2.22: Capacitive and Faradaic processes ¹⁰⁷	37

Figure 2.23: Large scale CDI desalination modules in China ⁴¹	38
Figure 3.1: Holder for slurry preparation and devil shaker	43
Figure 3.2: Slurry infiltration using the rolling press.....	44
Figure 3.3: SONO-TEK spray coating machine	45
Figure 3.4: Infiltration ink dropwise	46
Figure 3.5: Furnace used for thermal treatment.....	48
Figure 3.6: (A) Image of four point probe setup (1) multimeter, (2) four-point probe. (B) Close up illustrating the (1) outer probes, (2) inner probes and (3) the electrode	50
Figure 3.7: Image of in-house contact angle setup	51
Figure 3.8: Contact angle measurements of electrode E24.....	52
Figure 3.9: A detailed overview of the Membrane Capacitive Deionisation cell ¹⁶³	54
Figure 3.10: Image of MCDI setup ¹⁶³	56
Figure 3.11: Kim-Yoon Plot for ASAR vs SAC ⁴¹	59
Figure 4.1: SC electrode (A) front and (B) back	61
Figure 4.2: SIC electrode (A) front and (B) back	61
Figure 4.3: IID ^{RT} electrode (A) front and (B) back	61
Figure 4.4: Infiltration ink dropwise electrode at 25 ± 5 °C.....	62
Figure 4.5: Figure 4.4: Improved Infiltration ink dropwise electrode at 25 ± 5 °C.....	62
Figure 4.6: TGA Analysis of an electrode having an 80:10:10 composition.....	62
Figure 4.7: Contact angle measurements of E23-E25.....	67
Figure 4.8: Isotherms of (A) AC-YP50F and (B) AC-YP80F	69
Figure 4.9: BJH pore size distribution for differently prepared electrodes.....	70
Figure 4.10: BJH pore size distribution for E21 and E23	74
Figure 4.11: SEM images of pure (A) AC-YP80F, (B) CB, (C) PVDF powders and (D) JNT45 substrate	75
Figure 4.12: SEM images of (A) AC-YP80F with an empty cavity and (B) AC and CB 60 min dry mixture with CB sitting inside a cavity of AC	76
Figure 4.13: SEM images of (A) SIC electrode and (B) IID electrode.....	76
Figure 4.14: SEM images showing the cavities in (A) SIC and (B) IID electrodes.....	77
Figure 4.15: Conductivity and current graph vs time for E1.....	78
Figure 4.16: mSAC values of electrodes having different slurry mixing times	81
Figure 4.17: mSAC values of electrodes with different thermal treatment temperatures.....	81

Figure 4.18: Conductivity vs time graph for electrodes having different thermal treatment temperatures	82
Figure 4.19: Kim-Yoon plot for E21	83

List of Tables

Table 1.1: Salinity status classifications ³³	7
Table 2.1: Comparison of different desalination processes, modified from ⁵²	19
Table 2.2: Capital and operating cost of MCDI ⁹²	20
Table 2.3: Capital and operating cost of RO with a capacity of 1ML per day ⁹⁴	22
Table 3.1: Slurry/ink composition and amount of material utilised for each prepared ink.....	43
Table 3.2: SONO-TEK ExactaCoat parameters	45
Table 3.3: List of electrodes produced for this study.....	47
Table 3.4: Contact angle summary	51
Table 4.1: Electrode samples produced in this study with its corresponding electrode weight and electrode pair weight	60
Table 4.2: Conductivity measurements of electrodes produced using 4 different deposition procedures and 2 different compositions	63
Table 4.3: Conductivity measurements of electrodes having different production methods with 83:7:10 composition on SGDL substrate	64
Table 4.4: Conductivity and thickness of electrodes after thermal treatment at different temperatures	65
Table 4.5: Contact angle measurements of electrodes having different PVDF compositions.....	65
Table 4.6: Contact angle measurements of electrodes made with slurry having different mixing times	66
Table 4.7: Contact angle of electrodes having different thermal treatment temperatures	67
Table 4.8: BET results for electrodes made through different deposition methods	69
Table 4.9: BET results for the different thermal treatment temperatures for E15 and E16....	71
Table 4.10: BET results for electrodes having different ink mixing time.....	72
Table 4.11: BET results for electrodes having different thermal treatment temperatures	73
Table 4.12: mSAC values of electrodes having different deposition methods	78
Table 4.13: mSAC values of Electrodes with different deposition methods on SGDL substrate.....	80

1 Introduction

1.1 Background and motivation: Sustainable water supply

“When the well is dry, we know the worth of water” (Benjamin Franklin).

Water is known to be a fundamental resource to human existence that is often misused. Human development has impacted more than 75% of the land surface on Earth, which exerts an expanding footprint on water resources¹. Many nations face the dilemma of dwindling water supply that affect their populations in the short and long term. Mekonnen and Hoekstra reported that two-thirds of the world population survive with acute water scarcity at least one month of the year². Water scarcity affects developing countries and countries that are economically developed. Nations facing water scarcity will likely produce less agricultural and manufactured goods and will have to import greater amounts of each at relatively higher prices^{3,4}. Thus, areas that are losing water will generally export less resulting in the value of export decreasing and import more at higher costs, resulting in import values increasing⁴.

Many aspects of human development are concerned with access to adequate quality comprising agriculture, education, health sanitation and even stability and peace. Therefore, any stride towards improving availability to adequate quality water in Africa has the capacity to solve a myriad of development barriers. Water is of great importance to Africa and the world at large. It is the task of the government and industry to make sure that the demand of adequate quality water is met with a sustainable supply of water.

In order to address sustainable water supply the change in supply of adequate quality water and the change in demand needs to be understood.

1.2 Increased worldwide water consumption and scarcity

Access to natural resources is required in order to ensure growth. We are in a period in time in which natural resources impose new limitations on growth⁵. The dynamics of population, such as age distribution, growth, migration and urbanisation, create pressures on water sources through increased water demands and pollution. Natural landscape variations associated with population dynamics may create more pressures on local water resources and the necessity for more water-related services⁵. As shown in Figure 1.1 agriculture is responsible for more than 80% of water use in developing countries, leaving little for human consumption^{6,7}.

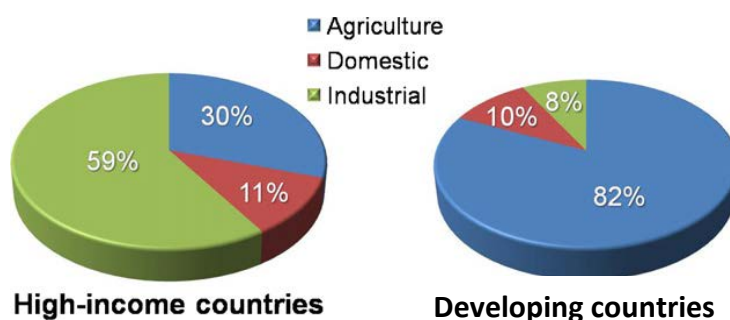


Figure 1.1: Water usage for high-income and developing countries⁷

1.2.1 Population growth

In 2010 it was estimated that more than half a billion people around the world encounter severe water scarcity throughout the year. By 2025 the amount of people inhabiting in water-stressed countries is expected to increase from half a billion to 3 billion due to an increase in population^{3,6}. By 2050 the global population is predicted to upsurge to approximately 9 billion which will lead to a rising demand for irrigation water, household and industry. Globally, cereals and meat demand has been anticipated to escalate by 65% and 56% respectively in response to population expansion and increase in earnings⁸.

Africa is the oldest inhabited territory, with the human species deriving from the continent⁶. It is the world's second largest continent, harbours fifty-four countries, occupying approximately 20.4% of the Earth's land surface⁶. It is also the second most densely inhabited continent with more than 1 billion people, which accounts for 15% of the human population. Africa is also the second-driest continent in the world and experiences from acute water scarcity problems involving water stress, water deficit/shortage and water crisis. 'Water scarcity' is the lack of sufficient water or not having access to safe water supplies. 'Water stress' is a much broader term that refers to the 'ability', or lack thereof, to meet human and ecological demand for water during a certain period. 'Water deficit/shortage' involves an insufficient quantity of water for a specific biophysical process. 'Water crisis' is a water scarcity situation leading to or is expected to lead to a dangerous situation which affects a community as a whole in a certain country⁶.

1.2.2 Improve human development index

In 2003, according to the UN, the 25 lowest-ranked countries in terms of Human Development Index (HDI), were all African. HDI measures achievements in terms of adjusted real income,

educational attainment and life expectancy^{6,9}. The struggle for clean drinking water may be indicative of how water scarcity affects human progress⁶. The desire to improve HDI could be a contributing factor for the increase in the demand for water. Less than 50% of people in rural Africa have access to both improved drinking water and sanitation⁶. Access to sanitation may be as described as having access to the safe disposal of human excreta and also the containment or treatment thereof¹⁰.

1.2.3 Industrial activities require water

Industrial activities include practises such as fabricating, processing, washing, diluting, cooling, or transporting a product¹¹ and mining¹². The amount of water utilised in industry is dependent upon many factors. These factors include the type of activity and the technology used¹². Industries that make use of large amounts of water produce merchandises such as chemicals, food, refined petroleum, paper, or primary metals¹¹. Large quantities of water are needed for the mining sector¹³. In 2015, the estimated amount of water withdrawal was 1.5 ML·day⁻¹ in the United States of America. That corresponds to approximately 1% of the total water withdrawals¹¹. From the year 2008 to 2009, industrial activities such as electricity and gas supply, food processing, manufacturing, and mining consumed 2.8 ML of water in Australia. This amounts to 20% of the total Australian water consumption for that period¹⁴.

1.3 Change in water supply

Numerous studies justify the concern for water security issues, highlighting that the accessibility to freshwater sources such as rivers, lakes and shallow groundwater aquifers are deteriorating as a result of the expanded and often unsustainable utilisation of groundwater and surface waters, degradation of water quality⁶ and poorly optimised water management systems¹⁵.

1.3.1 Impact of industrial pollution on the supply of high quality water

Pollution has a significant role on diminishing the water supply of the world. There are various sources for water pollution such as fertilisers and pesticides that run-off from farms, and waste from industrial production. Subsurface water in addition to surface water is susceptible to pollution since pollutants sink below the ground³. Mining processes may negatively influence the environment. The area surrounding mines can be potentially contaminated due to various chemicals used in the mining process. Aqueous extraction, mine cooling and drainage along with other processes produces large amounts of water, increasing the potential for chemicals

to contaminate ground and surface water¹³. In the past Grootvlei Propriety Mines Ltd discharged between 80-100 ML underground water into the Blesbokspruit wetland every day¹⁶. Mining drainage has a strong effect on the quantity of groundwater resources. Consequently mining, which results in the over-exploitation of water resources leads to a series of environmental geology problems¹⁷.

1.3.2 Global warming, climate change and its impact on fresh water accessibility

Globally, since the 1950s demand for water has tripled, while the supply of freshwater has been deteriorating⁸. Figure 1.2 illustrates the volume of freshwater resources for each continent. Ice caps and glaciers cover 10% of the world's landmass; these are concentrated in Antarctica and Greenland, containing 70% of the world's freshwater. These glaciers and ice caps are located far from human habitation and thus unfortunately are not readily accessible for human use¹⁸. Antarctica is strongly affected by climate change. Temperatures are warming at an alarming rate, approximately six times the global average, around the Antarctic peninsula¹⁹. In Greenland, ice sheets are shrinking as it melts at an accelerating pace²⁰. Shrinking glaciers provide a smaller contribution to the overall river flow. This results in river water levels lowering and becoming more variable during dry periods²¹.

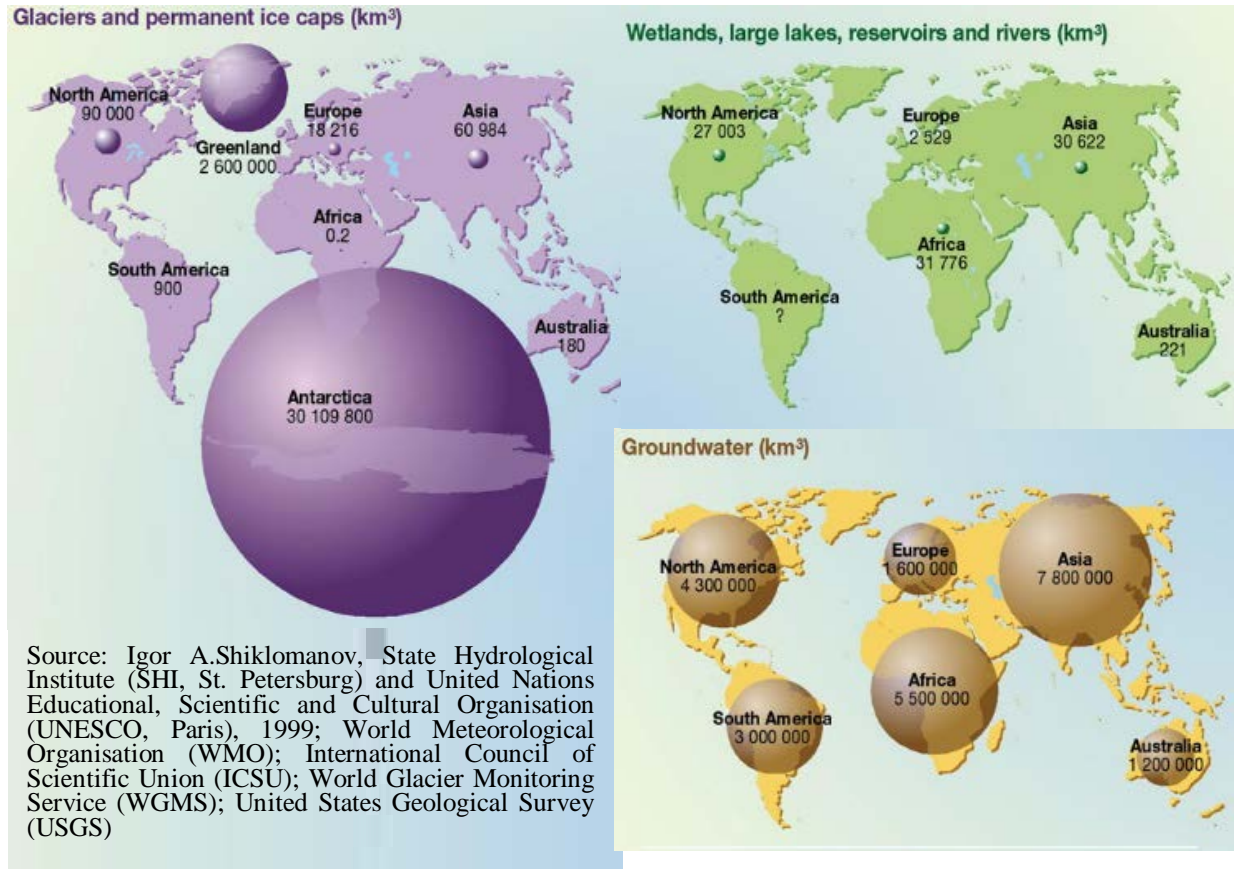


Figure 1.2: Volume of freshwater resources for each continent¹⁸

The primary natural driver of water resources is the climate system of Earth²². According to Wang et al.²³ climate change is inevitable, and is already apparent in many areas of the world^{23,24}. Primarily human activities, especially heat-trapping greenhouse gas emissions from fossil fuel combustion are responsible for climate change²⁵. Besides population and economy, climate is considered to be a pivotal factor in the water balance of a region^{23,26}. Therefore, changes in climate due to global warming could have harsh implications for water resources²³. Climate change is associated with sharp changes in temperature, which in turn is likely to affect evapotranspiration (the process by which water is transferred from the land to the atmosphere by evaporation from the soil and other surfaces and by transpiration from plants) and atmospheric water storage, thereby potentially changing the magnitudes, frequencies and intensities of rainfall as well as its seasonal and inter-annual variabilities and geographical distributions^{26,27}. Amplified temperatures and variable precipitation may alter regional water supplies and demands and, consequently, exacerbate the condition of water scarcity²³. It was projected by Parry et al. that the number of people at risk of hunger will increase by 10–20 % by 2050 because of climate change²⁸. It is very urgent to consider climate change issues in the planning and management of water resources, to be able to adapt to the changing environment²³.

Global warming has measurable effects on a hydrological cycle (the sequence of conditions through which water passes from vapor in the atmosphere through precipitation upon land or water surfaces and ultimately back into the atmosphere due to evaporation and transpiration), altering the amount, distribution and timing of available water. Climate change affects water supply through hydrologic extreme, which potentially results in flooding and drought risks²⁹.

1.3.3 Water crisis in Cape Town

Cape Town was awarded a prize in 2015 for its management of water, 3 years into the future; the city has run dramatically low on its water reserves. Figure 1.3 confirms a nearly empty reservoir near Cape Town³⁰. If the water levels keep lowering, Cape Town will have to declare “day zero”. This is the day when the city’s reservoirs are depleted and supply to the suburbs will be shut off. This scenario was not envisioned as a possibility even though the city has been known for its strong focus on the environment and respect for natural resources. It’s thus emphasis on the need for sustainability in such a city known for her standard and has been described as one of the world’s greenest cities³⁰.



Figure 1.3: Sand and dead tree trunks in a nearly empty reservoir near Cape Town³⁰

During the early summer months of 2018, the city has experienced the worst drought in the past 100 years. Because of this crisis, scientists are determining alternative means in which the crisis will have less impact on everyday life. Information about the amount of water that tertiary institutions will be able to draw and for how long are almost non-existent. Researchers locally are also concerned about how the water crisis will affect their staff and city as whole³¹.

An article in *The Lancet Planetary Health* claims that the causes of this crisis that has debilitated Cape Town finds its roots in repeated failures from the government to plan for this eventuality³¹. South Africa has been facing drought for the past three years. However, during the first two years of the drought the government placed no limitations on the water usage of farmers. Also, thinking the drought would be temporary, the government seemed to have underestimated the magnitude of the problem³¹. The economic contribution that water makes is immeasurable since it is used in agriculture, industry, and transportation. It is widely acknowledged that without a sustainable water supply, economic catastrophe will soon arise³.

1.4 Desalination as a means to meet the demand for adequate quality water

Desalination is a process whereby dissolved salts are removed from saline water to produce freshwater³². Table 1.1 lists the salinity values for different classes of water and its corresponding description and usage³³. Recently, seawater and brackish water have become essential unconventional water resources, particularly relevant³⁴ in arid areas of the world. Brackish water is defined as being salty but less saline than seawater. Brackish water can be found in aquifers and certain surface water settings such as estuaries³⁵.

Brackish water desalination could be considered as an important solution for the supply of clean water³⁶. The challenge involves removal of dissolved inorganic salts and other contaminants³⁷. At present, the commercial techniques that are used are reverse osmosis, distillation, and electrodialysis. The concerns with these techniques like the relative high energy input, secondary waste generation and poor efficiency^{36,37} will be discussed in detail in Chapter 2.

Table 1.1: Salinity status classifications³³

Salinity status	Salinity (g·L ⁻¹)	Description and use
Fresh	< 0.5	Drinking and irrigation
Marginal	0.5 - 1	Irrigation, adverse effects on ecosystems become apparent
Brackish	1 - 2	Irrigation certain crops only; useful for most stock
Saline	2 - 10	Useful for most stock
Highly saline	10 -35	Very saline groundwater; limited use for certain livestock
Brine	> 35	Seawater, some industrial and mining uses exist

Capacitive deionisation (CDI) is a desalination technique which removes ions from aqueous solutions by applying a voltage between pairs of porous electrodes³⁸. In CDI, a potential is applied between two electrodes that forms electrical double layers (EDL), driving the ions toward the surfaces of the two electrodes. The anode is aggregated by cations and anions aggregate around the cathode. This results in relatively deionised water exiting the cell³⁹. Due to the good performance of CDI, it has been proposed as a promising alternative technique for the desalination process⁴⁰. Commonly it has been applied to brackish water desalination, but is also used for microfluidic sample preparation, organic stream remediation, water softening and wastewater remediation⁴¹⁻⁴⁴. CDI has been anticipated to be of low-energy consumption and, due to its capability of regenerative electrodes, an environmentally friendly process⁴⁰. This electrochemical process uses a low-voltage electric field to separate ions from a solution. This is done in a two-step process; ions are stored in the EDL of a porous electrode throughout water treatment, later the ions can be discharged into a waste water stream regenerating the

electrodes⁴⁵. Additionally, ions can selectively be removed based on ion valence, diffusivity and size⁴⁶.

1.5 Problem statement and the challenge going forward

All aspects of human development are concerned with the availability of adequate quality water including health, agriculture, education, and even peace and political stability. Therefore, any step towards improvement of- and access to- clean drinking water in Africa has the potential to solve a myriad of development barriers. Water is of great importance to Africa and the world at large.

Many parts of the world face problems associated to the dwindling supply of adequate quality water. With time, the demand of water has increased mainly due to population growth and increased industrial activities. On the other hand, the supply of adequate quality water is decreasing due to an increase in industrial activities and the effects of global warming and climate change. To meet the local adequate quality water demand, cost effective desalination of saline water resources would be desired. As desalination technologies are generally energy intensive, the overall cost of adequate quality water will increasing considerably.

In South Africa there are areas that are facing a water crisis due to a decrease in rainfall during the winter months. Reverse Osmosis installations have been built to produce drinking quality water from sea water (a virtually unlimited water resource) in an attempt to meet the city's demand for drinking quality water. However, the energy demand to run the compressors for the RO plant is considerable ($3-10\text{kW}\cdot\text{h}\cdot\text{m}^{-3}$), resulting in a significant increase of the drinking water cost⁴⁷.

Advanced water desalination technologies designed to operate with reduced energy input is of great interest. The following chapter will provide an in-depth background of current and upcoming desalination technologies from which the research questions will emanate.

2 Literature Review

2.1 Types of desalination

Desalination, which is the removal process of dissolved salts, is an energy intensive process⁴⁸, and innovations are required to reduce the energy requirements⁴⁹. Currently there are a minimum of four principle approaches of desalination in existence: thermal, pressure, ion exchange⁵⁰ and electrical⁵¹. Figure 2.1 illustrates a visual summary of membrane and thermal processes. 86% of membrane-based plants belong to reverse osmosis while electro dialysis accounts for only 14%.

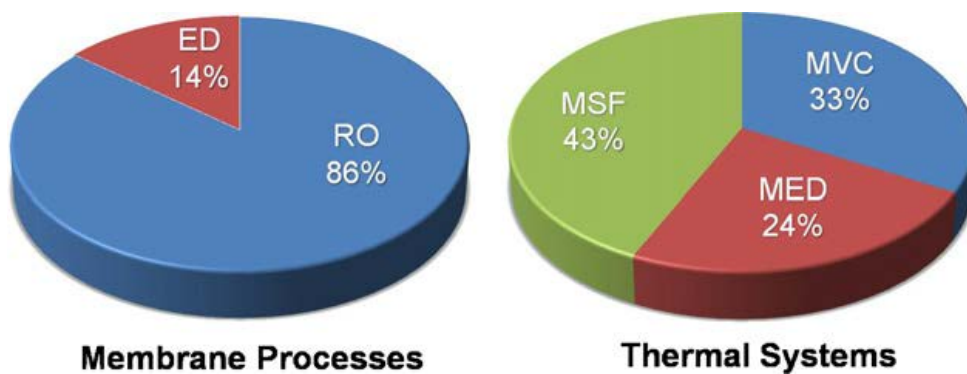


Figure 2.1: Percentage of membrane and thermal desalination plants worldwide⁷. ED: Electro dialysis, RO: Reverse osmosis, MED: Multiple-effect Distillation, MVC: Mechanical Vapour Compression, MSF: Multi-stage Flash

Figure 2.2 presents the impact these desalination techniques has on the desalination market. While there are more plants using membranes than thermal methods, the total amount of water processed is slightly more for thermal than membrane methods⁷.

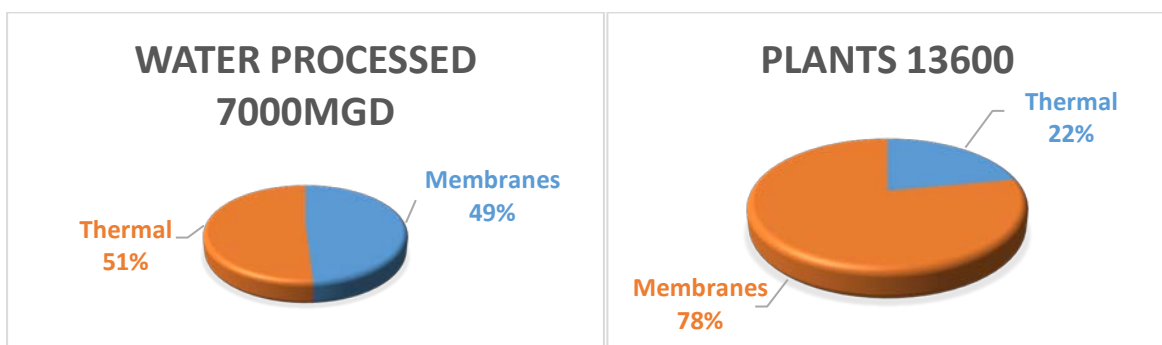


Figure 2.2: Percentage of membrane and thermal desalination plants worldwide and percentage of processed water. MGD: million gallons per day⁷

2.1.1 Thermally driven desalination processes

Thermal distillation is the oldest method and has been described by Aristotle as early as 400 BC. In this method heat is applied to vaporize water from saltwater, leaving the salt behind after the steam has been condensed and collected to produce distillate^{49,51}. Significant amounts of energy are required for the vaporization phase change; thus, thermal desalination plants are usually located in areas where there is an abundance of energy available^{51,52}. Modern methods of distillation make use of different practices such as vessels with low-pressure to lower the boiling temperature of the water and therefore, lower the energy needed to desalinate⁵¹. For more than four decades thermal-based technologies such as multiple-effect distillation (MED) and multi-stage flash (MSF) distillation have dominated the landscape of desalination⁵² and are widely used in the petrochemical industries⁵³.

2.1.1.1 Multiple-effect distillation

In MED multiple boiling stages are used without the need to additional heat input to evaporate the water. Figure 2.3 illustrates the principle of a MED process. Primary steam is condensed in the first effect for the evaporation of preheated saltwater. MED has a high-performance ratio (ratio of mass of product water to mass of initial steam input) due to the competent thermodynamics and heat transfer of the process. Although effective and operational for lengthy periods of time, this process is not without limitations⁵². A possible drawback of MED is the corrosion and scaling of the reactors, piping, and fittings of the units⁵⁴.

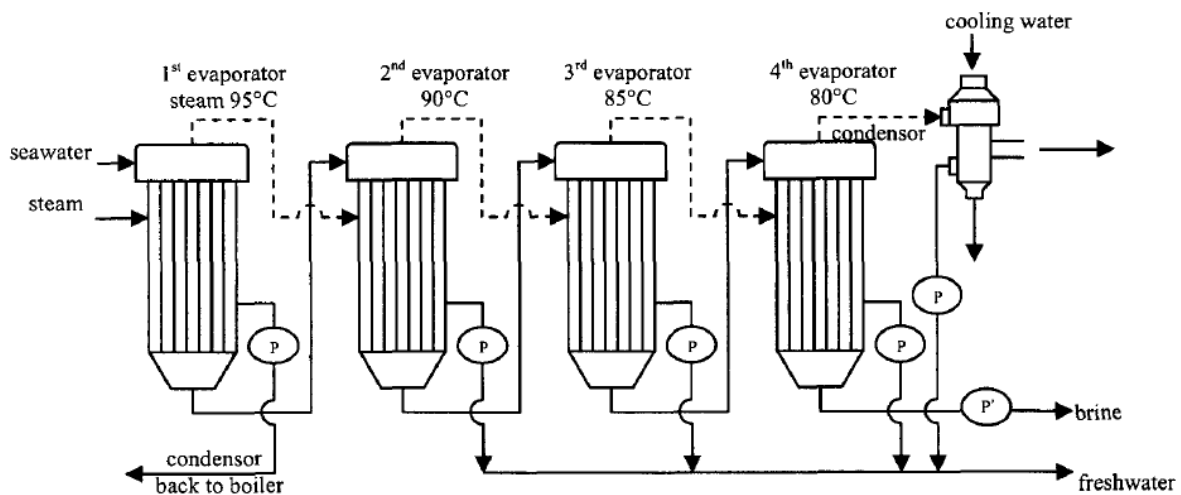


Figure 2.3: MED Principle⁵⁴

In the Kingdom of Saudi Arabia, there are MED systems located in many locations with capacities ranging from 1.5-800 ML·day⁻¹⁵⁵. This is a result of MED having the ability to operate at low temperature and use lower grade heat from power station turbines as the primary

source of heat for MED yield low specific energy costs for desalination of seawater and permits the use of lower grade materials for heat transfer tubes and the evaporator body⁵⁶.

2.1.1.2 Multi-stage flash distillation

MSF originated more than five decades ago⁵⁷. It began replacing MED due to its simplicity and reliability^{52,54}. The operation principle, which is presented in Figure 2.4 is based on a series of flash chambers where steam is generated from saline feed water at a reduced pressure. Heat exchange, with a series of closed pipes where the saltwater to be desalted is preheated, condenses the steam. The condensate, which is obtained as the desired product, is collected using collector trays. To obtain a higher water recovery, the exhausted brine is partly recirculated and partly rejected to the sea. The most noticeable disadvantage of MSF is the lower performance ratio. This makes MSF a costlier technique since the amount of energy consumed is much higher⁵⁴. Another disadvantage is the inflexibility in power and water cogeneration systems⁵⁷.

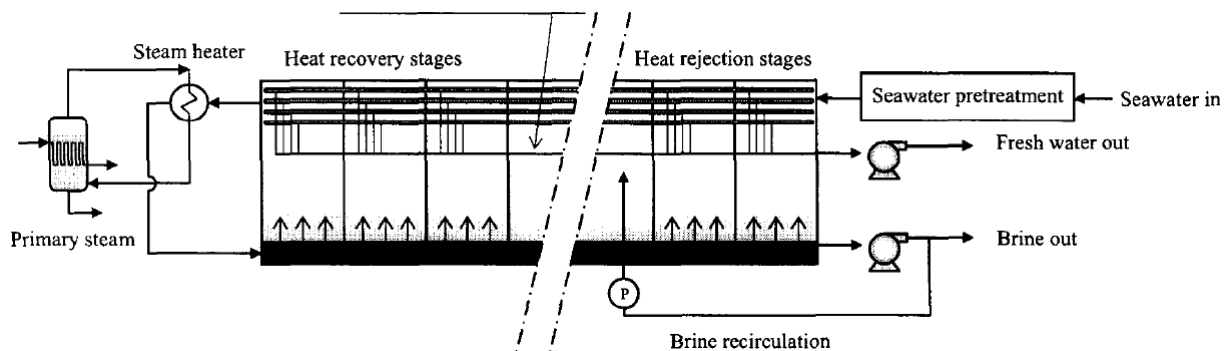


Figure 2.4: MSF Principle⁵⁴

2.1.2 Pressure driven desalination processes

2.1.2.1 Reverse osmosis

Reverse osmosis (RO) is a method of desalination which makes use of the second principle method. Pressure is used to drive water through a semipermeable membrane that impedes the passage of dissolved organic and inorganic material^{49,51}. Figure 2.5 illustrates the process of reverse osmosis. Seawater permeates through a membrane by applying a pressure greater than the osmotic pressure of the seawater. The membrane is permeable for the water but not the dissolved salts. Hence a separation between a pure water fraction (permeate) and a concentrated fraction (retentate or concentrate) is obtained⁵⁴. Reverse osmosis has been used increasingly in the past three decades for the desalination of seawater and brackish water, as well as water

treatment and wastewater reclamation due to the superior and stable quality of the water produced and the relatively low cost⁴⁸.

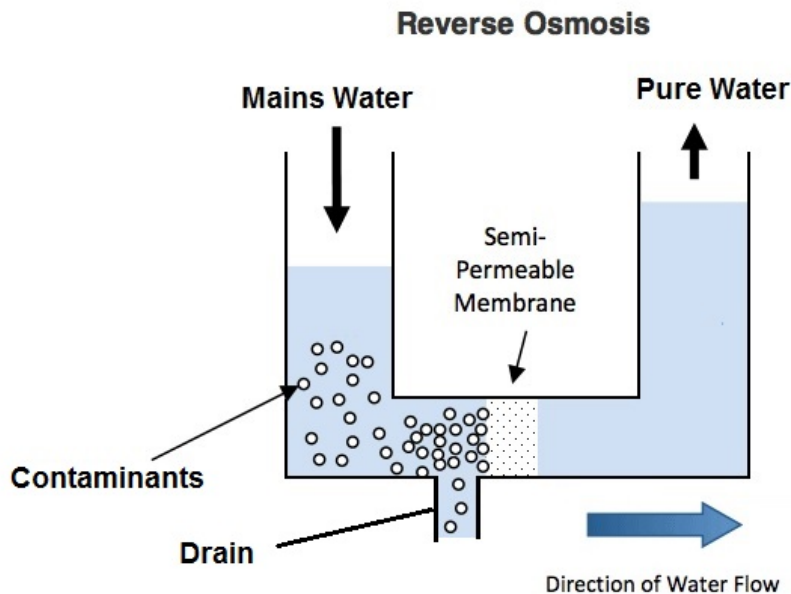


Figure 2.5: RO Diagram⁵⁸

The first successful application of reverse osmosis was brackish water desalination with the first appearance of a large-scale plant being in the late 1960s. New RO membranes appeared in the next decade with higher permeability making RO suitable for seawater desalination. RO became competitive with classical distillation techniques in the 1980s. In the early stages of RO pressures needed for the separation were as high as 120 bar, however with new developments the required pressure has significantly decreased to below 50 bar for seawater and below 20 bar for brackish water. Majority of membranes for RO are polymeric thin-film composite membranes. These membranes consist of a thin separating layer and numerous supporting layers with much lower resistance against mass transport. The configurations of the membranes are usually spiral-wound modules, where seawater flows between two flat membrane sheets wrapped around a central tube. Hollow fibre membranes can be used as an alternative, where membrane tubes of approximately 0.5 mm are utilised⁵⁴. Although reverse osmosis for desalination of seawater is currently the dominant technology, it does have disadvantages. Pre-treatment of seawater is needed prior to RO desalination⁵⁹. This is done to ensure a stable performance of the module, and optimisation of the pre-treatment is one of the most significant aspects of RO⁵⁴. Another disadvantage is the sensitivity of RO membranes to fouling⁵⁴ (amassing of unwanted material on a solid surface to the detriment of function), which is the accumulation of unwanted material on solid surfaces to the detriment

of function. The energy required for desalination increases due to membrane fouling either by decreasing productivity or increasing the driving force⁵⁹.

2.1.2.2 Nanofiltration

Nanofiltration (NF) membranes are unique compared to RO since it has varying selectivity toward different electrolytes⁶⁰. NF operates at much lower pressures compared to RO, resulting in a significantly lower energy inputs, which is the reason why NF could be more cost effective and environmental friendly⁶¹ than RO. NF is occasionally used in wastewater treatment and drinking water purification^{61,62}. Figure 2.6 demonstrates the NF mechanism. It has great properties in selectively rejecting different charged organic dyes and salt ions due to Donnan exclusion, its electrostatic interactions and physical size sieving exclusion^{60,61}.

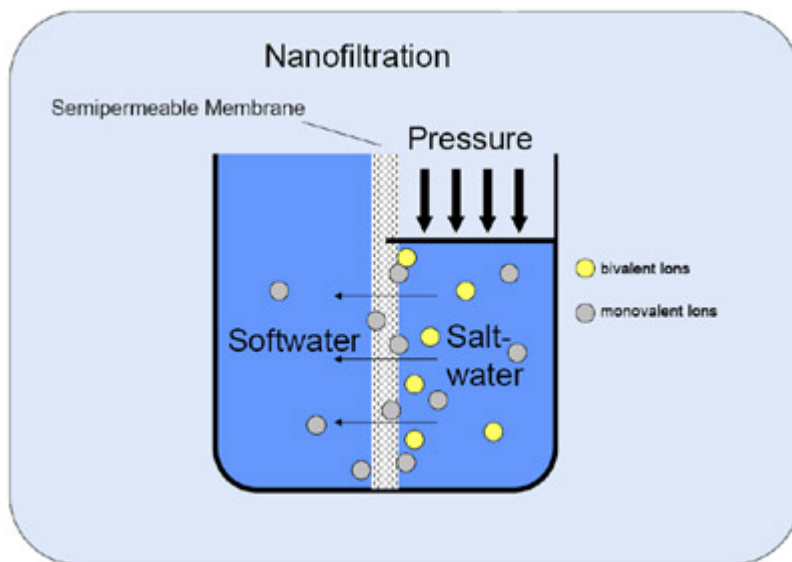


Figure 2.6: How Nanofiltration works⁶³

NF allows smaller molecules and ions such as water and monovalent ions to pass through the membrane, while rejecting larger molecules such as organic dyes and hazardous heavy metal ions⁶¹. When the hydrated size of species approaches the membrane pore size, they are sterically retained,⁶⁴ and transport within the pores may be delayed⁶⁰.

An efficient membrane should have high permeate flux, be selective during rejection, have reinforced mechanical property, long term stability in harsh chemical solutions⁶⁵⁻⁶⁷ and should also have excellent antifouling property during the operation process^{61,65}. NF membranes have the capability of removing monovalent ions to different extents, however, the difference in selectivity for the passage of varying monovalent ions is commonly small, and the mechanism for such a variance is poorly understood⁶⁰. Although nanofiltration has the favourable benefit of having the ability to process large volumes and continuously produce streams of products,

it is the least used membrane filtration method in water purification industry⁶⁸. Relative high operation and maintenance costs have been mentioned as possible reasons for the limited number of industrial implementations⁶⁹.

2.1.3 Ion-exchange desalination process

Ion-exchange (IE) technology is an attractive technology due to its relative simplicity of application, low cost and effectiveness to remove ions from wastewater, especially diluted solutions^{70,71}. IE is a process of separation where harmful or undesired ions are isolated from the solution to the resin or other IE material and is replaced by others which do not contribute to the contamination of the environment, since mostly the undesired ions is changed by another ion which is neutral within water bodies. The change continues until ionic equilibrium is reached by the ion exchanger. The capacity of the ion exchanger is then exhausted and no exchange is possible any longer. The IE column is removed from service after this, regenerated and reused after usage⁵⁰. Because carbon dioxide (CO_2) is weakly charged it will not be attracted to the resin bead. The CO_2 , however, can combine with a hydroxide ion (OH^-) to form bicarbonate. The resin bead will quickly become exhausted when loaded with hydroxide ions and with the presence of CO_2 . A classic scenario on how the process works is shown in Figure 2.7.

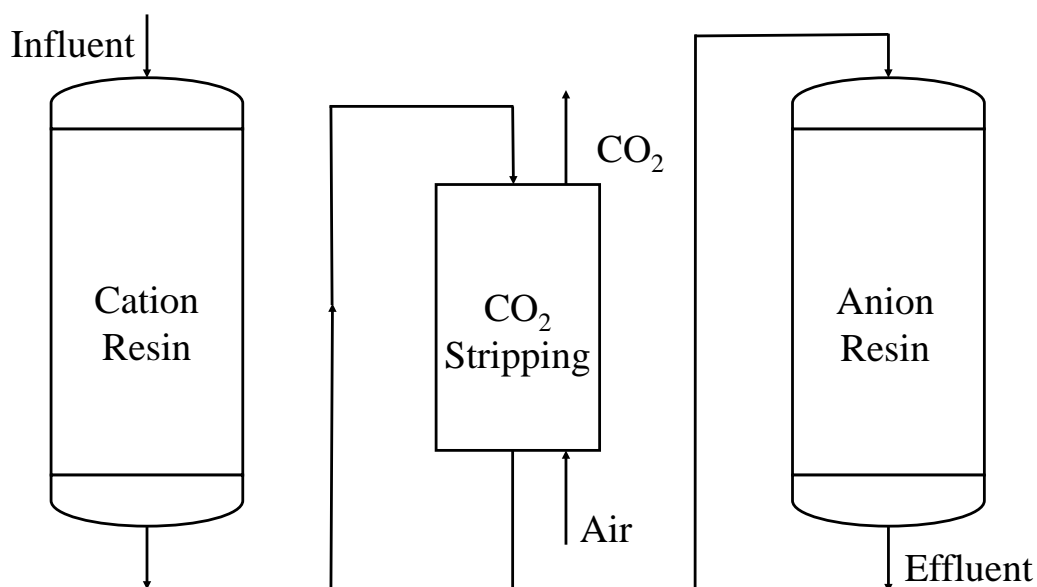


Figure 2.7: Ion Exchange system⁷²

The reason for CO_2 stripping is to prevent it from converting back into bicarbonate ions as the pH increases. In 2003, the City Public Service in San Antonio, Texas found that removing the

CO₂, the system operated for longer periods of time before regeneration was required⁷³. The utilisation of this technique is dependent upon several factors such as contact time, flow rate, initial contact pollution, operating temperature, pH and resin characteristics^{71,74}. Several studies have been reported on the selective removal of heavy metal ions by IE which include the removal of Pb(II), Hg(II), Cd(II), Ni(II), V(IV,V), Cr(III,VI), Cu(II) and Zn(II) from water and industrial wastewaters⁷⁵⁻⁷⁷. IE resins (functionalized porous or gel polymer) have also been applied in the drinking water treatment sector⁵⁰. Bolto et al. reported that when there is a high concentration of natural organic matter (NOM) in contaminated water there are high percentages of NOM removal efficiency found in the IE process⁷⁸.

Although some authors state that IE technology is environmentally friendly with relatively low maintenance cost⁷⁶, disadvantages such as organic contamination from the resin⁵⁰, calcium sulphate fouling, iron fouling, adsorption of organic matter, and bacterial and chlorine contamination have been reported as well⁷⁹. Furthermore, the use of an acid and base solutions to regenerate cationic and anionic resins respectively have a considerable impact on the running cost of the IE process and lead to the generation of secondary waste.

2.1.4 Electrically driven desalination processes

2.1.4.1 *Electrodialysis*

In 1833 Faraday first reported the principle of removing ions from solution^{52,80}. Electrodialysis (ED) is based upon the transport of dissolved salts through a stack of cationic and anionic membranes⁵⁴. The principle of an ED cell is depicted in Figure 2.8. Electrodialysis does not require pressure or heat to drive separation⁵². In order to transport ions selectively through membranes⁴⁹ an electrical potential is applied between two electrodes⁵². Anions migrate toward the positively charged anode and cations migrate towards the negatively charged cathode. Cations are repelled by anion exchange membranes and pass through cation exchange membranes since the ions are repelled by the membranes that carry the same charge⁵².

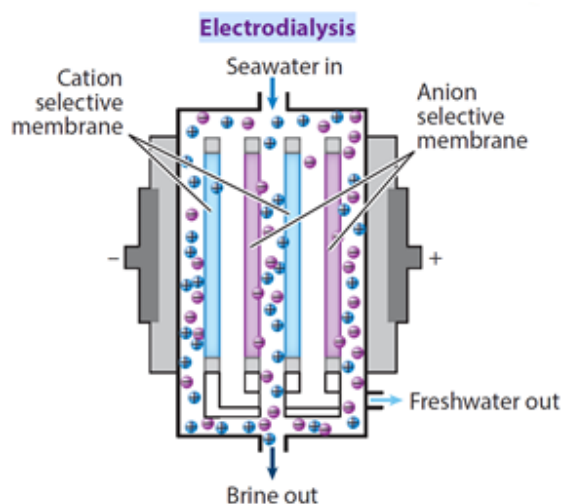


Figure 2.8: ED Principle⁵²

The concentration of salts to be removed largely determine the cost for desalination⁵⁴, and ED is suitable for desalinating water with a concentration of $\sim 10 \text{ g}\cdot\text{L}^{-1}$ or lower⁵². The ED process thus becomes uneconomical for large salt fractions but is suitable for brackish water desalination⁵⁴. Although ED is a promising technique⁵⁴ there are various issues limiting scale-up and wide use of this technique to desalinate water. Some of these issues include water splitting at high voltages, increased pH at the anion exchange membrane interface with CaSO_4 precipitation, expensive platinum electrode material cost, lack of long-term reliability, increased energy requirement with increasing salt removal, minimum salt-concentration requirement to meet minimum conductivity threshold, and extensive cleaning requirements⁵².

2.1.4.2 Capacitive Deionisation

Capacitive deionisation (CDI) is an emerging process and potentially cost-efficient desalination technology for brackish water. It can function at low potential and ambient conditions. Salty water passes along a pair of electrically charged electrodes and the dissolved salts can be removed⁸¹. It has advantages of low energy consumption, high energy efficiency, and is therefore considered as environmental friendly. Promising applications include water softening, deionisation of metal contaminated water or wastewater, and desalination of salt water⁸².

CDI could possibly replace ED⁸⁰ and outperforms reverse osmosis in energy efficiency at brackish feed water concentration ($< 3 \text{ g}\cdot\text{L}^{-1}$ of NaCl)⁸³.

Figure 2.9 illustrates the design of a CDI device. In this method ions are absorbed directly into the porous electrodes and must be desorbed by reversing the charge of the electrode⁵². Section 2.3 describes the CDI technology in great detail

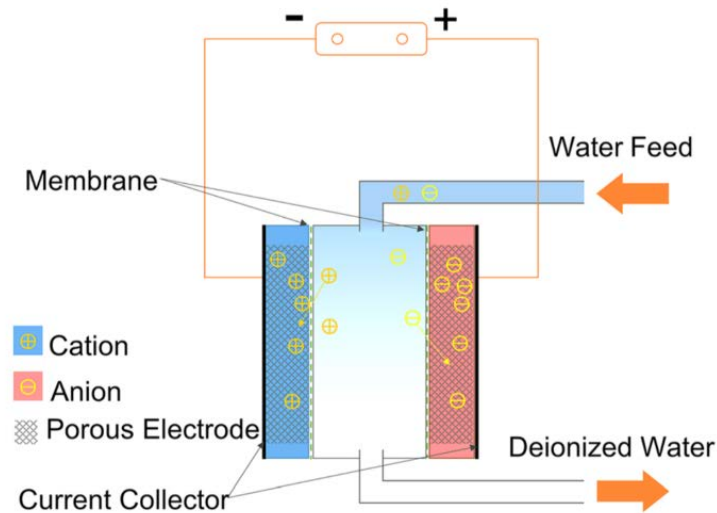


Figure 2.9: Illustration of CDI device³⁹

2.2 Energy requirements for water desalination and its cost

Since access to adequate quality drinking water is seen as a basic human right¹⁰, desalination plants are being built to supplement dwindling fresh water resources and foresee the growing drinking water demand. The number of seawater desalination plants, in the past 10 years, has rapidly increased. In 2016, the global freshwater production using desalination was approximately 380 million ML·year⁻¹. This is more than double the production level of 2008. However, desalination is generally speaking energy intensive and tends to be expensive⁸⁴. In order to satisfy the increasing demand for adequate quality water, the portion of saline feed water versus surface feed water is likely to increase. Reduction of the energy input for the desalination processes maintains to be important as water treatment must remain economically feasible.

From a water treatment cost perspective, both the capital expenses (CAPEX) and operational expenses (OPEX) need to be considered. The most economic water treatment process with will show the best combination between CAPEX and OPEX

In the 1970s, water distillation processes offered a better CAPEX-OPEX combination than RO. When early membrane started to show high salt rejection, the required energy inputs were still

high while the productivity per area of membrane were low. . Since then, ground-breaking advanced have been made in both membrane materials and module development⁸⁵. In the early stages of RO, pressures as high as 120 bar were needed for separation⁵⁴, however, with time the required pressure reduced to 2-17 bar for brackish water⁸⁶. A significant reduction in the specific energy consumption (SEC) was seen from 1990 to 2009. In 1990, RO had a SEC of $8.5 \text{ kW}\cdot\text{h}\cdot\text{m}^{-3}$, and in 2009 it was reduced to less than $3 \text{ kW}\cdot\text{h}\cdot\text{m}^{-3}$. This is due to the inclusion of new incoming energy recovery devices (ERDs) such as Francis turbine, Pelton turbine, and hyperbaric recovery devices⁸⁷. ERDs that are used in the water treatment industry reduce power by harnessing energy in the concentrate waste stream and transferring it to the feed side through different methods⁸⁸.

Currently, the majority of the current desalination technologies available are based on reverse osmosis. Current large-scale seawater reverse osmosis (SWRO) plants have the capability to produce clean water for as little as $\$0.50 \text{ m}^{-3}$ ⁸⁵. Figure 2.10 illustrates a breakdown of energy consumption within a standard seawater desalination plant utilising the Pacific Ocean water of total dissolved solids (TDS) concentration of $33.5 \text{ g}\cdot\text{L}^{-1}$ as a source. In this illustration, the total plant energy use is $3.57 \text{ kW}\cdot\text{h}\cdot\text{m}^{-3}$. Seawater reverse osmosis (SWRO) system accounts for 71% of the total plant energy use⁸⁰.

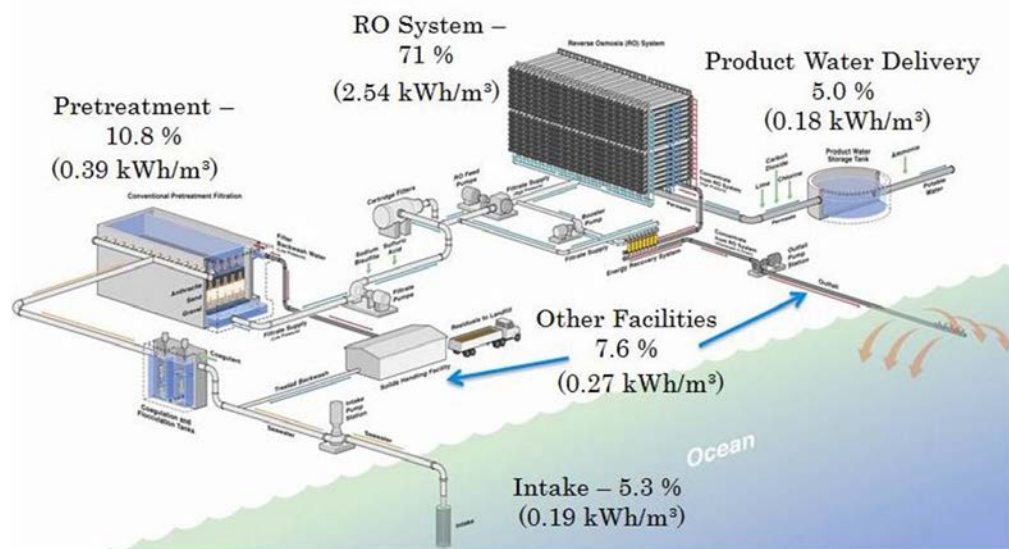


Figure 2.10: SWRO desalination plant energy breakdown⁸⁰

Table 2.1 shows a comparison of five different desalination techniques. Two of these processes are thermal. Characteristically, thermal desalination plants are located in areas where energy is relatively cheap. The MED plant in the United Arab Emirates has a capacity of $45.4 \text{ m}^{-3}\cdot\text{day}^{-1}$ ⁵². Performance of the three major electrically driven processes are also shown. Due to

electrodialysis being suitable for the desalination of brackish ($\sim 10 \text{ g}\cdot\text{L}^{-1}$) or lower concentration region, it represents relatively small fraction of the total desalination capacity worldwide⁸⁹. The energy requirements of this process are directly proportional to the amount of salt removed. A minimum salt concentration ($0.4 \text{ g}\cdot\text{L}^{-1}$) in the stream is required to acquire good conductivity; alternately, a maximum feed concentration ($\sim 2\text{-}10 \text{ g}\cdot\text{L}^{-1}$) should not be exceeded due to this technique not being able to desalinate efficiently above these concentrations. In 2014 there were only four-pilot plants for CDI, with a largest capacity of $3.8 \text{ ML}\cdot\text{day}^{-1}$ ⁵². Welgemoed and Schutte⁹⁰ demonstrated that the cost to desalinate a $2 \text{ g}\cdot\text{L}^{-1}$ feed was $\$0.35 \text{ m}^{-3}$ for reverse osmosis and $\$0.11 \text{ m}^{-3}$ for CDI. CDI requires less energy compared to RO. Ultimately this lowers greenhouse gas emissions, thus, reducing environmental impacts and decreasing operational costs⁴⁵.

Table 2.1: Comparison of different desalination processes, modified from⁵²

Process	Plant capacity ^a ($\text{ML}\cdot\text{day}^{-1}$)	Energy requirement ($\text{kWh}\cdot\text{m}^{-3}$)	Worldwide capacity ^b (%)
Hybrid (RO and MSF)	1036 (Ras Al Khair)	0.5	-
RO	600 (Sorek)	0.5	69
Multi-effect distillation	45.4	1.8-21	7
Multistage flash	815.1	4-20	18
Nanofiltration		0.3-1	3
Electrodialysis	45	0.4-8.7	2
Capacitive deionisation	3.8 (pilot)	0.1-2.03	<1
Membrane capacitive deionisation	5 (pilot)	1.96	<1

^a Largest daily capacity for each process

^b Percent of total worldwide capacity in 2018⁹¹.

The capital cost for membrane capacitive deionisation (MCDI) is rather expensive.

Cost factor	Cost Item	Value (€)	Value (ZAR)
Capital:	MCDI cells	150 € m^{-2} cell	2437 ZAR $\cdot\text{m}^{-2}$ cell
	<i>Purchased</i>	10-20 k€per pump	162 441-324 881 ZAR per pump
	<i>equipment</i>	10 k€per power supply	162 441 ZAR per power supply

Operating cost:	Energy: Chemicals Cell replacement Water consumption Wastewater treatment <i>Maintenance</i>	Desalination: 2.5 kWh·m ⁻³ Pumping 0.120€ (kWh) ⁻¹ for 60% efficiency HCl 22%: 78 €m ⁻³ 2 years cell lifetime Tap water: 1 €m ⁻³ , deionised water: 2 €m ⁻³ 1 €m ⁻³ 5% of equipment cost	Desalination: 2.5 kWh·m ⁻³ Pumping 1.95 ZAR (kWh) ⁻¹ for 60% efficiency HCl 22%: 1267 ZAR·m ⁻³ 2 years cell lifetime Tap water: 16 ZAR·m ⁻³ , deionised water: 32 ZAR·m ⁻³ 16 ZAR·m ⁻³ 5% of equipment cost
-----------------	-------------------------------------------------------------------------------------------------------------	------------------------------------------------------------------------------------------------------------------------------------------------------------------------------------------------------------------------------------------------------------------------------	-------------------------------------------------------------------------------------------------------------------------------------------------------------------------------------------------------------------------------------------------------------------------------------------------

Table 2.2 breaks down the capital and operating cost associated with large scale MCDI which will be used to desalinate biomass hydrolysate. Huyskens et al.⁹² investigated the economic viability of MCDI for a production capacity of 500 ton sugar per day with a target sodium removal from 3 to 0.1 g.kg⁻¹. Capital cost consist of the MCDI cell cost and the cost of the equipment installed. The MCDI cell cost include current collectors, porous carbon electrodes, ion-exchange membranes, spacer channels, cell housing, hydraulic, and electrical connections. The operating cost of MCDI include energy, chemicals for cleaning, cell replacement, water consumption, wastewater treatment, maintenance and depreciation.

Table 2.2: Capital and operating cost of MCDI⁹²

Cost factor	Cost Item	Value (€)	Value (ZAR)
Capital:	MCDI cells <i>Purchased equipment</i>	150 €m ⁻² cell 10-20 k€per pump 10 k€per power supply	2437 ZAR·m ⁻² cell 162 441-324 881 ZAR per pump 162 441 ZAR per power supply
Operating cost:	Energy: Chemicals Cell replacement Water consumption Wastewater treatment <i>Maintenance</i>	Desalination: 2.5 kWh·m ⁻³ Pumping 0.120€ (kWh) ⁻¹ for 60% efficiency HCl 22%: 78 €m ⁻³ 2 years cell lifetime Tap water: 1 €m ⁻³ , deionised water: 2 €m ⁻³ 1 €m ⁻³ 5% of equipment cost	Desalination: 2.5 kWh·m ⁻³ Pumping 1.95 ZAR (kWh) ⁻¹ for 60% efficiency HCl 22%: 1267 ZAR·m ⁻³ 2 years cell lifetime Tap water: 16 ZAR·m ⁻³ , deionised water: 32 ZAR·m ⁻³ 16 ZAR·m ⁻³ 5% of equipment cost

The MCDI process total energy consumption is calculated as the sum of the desalination energy, cell regeneration and pumping energy. Cell cleaning with 4% HCl is included for 3 minutes during standby. The annual water cost for rinsing and regenerating the MCDI cell, including the preparation of the cleaning solutions is included. The wastewater generated covers the water used for cell regeneration and the total volume of the cleaning solution⁹². The high capital cost of the CDI plants is the main reason this technology is not widely spread. Welgemoed and Schutte⁹⁰ performed one of the largest and most comprehensive tests using CDI technology. They demonstrated a 3.8 ML·day⁻¹ CDI desalination unit, and showcased that CDI can be cost effective against RO at low salinities. CDI can only compete at higher salinities

if there is a significant reduction in capital cost⁹³. Therefore, the aim of this research is to make CDI more cost effective by reducing the capital cost. Table 2.3 illustrates the capital and operating cost associated with reverse osmosis for a plant having a desalination capacity of a million litres per day⁹⁴.

Table 2.3: Capital and operating cost of RO with a capacity of 1ML per day ⁹⁴

Cost factor	Cost Item	Value (€)	Value (ZAR)
Capital	Direct capital construction cost	810 000	13 157 693
	Project engineering services	168 750	2 741 186
	Project development	101 250	1 644 712
	Project financing	108 000	1 754 359
	Contingency	162 000	2 631 539
Operating cost	Energy consumption	0.24 €m ⁻³	3.90 ZAR·m ⁻³
	Maintenance	0.08 €m ⁻³	1.30 ZAR·m ⁻³
	Labour	0.08 €m ⁻³	1.30 ZAR·m ⁻³
	Chemicals	0.06 €m ⁻³	0.97 ZAR·m ⁻³
	Indirect cost	0.05 €m ⁻³	0.81 ZAR·m ⁻³
	Membranes	0.03 €m ⁻³	0.49 ZAR·m ⁻³
	Waste disposal	0.02 €m ⁻³	0.32 ZAR·m ⁻³
	Monitoring	0.02 €m ⁻³	0.32 ZAR·m ⁻³

Direct capital construction costs entails the buildings and other structures, pipeline equipment, and site development. Usually, these direct capital costs account for 50 to 85% of the total capital expenditure (CAPEX). CAPEX costs can be further divided into nine parts, see Figure 2.11. The scale of the desalination plant determines the CAPEX, with larger plants costing less per million gallons of installed capacity⁹⁵.

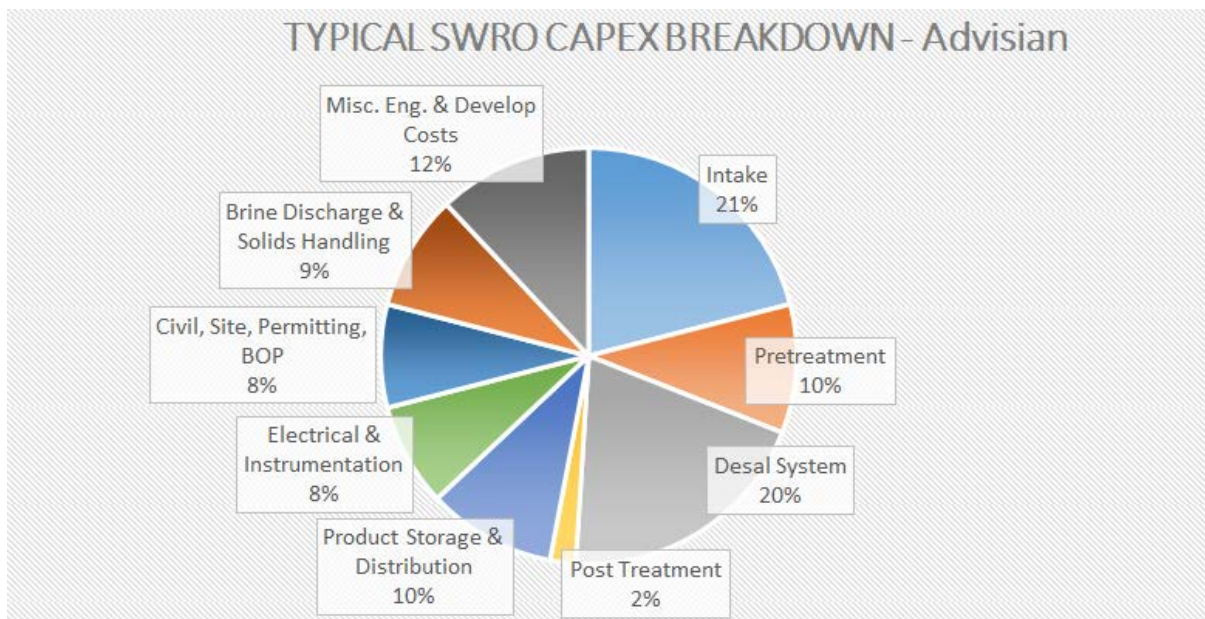


Figure 2.11: SWRO desalination CAPEX breakdown⁹⁵

2.3 Capacitive Deionisation

2.3.1 CDI history

Blair and Murphy reported the concept of electrochemical demineralisation in 1960⁹⁶. The commercial relevance and long-term operation of CDI was demonstrated in 1968 by Reid⁹⁷. Johnson et al. introduced a theory for ion transport in porous carbon electrodes in 1971 for CDI and ion storage. They presumed that no charge passes directly from the carbon into the solution. Consequently, a flow of current into the carbon is compensated by an equal and opposite magnitude of charge on the solution side of the interface. They stated that the interface is similar to an electrical capacitor⁹⁸. CDI attracted more attention from 1990 onward due to the development of new electrode materials, such as carbon aerogels⁹⁹ and carbon nanotube (CNT) electrodes¹⁰⁰. The term capacitive deionisation was introduced in 1996 by Farmer et al. and made use of the abbreviation “CDI” for the first time^{101,102}. Andelman et al. patented charge barrier flow-through capacitor and introduced Membrane Capacitive Deionisation¹⁰³. Despite the initially slow development of CDI, the past 10 years has shown tremendous advances, including the progression of flow electrodes¹⁰⁴, hybrid CDI systems⁸⁷, membrane CDI¹⁰⁵, and the discovery of important correlations between pore size and electrosorption performance¹⁰⁶. In the past few years there has been an expansion of novel architectures for CDI cells⁴¹. Scientists aim to harness potential energy savings and ion selectivity resulting in CDI experiencing rapid growth⁴⁵. In 2013, a new geometric class for CDI was illustrated by Jeon et al.¹⁰⁵ which leveraged carbon flow electrodes, or carbon slurry electrodes. This newly designed process was experimentally tested for seawater desalination¹⁰⁵.

2.3.2 Electrical double layer theory

Ion transport and ion adsorption occur in two different pore types in the carbon electrode, see Figure 2.12. Macropores are interparticle pores serving as transport highways for ions; micropores are intraparticle pores where EDLs form and ions are stored. To model ion adsorption in CDI the EDL theory is used, which relates the concentration of ions in the micropores of an electrode to the concentration in the bulk solution, or to the concentration in the macropores. Modelling the dynamics of ion adsorption, the transport of ions from the spacer channel, and across the membranes in MCDI, into the electrodes, towards the micropores are also taken into account¹⁰⁷.

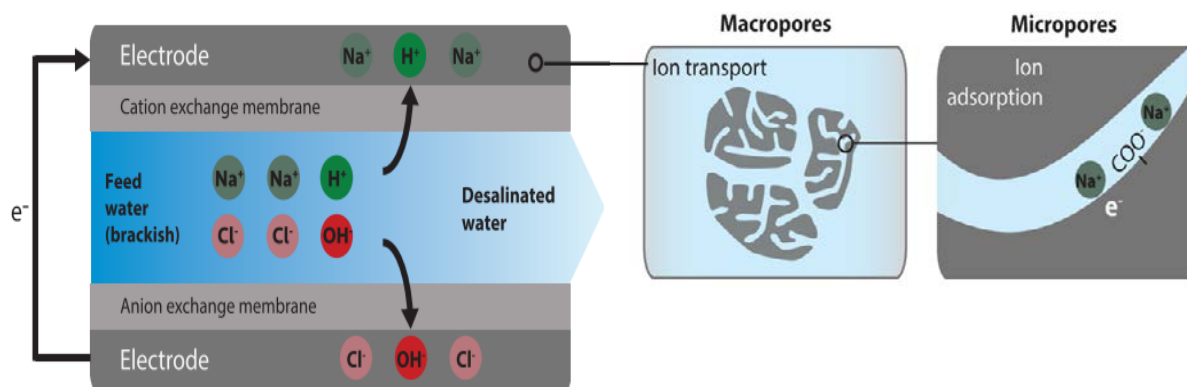


Figure 2.12: Schematic of ion adsorption coupled with ion transport theory in CDI¹⁰⁷

In electrochemistry, electrical double layer (EDL) is a basic concept¹⁰⁸. This concept dates back to Helmholtz who in the 19th century assumed that all surface charge is directly charge-compensated by countercharge adsorbed to the surface. This means the surface charge is directly compensated by the condensed layer of counterions. Co-ions have the same charge sign as that of the surface and are thus repelled from the surface. It would be ideal for CDI if the Helmholtz-model would hold, meaning for each electron transferred from one electrode to another, one cation would be transferred into the cathode to compensate the negative electronic charge there, while on anion would be transferred into the anode to compensate for the positive electronic charge there. As a result, one full salt compound would have efficiently been removed from the feed water¹⁰⁹. In CDI, the EDL is formed when the electrode is charged and put into an ionic solution, the interface of the charged electrode and ion rich solution will be inhabited with counterions due to the Coulomb force. Removing the Coulombic force by diminishing the charge releases the attached ions back to the solution. The taking up and release process can be utilised in desalination, as deionisation and regeneration¹⁰⁸. The Gouy-Chapman-Stern theory is often used to describe ion adsorption in EDLs^{107,110}. Rendering the Gouy-Chapman-Stern model, the double layer can be assumed to be divided into an ‘inner’ and ‘diffusion’ region. Illustrated in Figure 2.13, the inner region is labelled the Helmholtz layer¹⁰⁸ or the Stern layer¹⁰⁷. This is where ions directly cover onto the surface of the electrode. The Gouy-Chapman layer is a diffusion layer which is the region further from the surface of the electrode. This diffusion layer is where the distribution of electric charge is dependent on the voltage at the surface¹⁰⁸.

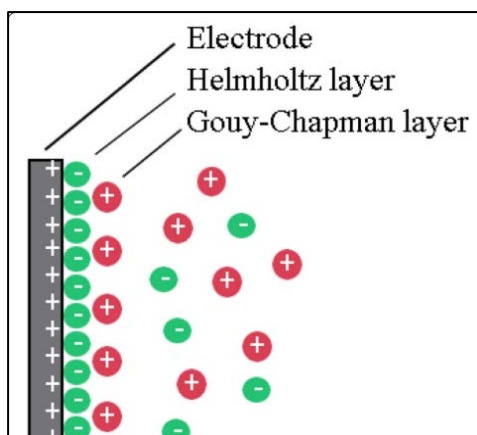


Figure 2.13: Charge distribution in Gouy-Chapman-Stern model¹⁰⁸

There are several models that mathematically describe the phenomena of adsorption in EDLs. Well-known models such as the Helmholtz and Gouy-Chapman-Stern models do not accurately describe ion adsorption for CDI^{38,107,111}. The Gouy-Chapman-Stern model is suitable for the non-overlapping, planar structure EDL¹⁰⁹. The Donnan model and its extended versions describe ion adsorption more accurately³⁸. The Donnan model assumes that the electrical potential in the micropores is constant¹¹¹. Two modifications need to be made in order to use the Donnan model for CDI. Firstly, a Stern layer should be included between the carbon electrode surface and the electrolyte, similar to the Gouy-Chapman-Stern model. Secondly, an attraction term (μ_{att}) should be included which will be used as a fitting parameter to describe ion adsorption in the micropores in the absence of electronic charge^{107,112,113}. The modified Donnan (mD) model is used to describe, theoretically, the equilibrium salt adsorption and charge in microporous carbons¹⁰⁹. The mD-model relates the ion concentration inside the carbon particles to the concentration outside the carbon particles¹¹⁴. It also assumes that the EDLs within the carbon particles are strongly overlapping to the point that it can be assumed that the potential in the micropores becomes constant. This means that the potential does not vary with the position in the pore¹⁰⁹. It was discovered that the mD model is problematic when describing multiple datasets in a range of values of the external salt concentration simultaneously¹¹⁴.

2.3.3 Electrode materials

In all CDI systems, the porous electrode is a key component. The CDI performance is determined by the material properties of carbon, as well as other system settings such as electrode thickness, spacer geometry, cell design, and operational settings¹⁰⁹. Johnson et al.

studied several carbon materials as electrode materials. Seemingly, the electrode material should be of large surface area in order to have a capacity high enough to hold a considerable amount of ions and be physically stable during the adsorption and desorption of the ions. Simultaneously, the electrode should have high electrical conductivity in order to complete the procedure swiftly¹¹⁵. The performance of carbon electrodes in CDI is also related to pore volume, pore size, pore connectivity and cost considerations¹⁰⁹. There are various carbon materials that are studied as candidates of electrode materials for CDI¹¹⁵.

Carbon material is a sizeable family representing an extensive range of materials that are primarily composed of the element carbon¹¹⁵. Activated carbon, carbon fibre, and carbon nanotubes are all examples of nanoporous carbon material and are ubiquitous and indispensable in a wide range of applications. This is due to their microporosity, large surface area, and high adsorption capacity. Moreover, activated carbons with selecting pore size contribution can separate target molecules by their variance in diffusion rate and adsorption capacity. Activated carbon is extensively used to eradicate environmental contaminants such as heavy metals and organic compounds in liquid phase¹¹⁶. Several carbon materials utilised for CDI will be reviewed in this section.

2.3.3.1 *Activated carbon*

Activated carbon (AC) powder is mainly produced via the pyrolysis of carbonaceous materials such as nutshells and wood¹¹⁵, coconut shells, coal, starch, or synthetic sources such as organic precursors or resins¹⁰⁹. Due to the low cost associated with AC, it is the preferred material used for CDI electrodes^{109,115}, and was the first electrode material used for electrosorption¹¹⁵. Aside from the low cost (~0.50 €kg⁻¹ or 8 ZAR·kg⁻¹) associated with activated carbon, it has a high specific surface area (SSA) in the range of 1000-3500 m²·g⁻¹, making this material particularly attractive for rife commercial applications. Generally, an increase in the total pore volume/SSA ensues a higher salt adsorption capacity¹⁰⁹.

2.3.3.2 *Carbon aerogels*

Carbon aerogels are nanosized air-filled foams with mainly carbon as a skeleton¹¹⁵. Typically carbon aerogels (CAs) have a moderate SSA ranging from 400-1100 m²·g⁻¹ but may go up to 1700 m²·g⁻¹, and high electrical conductivity (25-100 S·cm⁻¹). CAs have been synthesised in different forms such as powders, small beads, thin films, and monoliths and are composed of a network of dense carbon nanoparticles. Most of the total SSA is result of the interparticle pores (mesopores), however, depending on the synthesis conditions there may be micropores that are related to the intraparticle porosity¹⁰⁹.

2.3.3.3 *Ordered mesoporous carbons*

Ordered mesoporous carbons (OMCs) have an ordered uniform pore size ranging from 2-50nm¹¹⁵. OMCs show a highly periodic hexagonal or cubic arrangement of mesopores. This may enhance the transport of salt ions through the pore network. They can be derived through soft or hard templating¹⁰⁹. The hard-template method is when the uniform pore structure is achieved by attaching precursors onto certain templates with three-dimensional structures (silica and zeolite) and the template is removed after carbonisation. A soft-template method was introduced to overcome the time-consuming and expensive steps of the silica etching process. Thus, this method includes the direct assembly of organic amphiphilic surfactant or block copolymer templates with the carbon precursor¹¹⁵. Zou et al. did a study comparing OMC with AC electrodes. The study confirmed that using OMC as the electrode material for deionisation is effective compared to the salt-removing capability of AC¹¹⁷.

2.3.3.4 *Carbon nanotubes and graphene*

Carbon nanotubes (CNTs) and graphene have been investigated as materials for CDI electrodes¹⁰⁹. Both materials have a unique structure and possess extraordinary electrical properties. Graphene is composed of one-layer of graphite. Carbon atoms in graphene are shaped in a regular hexagonal pattern. Single-walled carbon nanotube (SWCNT) is composed of a graphene sheet rolled into a cylindrical shape. Multi-walled carbon nanotube (MWCNT) is made of more than two layers of graphene sheets. CNT can either be metallic or semiconducting depending on the arrangement of the hexagon rings along the tubular surface¹¹⁵. Lee et al. used CNTs as a conductive agent for the CDI electrode and found that the homogeneously dispersed CNTs illustrated enhanced electrochemical and desalination performance⁴⁰.

The carbonaceous electrodes are one of the key materials in CDI. Much research has been done to manufacture an electrode for CDI that has excellent characteristics in terms of electrical conductivity and pore distribution¹¹⁸. However, more needs to be done in order to lower the cost without compromising the performance of the porous carbon electrodes.

2.3.4 Operational considerations

2.3.4.1 CDI cell architectures

In this section, architectures that have previously been developed will be discussed. Many different cell architectures have been developed with the intention of augmenting energy efficiency¹¹⁹, salt adsorption capacity¹²⁰, electrode regeneration¹²¹, and ion removal rate¹⁰⁴.

- Flow-by electrode

Figure 2.14 A illustrates the first and historically most extensively used CDI cell architecture and is often identified as flow-by architecture^{45,109}, and has also been called CDI flow-between electrode¹⁰⁴. It consists of a pair of porous carbon electrodes separated by a spacer in which the feed water flows, allowing the feed water to flow perpendicular to the direction of the applied electric field¹²². This architecture was commonly used in a wide variety of works, including those exhibiting salt removal from diverging feed waters¹²³, investigation of the performance of novel electrode materials¹²⁴, or operating fundamental studies of salt sorption on porous electrodes¹¹⁰.

- Flow-through electrode

Johnson et al. developed a cell in the 1970s in which the feed flow was directed straight through the electrodes and parallel to the direction of the applied electric field¹²² as illustrated in Figure 2.14 B. For almost four decades, work on flow through CDI cell architecture was apparently abandoned until Avraham et al. used this CDI cell architecture in a three-electrode cell^{125–127}. This was done to study fundamental performance parameters such charge efficiency. The authors of this work noted that flow-through electrodes allow for faster cell charging relative to flow-by cell systems¹²⁵. The primary benefit of this architecture eliminating the need for a separator layer, allowing a minimisation of separator thickness, commonly from 200-500 μm to 10 μm ¹⁰⁴. Since the spacer thickness is reduced, more compact cells are tolerable with lower ionic resistance. The desalination process potentially becomes faster since the diffusion timescale governing salt removal between the electrodes is reduced¹²⁸.

Remillard et al. did work on a direct comparison of flow-by and flow-through capacitive deionisation. The authors concluded that generally, flow-by CDI cell architecture yielded superior performance compared to flow-through. They attributed the superior performance to; lower contact and setup resistance during operation, and fewer Faradaic side reactions, and thus less electrode oxidation⁴⁵.

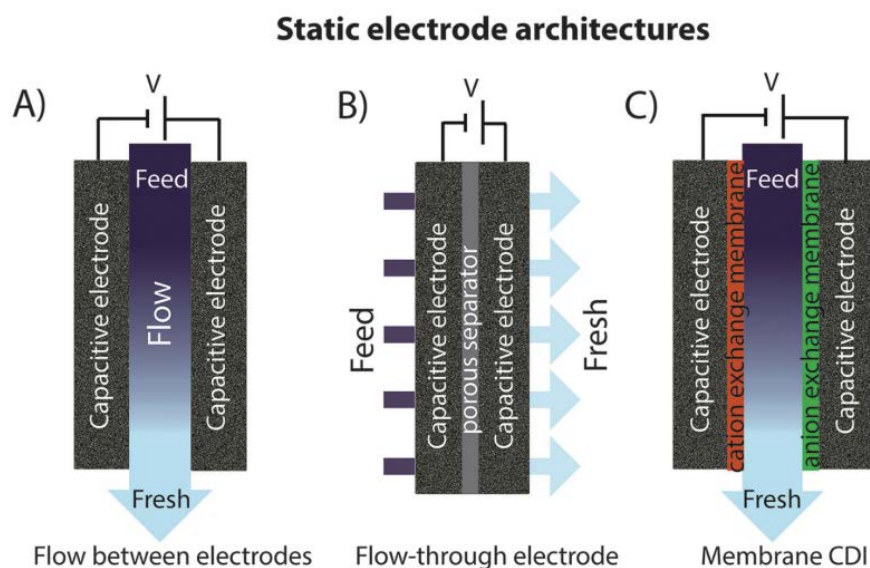


Figure 2.14: (A)–(C) CDI architectures using static electrodes, including: (A) flow between electrodes, (B) flow-through electrode and (C) membrane CDI¹²²

- Membrane capacitive deionisation

A significant variation in the elementary CDI cell architecture was established with the advancement of membrane CDI (MCDI). The first scientific demonstration of an MCDI system was done by Lee et al. in 2006 and was used to desalinate thermal power wastewater¹²⁹. In this cell architecture anion (AEM) and cation exchange membranes (CEM) are incorporated on the separator side of each electrode as shown in Figure 2.14 C to improve the selectivity of ions¹²⁹. This enhances the desalination efficiency and lowers energy consumption. This is a result of better ion selectivity and inhibition of co-ion desorption from the electrodes during the desorption process^{130,131}. The most often used configuration in MCDI is a free-standing CEM placed at the cathode, and a free standing AEM placed at the anode¹²². The utilisation of ion-exchange membranes (IEM) has allowed for the possibility to innovatively use MCDI for selective removal of ions. It has been reported that the application of ion exchange membrane resin produced electrodes showing improved selectivity towards nitrate and Li-ions from mixed solutions.^{129,132} Moreover, the introduction of membranes to the CDI cell shows a marked improvement of the charge efficiency compared to conventional CDI, Zhao et al. claim MCDI to be 4 times more efficient.¹³³ As of late, MCDI has seen intensive development, in the progression of theoretical comprehension^{134,135}, membrane materials, fabrication methods, and commercial applications^{136,137}.

MCDI requires less energy than conventional CDI. This is because in the CDI cell the “re-adsorbed ions” in the desorption process needs to be ejected in the succeeding adsorption

process resulting in additional energy consumption. While the introduction of ion-exchange material (IEM) adds resistance to the cell and amplifies the general energy consumption of the MCDI cell, the effects of higher regeneration efficiency overcome the effects of the increased resistance¹³³.

- Flow electrode

The concept of flow electrode CDI (FCDI) follows that of slurry-based electrodes developed for electrochemical energy storage systems such as the electrochemical flow capacitor¹³⁸. The suspended carbon material has the same role as the fixed carbon electrodes in a classic CDI process. This novel design allows suspended carbon to flow through a flow path existing between the IEM and the current collector, with the salt water passing through a spacer¹⁰⁵ as illustrated in Figure 2.15. When an electrical potential is applied between the current collectors in a FCDI cell, ions in the electrolyte migrate through the IEM, enter the flow-electrode, and are ultimately adsorbed onto the suspended carbon material¹⁰⁵.

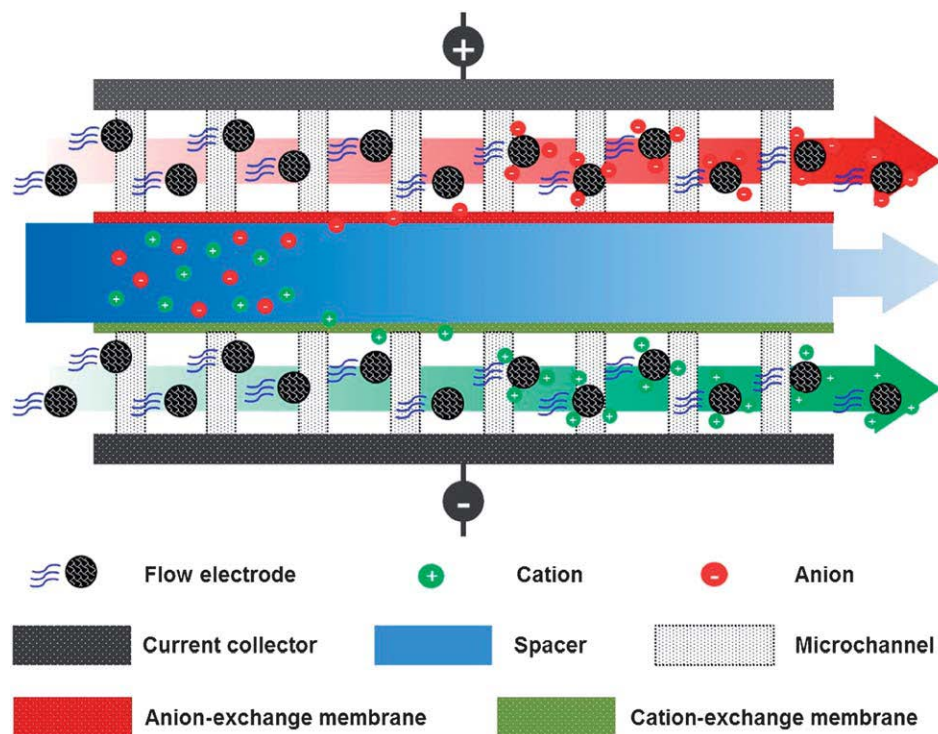


Figure 2.15: Schematic of FCDI process¹⁰⁵

FCDI has two key benefits relative to the static electrode CDI system¹²². Firstly, it can continuously desalinate feed water if the electrode material flows through the FCDI cell. Thus, no discharging step is required within the same cell¹⁰⁵, which is the case in a conventional CDI cell. Secondly, the continuously introduction of uncharged carbon particles into the cell increases the effective capacitance available for desalination¹²².

Flow electrode architectures

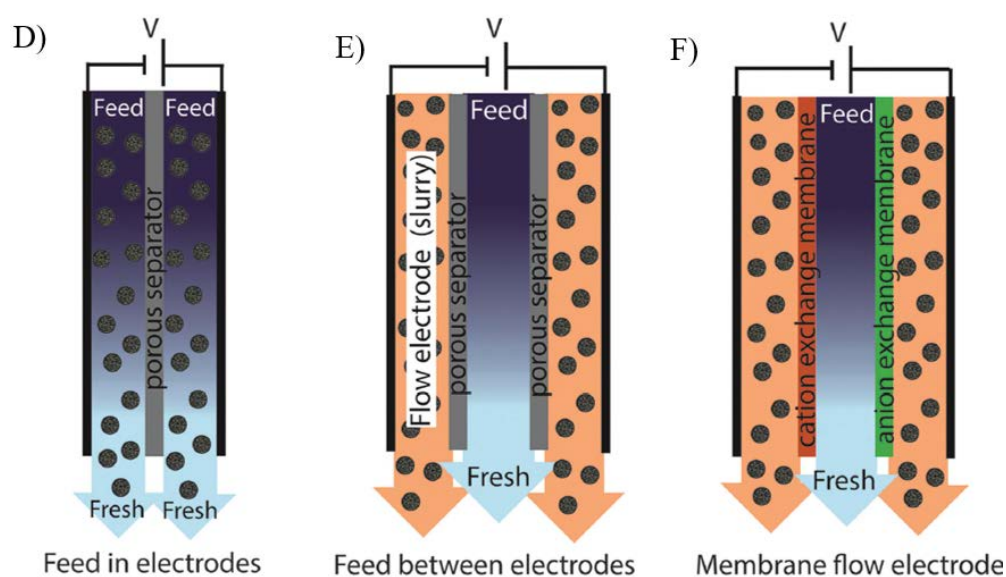


Figure 2.16: CDI architectures with flow electrodes, including systems with (D) feed-in electrodes, (E) feed-between electrodes, and (F) membrane flow electrode CDI¹²²

An FCDI cell architecture was proposed in 2014 by Hatzell et al. which desalinates without an IEM or a feed stream between electrodes¹³⁹ (see Figure 2.16 E-D). Lee et al.¹⁴⁰ did a study where the IEM was coated on the surface of a ceramic porous structure (spacer) to create a cell system whereby the IEM and spacer were combined into a single unit. The authors however faced the problem of blocking the pores of the porous ceramic structure when coating with the IEM. To resolve this problem two coating steps were applied to reduce the surface pore size before the IEM coating.

- Wire electrode

In 2012 Porada et al. proposed a method called “water desalination with wires”¹²¹. This is related to FCDI since it is another form of “electrodes in motion” through the utilisation of moving wires to accomplish desalination⁴¹. The wires used in this method was made of graphite having a rigid structure, and a length that was 40x their thickness¹²¹. Figure 2.17 illustrates the simple design of a wire-CDI cell³⁸. Graphite was chosen due to their inert and highly conductive properties in addition to being cost effective¹²¹.

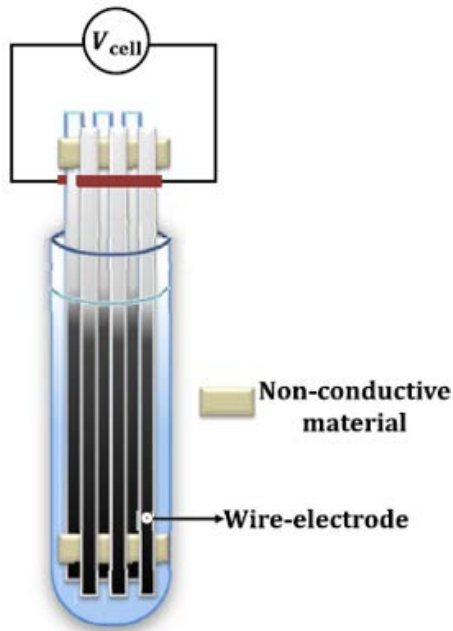


Figure 2.17: A wire-CDI cell³⁸

The cylindrical outer surface of the wires is coated with a porous carbon layer¹²¹. The graphite rod may also be coated with an optional outer coating of an ion-exchange membrane⁴¹. Two wires together form a “wire pair”. Figure 2.18 shows a schematic of the desalination process with wires. The “wire pair” is dipped into the feed water stream, and upon applying a cell potential difference between the wire-pair, the one of negative polarity adsorbs cations since it acts as the cathode with the other operating as the anode by adsorbing anions. The wire pair is manually lifted from the freshwater stream after some contact time in the solution and is brought into contact with what will become the brine stream. The electric field is removed or reduced and the stored ions are released into the solution causing the salinity to escalate¹²¹.

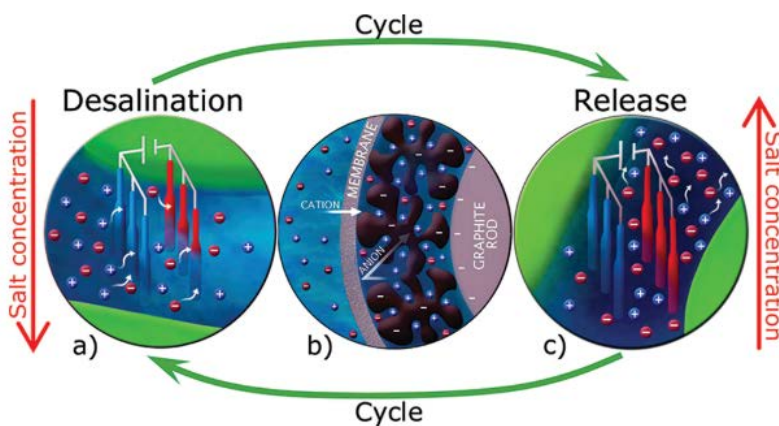


Figure 2.18: Schematic of desalination process with wires¹²¹

2.3.4.2 Single pass vs Batch mode

In order to determine the actual desalination of water by CDI, the change in ion concentration needs to be measured over time for all CDI cell designs. This can be done by analysing ion composition for water samples. Two methods are possible for the configuration of a CDI experiment, particularly the conductivity probe location, which is where the conductivity is measured¹⁰⁹.

First is the single-pass (SP)-method, see Figure 2.19 a, where water is fed from a storage vessel and the conductivity is measured at the exit of the cell^{109,124,135}. In this technique, soon after applying the cell potential, the conductivity (salinity) of the effluent will start to drop. However, later on, the measured conductivity of the effluent will increase again to the inlet value, due to the electrode having reached their adsorption capacity. The effluent water can either be discarded or recycled to a reservoir container. In order to ensure that the concentrations within the reservoir only slightly change within the adsorption half of the cycle (<1%), the reservoir needs to be large. Moreover, to ensure that during the cycle the influent concentration remains virtually constant. Using numeral integration of the effluent concentration vs time data, the total amount of salt removed can be determined^{109,110,124,135,141,142}.

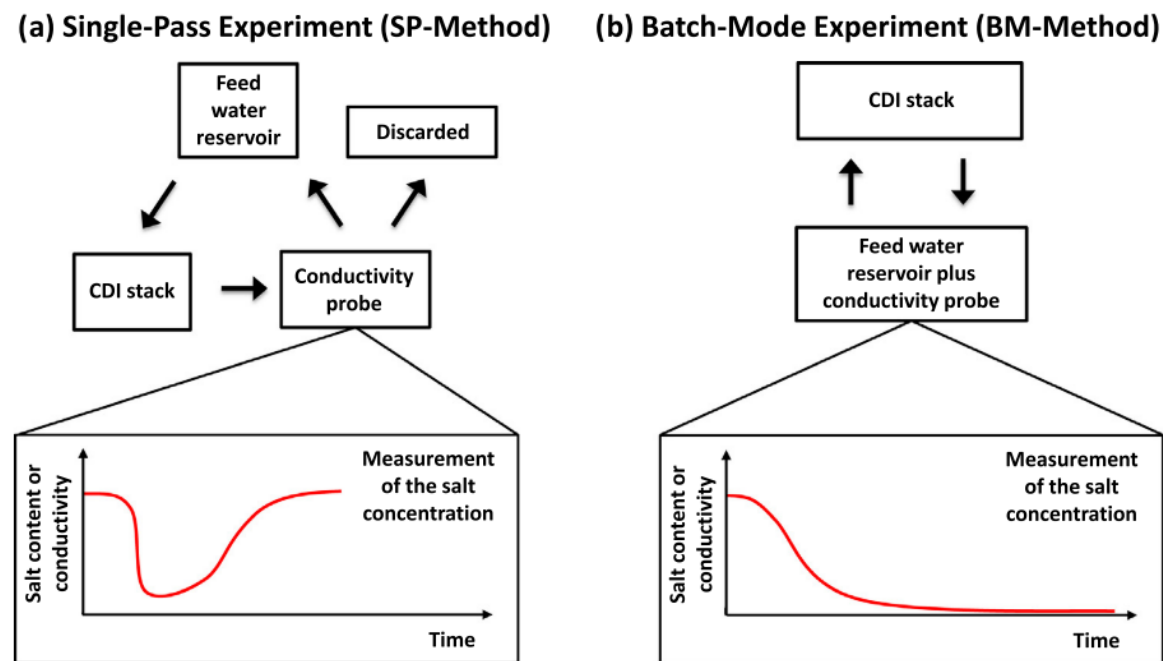


Figure 2.19: Schematic of CDI experimental design¹⁰⁹

Second is the batch-mode (BM)-method, see Figure 2.19 b. The BM-method is a common approach where the recycling reservoir is much smaller and is in the container where the conductivity is measured^{100,109,117}. In order to ensure that the change in salinity is low and is

measured accurately, the volume of the recycling reservoir needs to be small. In this method there is a steady drop in the measured salinity and levels off at a final, low value instead of having a minimum. To calculate the amount of ions removed from the water, the variation in salinity between the initial and final situation can be multiplied by the total water volume in the whole system¹⁰⁹.

BM-method analysis is simpler compared to SP-method. But there is a problem in the BM-method; the equilibrium salt adsorption is measured for a different reservoir concentration in each experiment. This is a challenge when one wants to compare data for equilibrium adsorption with the same salt concentration. For the SP-method this problem does not arise since all properties such as effluent conductivity and electrical current, are measured at well-defined values of the conductivity of the feed stream. In addition to this benefit, is the more reminiscent of a real CDI application this is, with the water to be treated only passing through the CDI cell once, instead of being recycled numerous times, which will be less efficient¹⁰⁹.

2.3.4.3 *Modes of operation*

Besides the choices around the desired architecture for the CDI cell, there are some options when it comes to selecting the mode of operation

- Constant Voltage Operation vs Constant Current Operation

There is a direct relation between the operation mode and the energy input of a CDI experiment. This is an important factor allowing CDI to compete with other conventional desalination technologies such as reverse osmosis. Generally, the operational modes consist of constant voltage (CV) and constant current (CC) modes^{7,90,143–145}.

When operating in CV operational mode, a constant voltage is applied to the cell. The concentration of the effluent tends to differ in time based on the variation in the amount of adsorption with time^{142,146}. For CV mode, there is two desorption modes; zero-voltage desorption (ZVD) and reversed-voltage desorption (RVD). ZVD is when the desorption step is set at a potential of 0V and is the standard operational mode in the scientific literature of CDI. RVD is when desorption step voltage is changed to values opposite in magnitude to that during the adsorption step. Figure 2.20 illustrates the advantage in desalination per cycle when using RVD-mode. Biesheuvel et al¹³⁵ presented the RVD operational mode and argued that RVD-mode is not possible for conventional CDI. That conclusion, however, was found to be premature and that CDI-CV-RVD is possible. ZVD-mode is at a disadvantage, because during the standard ZVD desorption, counterions are ejected from the electrodes into the spacer

channel. This reduction of counterions from the electrode region continues until the micropores become uncharged and the salt concentration in the macropores is approaching that in the spacer channel¹⁰⁹.

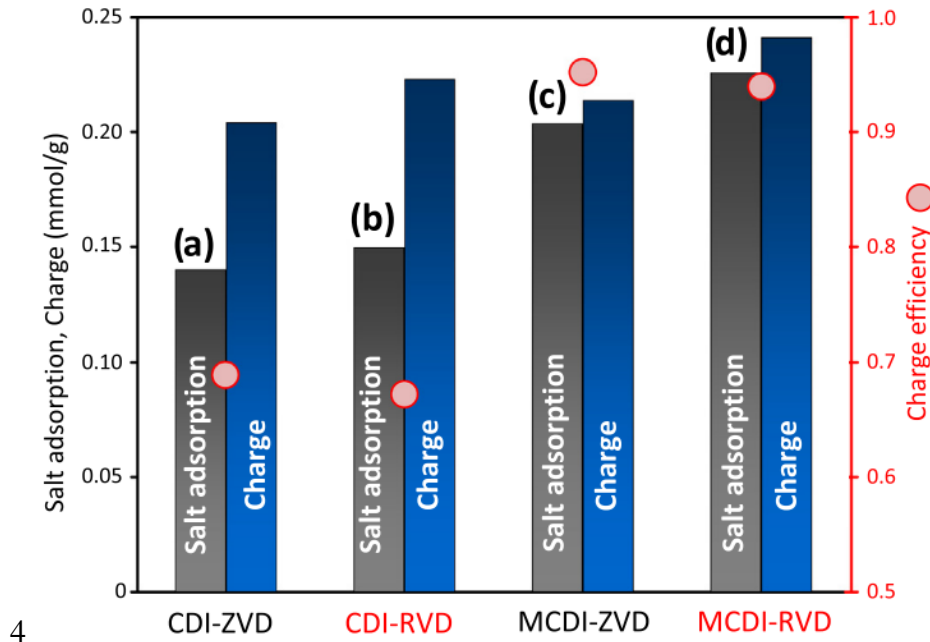


Figure 2.20: Comparison of salt adsorption and charge per cycle, and charge efficiency for CDI and MCDI with different CV operational modes¹⁰⁹

When operating in CC operational mode, a constant current is applied to the cell. Generally, in the cell the current flowing is proportional to the adsorbed amount. This makes it possible to maintain a constant salt concentration in the effluent when operating in this mode^{142,146}. In 2012, Zhao et al reported results of a desalination experiment done by supplying constant current to an MCDI cell. The effluent concentration was adjusted to the desired level by adjusting the flow rate and the current supplied^{142,146}. For Figure 2.21, the inlet salt concentration was 20 mM, flow rate 7.5 mL·min⁻¹. During adsorption, the current applied was 37A·m⁻² and during desorption -37A·m⁻². When the cell reached the upper limit of $V_{cell,max} = 1.6V$ the current is reversed from positive to negative. In CC-operation the effluent salt concentration level remains fairly constant, specifically at a constant low value during adsorption, and at a constant high value during desorption (see Figure 2.21)¹⁰⁹.

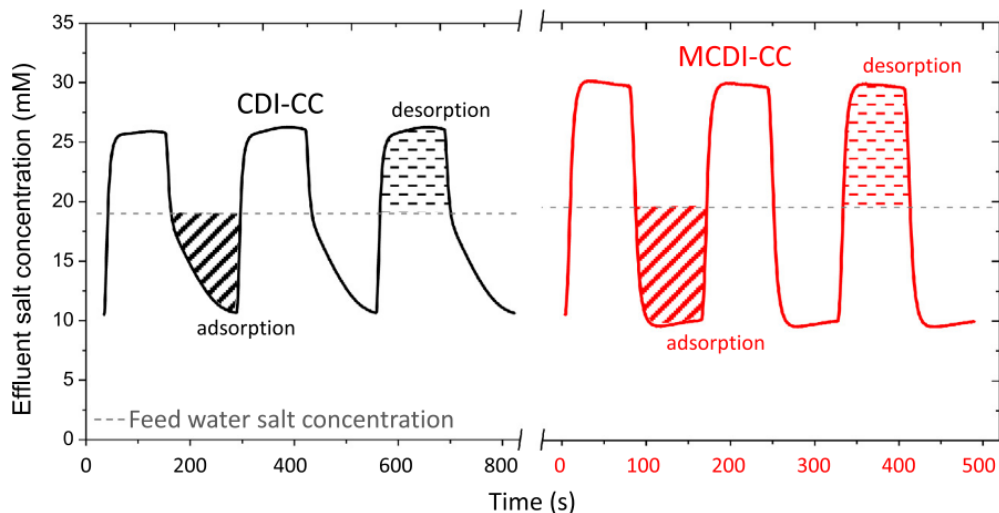


Figure 2.21: Effluent salt concentration for CC-mode of CDI and MCDI¹⁰⁹

There are various criteria to base the choice on whether to choose CV or CC mode, such as the purpose for a constant effluent concentration (CC in MCDI), or a low energy consumption of the experiment. It should be noted that this choice is only necessary for cyclic processes and not steady state operation of CDI with flowing electrodes¹⁴⁵. Between the two modes, in both the academic commercial and fields, reports on CV mode are more common^{7,90,143}. This is possibly due to the challenges faced when controlling voltage levels in CC mode¹⁴³. Zhao et al reported that MCDI had a lower energy requirement than CDI and that this difference is larger for CC-mode than for CV-mode, which correlates with higher dynamic charge efficiency for MCDI compared to CDI¹⁴².

CDI is based on a capacitive process. However, a capacitive process does not involve the transfer of charge across the electrode-solution interface; therefore Faradaic reaction may also occur (see Figure 2.22). In CDI these reactions can be unfavourable, as they¹⁰⁷:

- Lessen charge and energy efficiency of the process
- Could result in unwanted pH changes of the effluent solution since some reaction encompass the production and consumption of protons or hydroxyl ions. This can result in the precipitation of salt on membranes or into electrodes, thus affecting the long-term stability of the cell
- May result in oxidation of carbon, thus affecting the stability of the CDI desalination process.

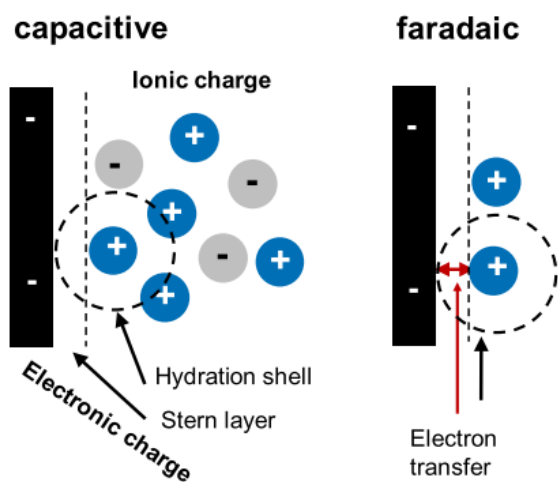


Figure 2.22: Capacitive and Faradaic processes¹⁰⁷

2.3.5 CDI applications

Desalination of brackish water is the most widely investigated application for CDI^{117,123,147–149}. In a laboratory, the majority of CDI experiments test CDI cell architectures and electrode materials using brackish feed water that is synthesised. Typically, the feed water is a solution of sodium chloride in deionised water¹⁰⁹. This allows for insightful, controlled experiments, however, they do not allow for reliable prediction of the performance during the continuous treatment of real brackish feed water. Xu et al. tested water that was collected from a natural gas operation site in the USA. The field tests indicated a stable performance of the carbon aerogel-based CDI system. Additionally, no deterioration was observed for the carbon aerogel electrodes¹²³. Kim et al. showed that MCDI could be used to treat brackish water having 0.005–0.010 g·L⁻¹ of oil compounds such as octane. The operation illustrated stable and reproducible adsorption and desorption capabilities¹⁴⁹. FCDI has an advantage of being able to desalinate feed waters with high salinity¹⁰⁵. CDI has also been used for other applications that require the removal of ions from an aqueous solution. Seo et al. investigated the removal of hardness ions using CDI. The CDI cell was used to remove divalent ions for water softening applications⁴³.

Furthermore, there has been several efforts to commercialise CDI. Lawrence Livermore National Laboratory (LLNL) in the USA emerged commercialisation efforts in the 1990s, however, this attempt was unsuccessful⁹⁹. Advances have been made since then⁴¹. Worldwide, several companies are developing CDI-related products. Companies that are leading in CDI activities are Voltea (Netherlands), AquaEWP (USA), Atlantis (USA), Idropan Inc. (Italy), LT Green Energy (Australia) and Enpar (Canada)¹⁵⁰. Voltea has developed MCDI-based systems

for commercial and domestic use. EST Water & Technologies (People's Republic of China) develops large-scale CDI systems (see Figure 2.23). A municipal wastewater reuse desalination plant is shown in Figure 2.23 A. This plant has a desalination capacity of 60 ML·day⁻¹. In Figure 2.23 B a coal mine waste water remediation plant is illustrated with a capacity of 5 ML·day⁻¹ ⁴¹. It is expected that worldwide, CDI technology will see an increase in funding by governmental organisations as well as equity investments in CDI. Voltea has received one of the largest equity investments, raising more than US\$ 10 million in two rounds of investments¹⁵⁰.

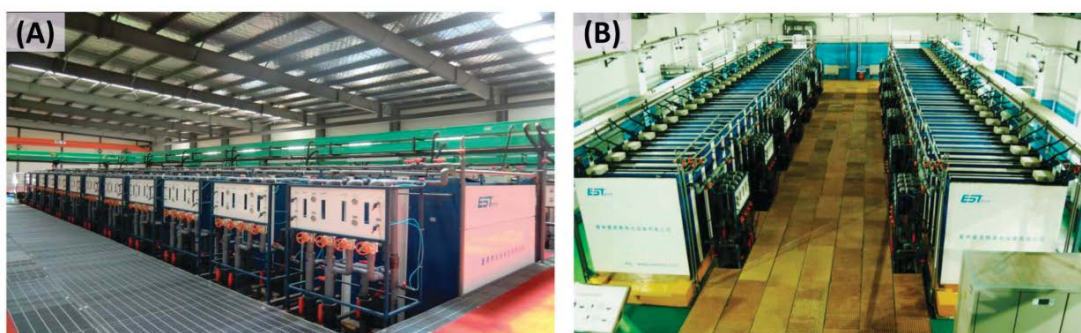


Figure 2.23: Large scale CDI desalination modules in China⁴¹.

2.3.6 Summary of literature review

Capacitive deionisation technology has been identified as a promising desalination technology that in theory consumes less energy than conventional water desalination technology such as reverse osmosis and multistage flash distillation¹⁵¹ but only at low salinities⁹³. The capacitive deionisation field has grown tremendously from a laboratory curiosity into a capable technology. In order for capacitive deionisation to reach its full potential, better comprehension is needed regarding the mechanisms of performance degradation and device failure. As the expertise in CDI application with more robust performance and stability enhances, the versatility of the method will grow⁴¹. The major challenge associated with CDI is cost. The high cost associated with CDI is mainly due to the low manufacturing volumes and immature process of manufacturing¹⁵⁰.

Much effort has been put on the electrode characteristics and optimising the operational conditions to further enhance the efficiency of capacitive deionisation¹⁵¹. Nearly five decades after first being introduced, CDI continues to be a stimulating and inciting field and can still be considered as an evolving technology. There are many trials that remain in the understanding of the capacitive deionisation method. However, investigations should continue concerning the

optimisation of the capacitive deionisation electrode composition, and synthesis as well as operational conditions. Essentially, in order to ensure that CDI get more recognition, CDI electrodes need to be optimised in order to desalinate water at higher salinities, while simultaneously lowering the capital cost of the CDI cell, as compared to RO, the capital expenditure for a CDI plant is high ¹¹⁹.

2.4 Research aims and objectives

This research work seeks to select the most appropriate processes and materials to produce electrodes showing optimal performance in a MCDI process. The optimal electrode composition and synthesis approached will be determined through analysis of the salt removal capacity and the rate at which the electrodes absorb and desorb ions.

MCDI systems using electrodes with optimised adsorption performance capacity require less electrodes, less seals, less current collectors and less spacers. Knowledge to produce high performance CDI electrodes shows clear potential for the reduction of overall water treatment cost, which fits in with the United Nation's sustainable development goals to provide access to appropriate quality water to all.

Main objectives outlined:

- Optimise ink/slurry composition and;
 - ratio between activated carbon, carbon black, PVDF binder and DMAC
 - Stirring mechanism of the ink
- Optimise CDI electrodes manufacturing technique which includes;
 - Spray coating
 - Slurry impregnation
 - Additional electrode treatments (thermal or pneumatic)
- Analysis of the produced electrodes;
 - Specific surface area by N₂ adsorption
 - Conductivity by 4 point probe method
 - Wettability by determination of the contact angle
 - Maximum salt adsorption capacity (mSAC)
 - Average salt adsorption rate, (ASAR)
 - Charge efficiency

- Optimize operational parameters of CDI cell

The application of MCDI on mildly saline water resources such as ground water is expected to yield potable water with an energy consumption below $0.5\text{kW}\cdot\text{h}\cdot\text{m}^{-3}$, showing great potential to produce more affordable potable water. One known drawback for MCDI is its relative high capital cost and a reduction of the electrode cost is required to make MCDI a more widely applied desalination technology.

3 Experimental Methods

This chapter gives a descriptive explanation on the experimental work performed. The methodology chapter is divided into two sections, electrode production and electrode characterisation.

3.1 Electrode production

Electrode production involves the synthesis of ink/slurry which is then transferred onto/into a substrate. CDI electrodes consist of four components;

1. Active material; YP80F and/or YP50F
2. Binder; Polyvinylidene fluoride (PVDF).
3. Additives that improve electrical conductivity; Carbon black
4. Substrate; carbon paper which is a non-woven electro conductive carbon fibre based porous material.

Three different methods were used to transfer the ink/slurry onto/into the substrate; slurry infiltration (SI), infiltration ink dropwise (IID) and spray coating (S).

3.1.1 Ink preparation

Ink/slurry preparation starts with the production of the binder solution; the process is described in 3.1.1.1. To prepare the electrode ink/slurry, activated carbon, carbon black (conductive additive), and PVDF (binder) were utilised; the process is explained in 3.1.1.2.

3.1.1.1 Binder solution preparation

In order to prepare 25 mL of 5wt % PVDF binder solution, 23.50g of N-N-Dimethylacetamide (DMAC) solvent was weighed out and added into a 100 mL glass bottle and heated on a hot plate to 110 ± 10 °C. 1.24 g of PVDF powder was weighed out before and slowly added to the heated DMAC and stirred vigorously to ensure the powder had completely dissolved. The prepared binder solution was then stored at room temperature in a closed container. The preparation of the binder solution was done in a fume hood due to safety concerns of the DMAC solvent since it is harmful when inhaled.

3.1.1.2 *Slurry/Ink solution preparation*

The slurry/ink that was prepared in this work, was dependent on the type of deposition method that was used. In the case of using the calendaring/rolling press to deposit the active materials into the substrate, a slurry was made. In the case of spray-coating or infiltration ink dropwise, an ink was prepared, since it required the addition of more solvent. All slurries were prepared using the body of a 20 mL syringe as a container. The nozzle of a clean 20 mL syringe was closed off by burning the tip with a fire lighter to ensure none of the ingredients escaped. All inks that were prepared were initially mixed in a syringe and upon the addition of the solvent were transferred into a 100 mL glass bottle. Slurries/inks **1-17** were mixed using an overhead stirrer, while slurries **18-31** were mixed using a devil shaker.

The slurry underwent a two-step mixing process. First the dry ingredients, activated carbon (0.72 g) and carbon black (0.09 g) powders were transferred into the body of the 20 mL syringe and mixed for 60 minutes (dry mixing) at a speed of 333 rpm using an overhead stirrer. According to Kwade and Haselrieder¹⁵² using an intensive dry-mixing mechanism for 60 minutes results in a slurry having a lower viscosity (1.5 Pa·s) compared to when mixing for 5, 15 or 30 minutes (3, 2.5 and 1.75 Pa·s, respectively). The second step included the addition of the PVDF binder solution (1.18 or 1.81 g) and 2-3 mL of DMAC solvent. The required amount of binder solution was added to the activated carbon/additive mixture in order to get a weight ratio AC:PVDF:CB of either 83:7:10 or 80:10:10. This was further mixed for 30, 60 or 120 minutes. When using the overhead stirrer for mixing it was discovered that due to the limiting movement of the overhead stirrer not all the materials in the syringe partook in the mixing process. This resulted in one having to first hand agitate the materials in the syringe for 5 minutes followed by using the overhead stirrer to complete the wet mixing process. This issue was resolved when using the devil shaker with the addition of the 10 mm zirconia ball. The syringe and its contents were closed off with the plunger and placed into an in-house prepared holder (see Figure 3.1). The addition of the zirconia balls was to enhance the mixing of the different ink ingredients. The holder was then placed into a devil shaker and was mixed for 60 minutes to complete the dry mixing process. As mentioned previously, intensive dry-mixing for 60 minutes results in a slurry having a lower viscosity. DMAC solvent was finally added, the amount determined through heuristics (2-3 mL) and was stirred for an additional 30, 60 or 120 minutes.



Figure 3.1: Holder for slurry preparation and devil shaker

Inks that were prepared in this work followed the same dry-mixing procedure as the slurries. After being dry-mixed, the ingredients were transferred to a 100 mL glass bottle. PVDF binder solution (1.18 or 1.81 g) and 22 g of DMAC solvent was added. Inks were magnetically stirred for 60 minutes, followed by being ultra-sonicated for 30 minutes using the Bandelin Sonorex RK 514 BH ultrasonic bath. Table 3.1 details the slurry/ink composition and the amount of material used for each slurry/ink prepared.

Table 3.1: Slurry/ink composition and amount of material utilised for each prepared ink

Slurry/ Ink no.	Activated carbon		Additive		Binder		Solvent		Composition (%)
	Type	Mass (g)	Type	Mass (g)	Type	Mass (g)	Type	Amount (*)	
1	YP50F	0.73	Super-P	0.090	PVDF	1.23	DMAC	2 mL	83:7:10
2	YP50F	1.45	Super-P	0.182	PVDF	2.42	DMAC	44.5 g	83:7:10
3	YP50F	0.73	Super-P	0.100	PVDF	1.2	DMAC	22.08 g	83:7:10
4	YP50F	0.73	Super-P	0.090	PVDF	1.27	DMAC	22.08 g	83:7:10
5	YP80F	0.73	Super-P	0.090	PVDF	1.23	DMAC	3 mL	83:7:10
6	YP80F	0.73	Super-P	0.090	PVDF	1,23	DMAC	22.2 g	83:7:10
7	YP80F	0.73	Super-P	0.090	PVDF	1.22	DMAC	22.1 g	83:7:10
13	YP50F	1.45	Super-P	0.182	PVDF	1.82	DMAC	44.23 g	80:10:10
14	YP50F	0.73	Super-P	0.091	PVDF	1.82	DMAC	2 mL	80:10:10
15	YP80F	0.73	Super-P	0.091	PVDF	1.83	DMAC	2 mL	80:10:10
16	YP80F	0.73	Super-P	0.091	PVDF	1.84	DMAC	2 mL	80:10:10
17	YP50F	0.73	Super-P	0.091	PVDF	1.85	DMAC	22.1 g	80:10:10
18	YP80F	0.73	Super-P	0.091	PVDF	1.83	DMAC	2 mL	80:10:10
19	YP80F	0.73	Super-P	0.091	PVDF	1.83	DMAC	2 mL	80:10:10
21	YP80F	0.73	Super-P	0.091	PVDF	1.82	DMAC	2 mL	80:10:10
23	YP80F	0.73	Super-P	0.091	PVDF	1.83	DMAC	2 mL	80:10:10
24	YP80F	0.73	Super-P	0.091	PVDF	1.81	DMAC	2 mL	80:10:10
25	YP80F	0.73	Super-P	0.092	PVDF	1.82	DMAC	2 mL	80:10:10
31	YP80F	0.73	Super-P	0.091	PVDF	1.82	DMAC	2 mL	80:10:10

* (Amount of solvent larger than 10 mL were measured with a weigh balance)

3.1.2 Electrode substrates

Two different substrates were investigated in this study, namely JNT GDBL (JNT) and SIGRACET® GDL (SGDL). SGDL was less thick compared to JNT, according to the suppliers physical properties it had a thickness of 0.28 mm while JNT had a thickness of 0.40 ± 0.03 mm.

3.1.3 Ink deposition techniques

In this study three different methods were utilised for the production of the electrodes, slurry infiltration (SI), and infiltration ink dropwise (IID) and spray coating method (SC). All three methods will be discussed in the sections to follow.

3.1.3.1 Slurry infiltration by calendaring

First a 50 x 210 mm piece of substrate was cut and placed onto a piece of Teflon to prevent sticking and breakage of the substrate when passing through the rolling press. The slurry was transferred from the syringe onto the substrate and was spread out onto the substrate using a blade. The prepared slurry was then infiltrated into the chosen substrate using a MSK-HRP-MR100A rolling press (see Figure 3.2). The function of the rolling press was to force the slurry to infiltrate the fibrous substrate and to distribute the slurry evenly. The distance between the two rollers of the rolling press was 0.7 mm to accommodate for the thickness of the substrate as well as the addition of slurry.

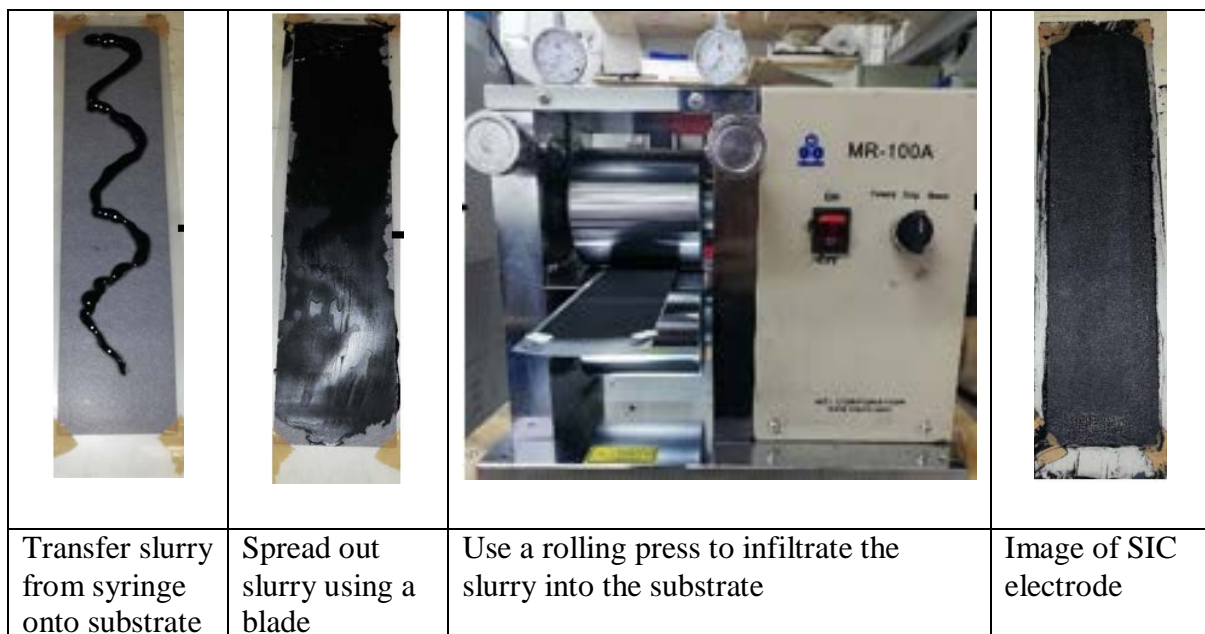


Figure 3.2: Slurry infiltration using the rolling press

In order to achieve a uniform spread of the slurry, each substrate was passed through the press six times. Some of the carbon fibres in the substrate would break under the pressure exerted by the roller press which becomes visible after more than 6 passes. The produced electrode was left uncovered in the fumehood at room temperature (25 ± 5 °C) so as to liberate the solvent.

3.1.3.2 *Spray coating*

A SONO-TEK ExactaCoat benchtop coating system (see Figure 3.3) was used to spray coat electrodes. It is a programmable automated XYZ motion ultrasonic coating system.



Figure 3.3: SONO-TEK spray coating machine

The parameters for the SONO-TEK ExactaCoat benchtop coating system are listed in Table 3.2. This set of parameters was adopted from fellow students of the HySA systems research group who have been using the SONO-TEK spray machine to deposit their carbon based ink slurries into carbon substrates to produce membrane electrode assemblies in a highly reproducible manner. The ink was loaded into the syringe and spray coating commenced onto the carbon substrate. Once spray coating was completed, the electrode was left uncovered at room temperature.

Table 3.2: SONO-TEK ExactaCoat parameters

Pressure (psi)	Path speed (mm·sec ⁻¹)	Spray rate (mL·min ⁻¹)	Area spacing (mm)	Spray head high (mm)	Platen temperature (°C)
0.86	50	0.5	4	48	150

3.1.3.3 Infiltration ink dropwise

This method of electrode production was based on work done by Lu et al.¹⁵³. The intention of their study was to develop a novel technology of formulating CDI electrodes in a manner that is easily manipulated and controllable. They reported that electrodes produced in this manner showed promising stability, high porosity and favourable hydrophilic property. In their work, a modified evaporation casting method was reported, which relies on a simple step-by evaporation of the slurry on a heated substrate. For the infiltration ink dropwise method, a substrate with a dimension of 100 mm x 105 mm, was placed inside a Petri dish on a heat plate inside a spray-coating machine. Making use of a Pasteur pipette, the ink was added onto the substrate in a dropwise fashion (see Figure 3.4). Two different temperatures ($25 \pm 5 \text{ }^\circ\text{C}$) and ($130 \pm 5 \text{ }^\circ\text{C}$) of the platen were selected on the basis of determining whether temperature influences performance of the electrodes.

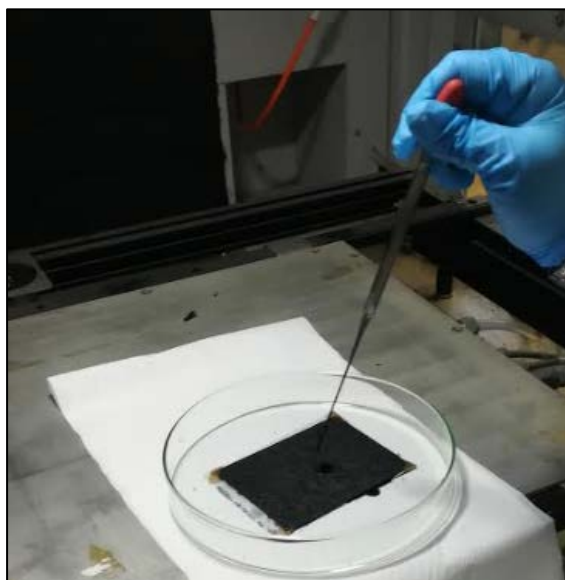


Figure 3.4: Infiltration ink dropwise

3.1.4 Electrode samples

For majority of electrodes drying occurred at RT *overnight*. Later in this work the drying was optimised by drying at different temperatures. Electrodes that were fabricated in this study were named using the following code, E- for electrode, followed by electrode number: I- for ink *or* S- for slurry, followed by ink or slurry number: activated carbon used: substrate used: conductive additive used. A Graphtec Cutting pro was used to cut a pair of electrodes with the required dimensions of 79 mm x 39 mm, after the drying procedure. Subsequently, all the electrodes were then characterised using the different techniques which will be discussed in

section 3.2, with the exception of E15 and E16. These electrodes were produced solely for BET analysis in order to investigate the influence of thermal treatment on the surface area.

Table 3.3: List of electrodes produced for this study

Electrode code	Electrode materials	Composition weight ratio	Electrode production method ^{a)}
E1-S1-YP50-JNT45-CB	YP50:PVDF:CB	83:7:10	SIC
E2-I2-YP50-JNT45-CB	YP50:PVDF:CB	83:7:10	SC
E3-I3-YP50-JNT45-CB	YP50:PVDF:CB	83:7:10	IID ^{RT}
E4-I4-YP50-JNT45-CB	YP50:PVDF:CB	83:7:10	IID ^{HT}
E5-S5-YP80-SGDL-CB	YP80:PVDF:CB	83:7:10	SIC
E6-I6-YP80-SGDL-CB	YP80:PVDF:CB	83:7:10	IID ^{HT}
E7-I7-YP80-SGDL-CB	YP80:PVDF:CB	83:7:10	IID ^{RT}
E13-I13-YP50-JNT45-CB	YP50:PVDF:CB	80:10:10	SC
E14-S14-YP50-JNT45-CB	YP50:PVDF:CB	80:10:10	SIC
E15-S15-YP80-JNT45-CB	YP80:PVDF:CB	80:10:10	IID ^{HT}
E16-S16-YP80-JNT45-CB	YP80:PVDF:CB	80:10:10	SIC
E17-I17-YP50-JNT45-CB	YP50:PVDF:CB	80:10:10	IID ^{HT}
E18-S18-YP80-JNT45-CB	YP80:PVDF:CB	80:10:10	SIC
E19-S19-YP80-JNT45-CB	YP80:PVDF:CB	80:10:10	SIC
E21-S21-YP80-JNT45-CB	YP80:PVDF:CB	80:10:10	SIC
E23-S23-YP80-JNT45-CB	YP80:PVDF:CB	80:10:10	SIC (130 °C) ^{b)}
E24-S24-YP80-JNT45-CB	YP80:PVDF:CB	80:10:10	SIC (250 °C) ^{b)}
E25-S25-YP80-JNT45-CB	YP80:PVDF:CB	80:10:10	SIC (350 °C) ^{b)}
E31-S31-YP80-JNT45-CB	YP80:PVDF:CB	80:10:10	SIC

^{a)} SIC=slurry infiltration by calendaring, IID=infiltration ink dropwise, ^{RT}=25±5 °C, ^{HT}=130±5 °C, SC=spray-coating

^{b)} Thermal treatment temperature

The electrodes were named using the following code; E- for electrode, followed by electrode number; I or S- for ink or slurry, followed by ink/slurry number. The code also includes the activated carbon type (YP50 or YP80) and the substrate which was used (JNT45 or SGDL). The CB indicates that carbon black was used as an additive.

3.1.5 Thermal treatment of electrodes

Differential scanning calorimetry/Thermogravimetric analysis (TGA/DSC) was carried out using a PerkinElmer Simultaneous Thermal Analyser STA 8000 (Massachusetts, United States). This was done to determine which temperatures to investigate. Approximately 3 mg of electrode was placed into the PerkinElmer Simultaneous Thermal Analyser. The analysis was done at a temperature of range of 50 °C to 350 °C, in the presence of argon gas at a flow rate of 100 mL·min⁻¹. Electrodes produced for these experiments had an ink mixing time of 30

minutes and were produced via the slurry infiltration by calendaring since these electrodes showed the most promising results in terms of desalination performance.

To thermally treat electrodes a furnace (Model HTF 028, KILN Contracts, Cape Town) was used (see Figure 3.5). This was done to determine the effect of thermal treatment on electrode characteristics including the desalination performance.

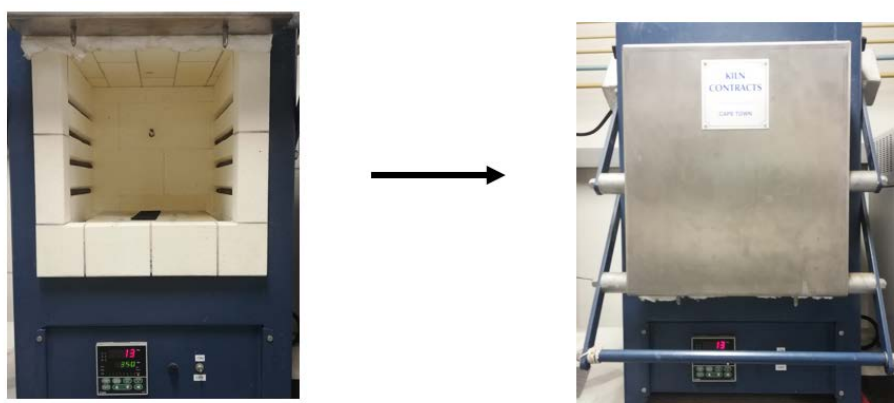


Figure 3.5: Furnace used for thermal treatment

3.2 Electrode characterisation

The produced electrodes were characterised using different techniques; four-point-probe measurements performed to determine the electrical conductivity, contact angle measurements to determine the hydrophilicity/hydrophobicity, N_2 adsorption to determine the specific surface area, pore distribution and pore volume, and chronoamperometry to evaluate the electro-sorption performance of the electrodes. Appendix A lists the different materials and reagents used, the specifications, purpose and supplier of the equipment. Appendix B lists the equipment used, specification, purpose and supplier of the respective components.

3.2.1 Electrode conductivity

Electrical resistivity and conductivity are physical properties that influence a material's electrostatic behaviour¹⁵⁴. Electrical resistance is a material's ability to oppose the electrons' flow (or electric current) when a potential is applied between two points of the material¹⁵⁵.

Electrical conductivity is the ease with which electrons flow through a material, and is the inverse of resistivity^{154,155}. The SI units for resistivity and conductivity are ohm (Ω) and Siemens (S) respectively. There are two different types of resistances that are relevant; surface and volume resistivity. Surface resistivity is the ratio of a potential difference to the current flow on the material surface¹⁵⁴. Volume resistivity is the ratio of potential difference to the current flow through the material¹⁵⁴. Surface and volume conductivity are the inverse of surface and volume resistivity. Surface resistivity and conductivity are relevant for textile surfaces such as knitted, woven and nonwoven fabrics¹⁵⁴. Volume resistivity and conductivity are utilised to characterise textile products like yarn¹⁵⁴. Low resistivity indicates a material that readily allows the movement of electrical charge¹⁵⁵. Various methods exist that measure resistivity. One of these uses a two point probe whereby a voltage is applied across a sample and an ammeter is utilised to measure the current. The resistance can then be calculated utilising Ohm's law presented in Equation 3.1. This method has its limitations however since the measured resistivity will not be the true resistivity of the material as it be too high due to the fact that it does not account for the resistance between the contact wires and the material or the measuring equipment. This is where the four point probe method comes in. As the name suggests, the four point probe method utilises four wires to measure resistivity (or sheet resistance). The measurement functions by passing a current (I) through the outer two probes, while simultaneously measuring the potential (V) produced across the two inner probes. The sheet resistance of the sample can be deduced by calculating the ratio of voltage to current. The advantage of making use of this method is that it ignores the contact resistance between the probe and the material¹⁵⁶. Equation 3.2 and Equation 3.3 are the equations responsible for calculating resistivity and conductivity, respectively.

$$R = \frac{V}{I} \quad \text{Equation 3.1}$$

$$\rho = \frac{RA}{L} \quad \text{Equation 3.2}$$

$$C = \frac{1}{\rho} \quad \text{Equation 3.3}$$

Where:

- R = Resistance (Ω) of electrode
- V = Voltage (V)
- I = Current (A)
- ρ = Resistivity ($\Omega.m$) of electrode
- A = Cross-sectional area (m^2) of electrode
- L = Probe spacing
- C = Conductivity ($\Omega.m$)⁻¹ or (S.m⁻¹) of electrode

Figure 3.6 illustrates the basic experimental four point probe setup. The length and width of the samples were measured using a ruler and the thickness was measured using a micrometre screw gauge. Once the parameters were established the sample was fastened into the probe using a screwdriver. A power source was connected to the outer probes and the inner probes were connected to a voltmeter. Once the setup was complete a current was applied by the power source. The resulting voltage on both the power source and the multi-meter were recorded. Subsequently the applied current was increased with set intervals from 0.1A to 0.3A with increments of 0.05A to yield at least 5 measurements per sample to get an average value for conductivity. The current range of 0.1A to 0.3A was chosen, because setting the current to a higher current range resulted in the sample being damaged as sparks appeared on the sample.

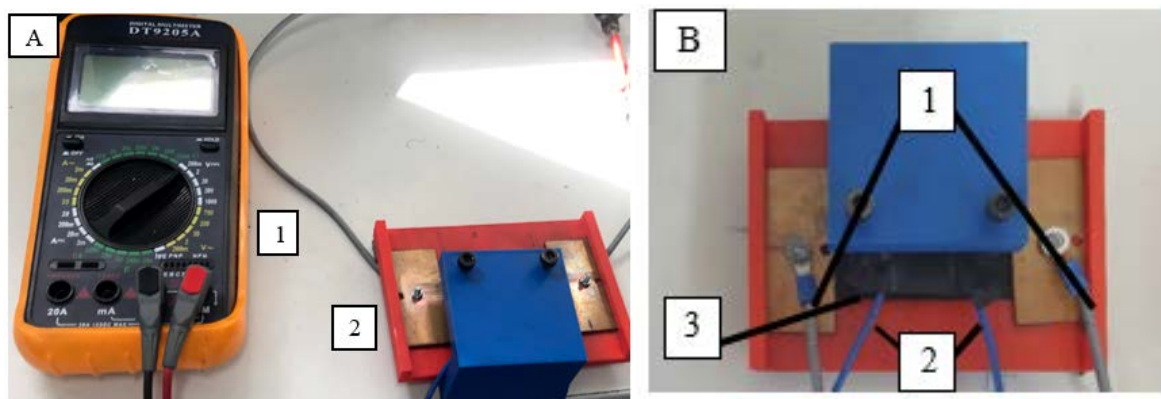


Figure 3.6: (A) Image of four point probe setup (1) multimeter, (2) four-point probe. (B) Close up illustrating the (1) outer probes, (2) inner probes and (3) the electrode

3.2.2 Contact angle measurements

Contact angle measurements were conducted to determine the wettability of the prepared electrodes. Non-woven fabric wettability is referred to as its ability to be wetted by liquid and is determined by the balance of the surface energy in the interface between air, liquid, and solid materials¹⁵⁷. Wetting is the initial behaviour when the sample is brought into contact with the liquid and involves the displacement of a solid-air interface with a solid-liquid interface¹⁵⁷. Thus, wettability is dependent on the chemical nature of the sample surface, geometry such as surface roughness and structure. The wettability of a sample is determined by the liquid contact angles¹⁵⁷. Table 3.4 gives a summary of the contact angle, degree of wetting and interaction strength between solid-liquid. A sample is termed hydrophilic if it has a wettable surface and hydrophobic if it has a non-wettable surface. Samples that have a contact angle greater than

150° are considered super hydrophobic since there is almost no contact between the liquid drop and the surface. A contact angle setup (see Figure 3.7) was designed in-house at SAIAMC and manufactured by Wake engineering.

Table 3.4: Contact angle summary

Contact angle	Degree of wetting	Interaction strength: solid-liquid
$\Theta = 0$	Perfect wetting	Strong
$0 < \Theta < 90^\circ$	High wettability	Moderate
$90^\circ < \Theta < 180^\circ$	Low wettability	Weak
$\Theta = 180$	Perfectly non-wetting	Weak

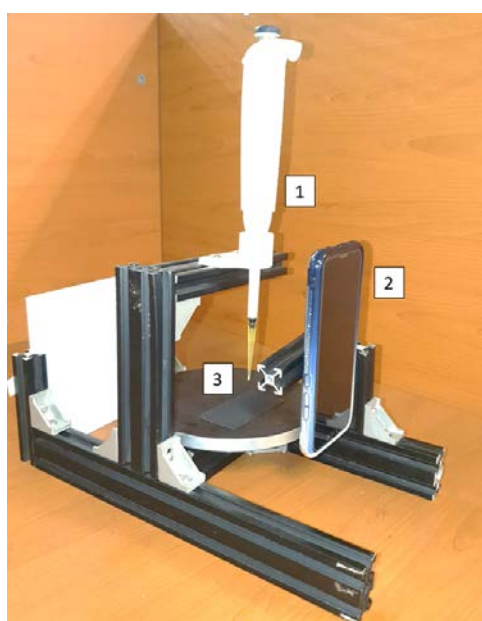


Figure 3.7: Image of in-house contact angle setup

For the contact angle testing, firstly, an electrode was placed on the base of the contact angle setup, (3) in Figure 3.7, then a HUAWEI P20 lite cellular phone was positioned (camera at the bottom) and kept in place using a magnet, (2) in Figure 3.7. Using the micro pipette (20 -200 μL), (1) in Figure 3.7, a 50 μL water droplet with 1 $\text{g}\cdot\text{L}^{-1}$ NaCl content was dropped onto the test electrode, finally using the HUAWEI P20 lite camera function an image was captured within 10 seconds of the water droplet making contact with the surface of the electrode. This process was done five times on the same electrode surface at different positions so as to obtain a more accurate measurement. The same procedure took place for the back surface of the electrode. Twenty images were taken for each electrode, and from these 20, an average contact angle was calculated.

Figure 3.8 shows the contact angle image for E24. ImageJ® software was utilised to analyse the pictures taken and to measure the contact angle. The angles on the right and left side of the water droplet were reordered. A label “L” correlated to the angle of the droplet on the left side, subsequently, a label “R” signified the angle of the droplet on the right side.

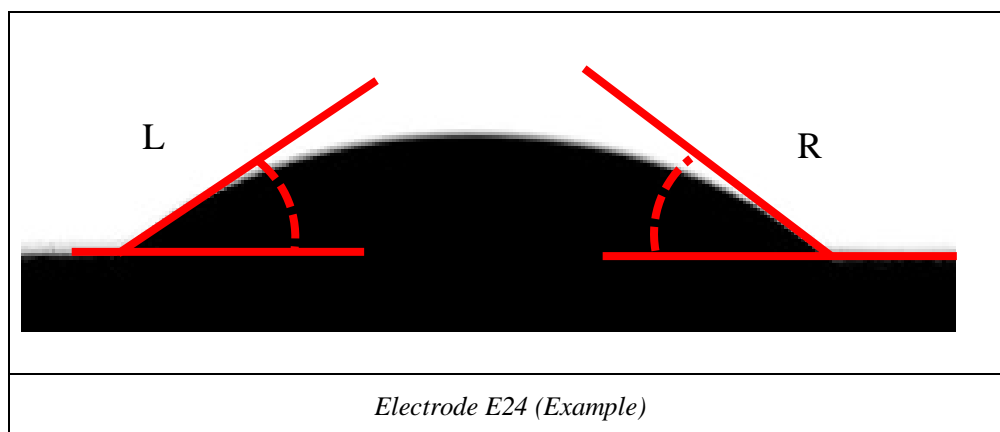


Figure 3.8: Contact angle measurements of electrode E24

3.2.3 Specific surface area N_2 adsorption

Specific surface area was determined using the Brunauer Emmet and Teller (BET) theory. Developed by Stephen Brunauer, Paul Emmet and Edward Teller in 1938, this theory aims to elucidate the physical adsorption of gas molecules on a solid surface and serves as the basis for an imperative analysis technique for the determination of the specific surface area of materials¹⁵⁸. The BET theory is applicable to systems having multilayer adsorption and typically uses probing gases that do not chemically react with material surfaces as adsorbates to enumerate specific surface area. The most commonly employed gaseous adsorbate utilised for surface probing by BET is nitrogen, and for this reason, standard BET analysis is habitually performed at the boiling point of nitrogen, 77K (-196°C) . This temperature is chosen as adsorption may only occur when the gaseous adsorbate is close to its boiling point. Other gaseous adsorbates include argon, carbon dioxide and water. Since BET is a scale-dependent property, quantities of specific surface area determined through BET theory may be contingent on the adsorbate molecule used and its adsorption cross section¹⁵⁹. Equation 3.4 shows the BET equation where v is the adsorbed gas quantity, p_0 and p are the saturation pressure and equilibrium pressure of adsorbates at the temperature of adsorption, respectively, v_m is the monolayer adsorbed gas quantity and c is the BET constant. Equation 3.5 and Equation 3.6 show the equation for the total surface area and specific surface area, respectively, where v_m is the monolayer adsorbed gas quantity in units of volume, N , is Avogadro’s number, s is the

adsorption cross section of the adsorbing species, V is the molar volume of the adsorbate gas and α the mass of the solid sample or adsorbent.

$$\text{BET equation: } \frac{1}{v[(P_0/P)-1]} = \frac{1}{v_m c} + \frac{c-1}{v_m c} \left(\frac{P}{P_0}\right) \quad \text{Equation 3.4}$$

$$S_{total} = \frac{v_m N s}{V} \quad \text{Equation 3.5}$$

$$S_{BET} = \frac{S_{total}}{\alpha} \quad \text{Equation 3.6}$$

In this study, the BET theory was used to determine the specific surface area and pore distribution in the carbonaceous materials used. Selected samples such as activated carbon and the prepared electrodes were weighed, placed into Micromeritics FlowPrep™ 060 oven apertures to degas utilising a low nitrogen gas flux of approximately 20 cm³.min⁻¹ for a minimum of 12 hours at 130°C in order to remove solvents and water trapped inside the porous structure. After degassing the sample loaded test tubes were anchored to a Micromeritics 3 Flex surface area and porosity analyser for surface area measurements conducted at -196°C utilising liquid nitrogen as the coolant. Since activated carbon is the main material in the electrode and the surface area is mainly based on the surface area of activated carbon, the surface area obtained was normalised to that of activated carbon.

3.2.4 Scanning electron microscopy

Scanning electron microscopy (SEM) is known to provide high-resolution electronic images of the surface of various materials by scanning with an electron beam. Additionally, the images' contrast provides information about the composition of the surface sample, as its various elements emit varying amounts of characteristic electrons¹⁶⁰. SEM is one of the most prevalent imaging techniques. SEM generates images by logging different signals resulting from interactions of the electron beam with the sample as it is scanned raster pattern across the sample surface¹⁶¹. The electrons used in SEM typically has an energy up to 40 keV¹⁶².

The morphology, topography, thickness and uniformity were studied using a HR-Carl Zeiss HRSEM-AURIGA microscope (Oberkochen, Germany). Samples for SEM analysis included pure PVDF, CB and AC-YP80F powders. A 60 minutes dry mixture of AC and CB and a slurry sample which was prepared as described in section 3.1.1.2, was also included. The slurry sample was dried in the furnace overnight at 130 °C as to remove the solvent since SEM requires samples to be imaged under vacuum, thus samples need to be dried. Two electrode samples which were prepared according to sections 3.1.3.1 (SI) and 3.1.3.3 (IID) were also

analysed using SEM. SEM sample preparation involved the immersion of electrode sample in liquid nitrogen and physically fracturing the electrodes to obtain a clear cross-section distinctly showing the electrode and substrate layers. All samples were then sputter coated with a carbon layer, using an EMITECH K950X Turbo Evaporator (Kent, United Kingdom), to enhance the conductivity of the electrodes and thus augment ultimate image visibility. Sample cross-sections were placed perpendicular to the electron beam for cross-sectional images and the same applied for surface images.

3.2.5 Membrane Capacitive Deionisation Cell Design, Description and Desalination Performance

3.2.5.1 Cell Design

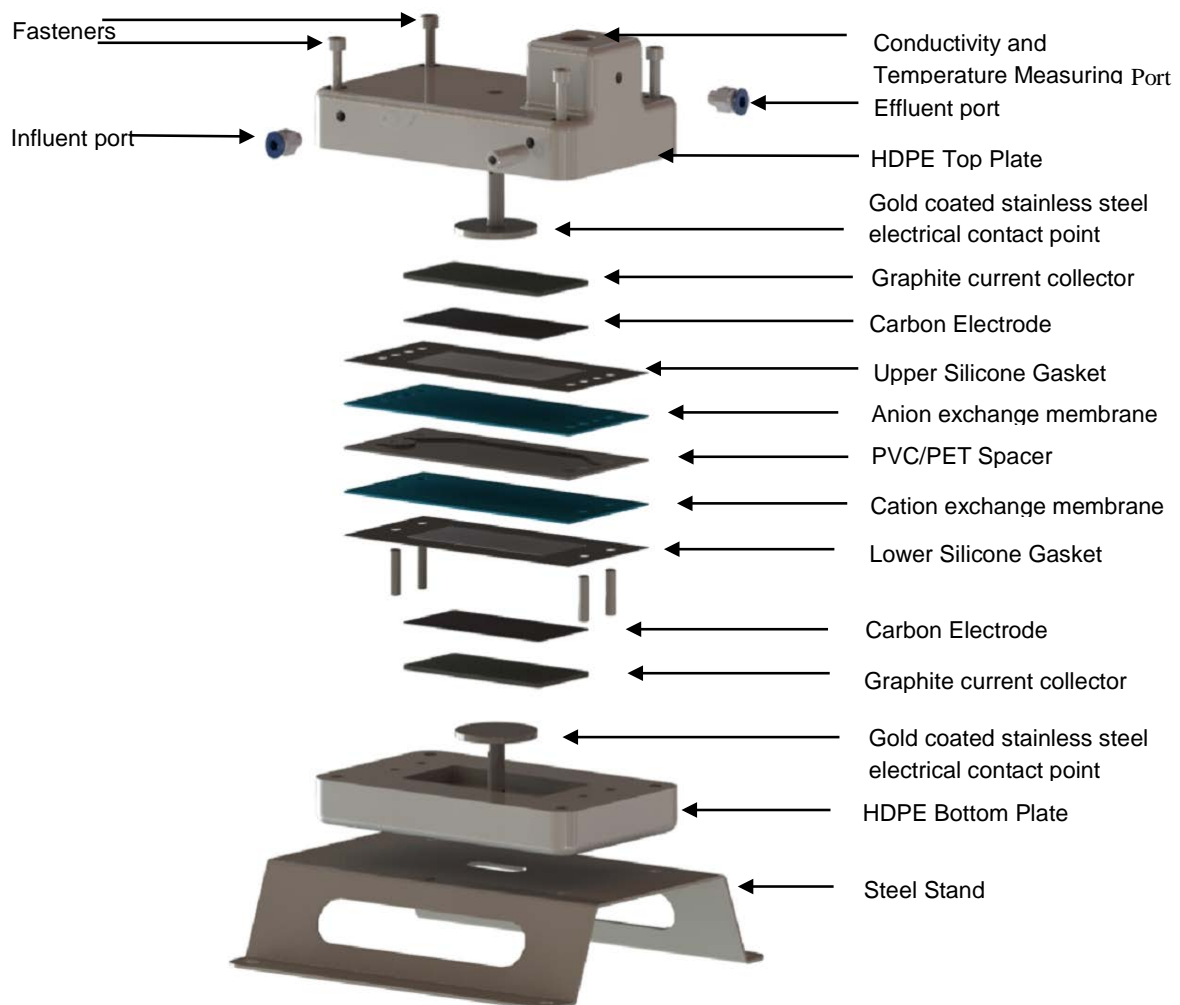


Figure 3.9: A detailed overview of the Membrane Capacitive Deionisation cell¹⁶³

Figure 3.9 illustrates a detailed overview of the MCDI cell. The MCDI cell included a single carbon electrode pair that was placed in a parallel configuration separated by a PVC/PET spacer, which served to provide sealed channels for a well distributed turbulent feed flow and limited pressure drop. Adjacent to the spacer were the anion and cation exchange membranes. The anion exchange membrane allowed transport of negatively charged ions whilst the cation exchange membrane allowed positively charged ions to traverse through. The carbon electrodes served to adsorb/desorb the negative and positive ions, and these were positioned between the ion exchange membrane and a graphite current collector. The graphite current collector provided the contact between the power source through the gold coated stainless steel disk and the electrode. The gold coated stainless steel disks, served as the electrical point of contact between the graphite and the power source. To prevent water from leaking out of the cell, two silicone gaskets were placed between the cell housing and the membrane. High-density polyethylene (HDPE), which is resistant to corrosion, was used to fabricate the housing of the cell. Fasteners (bolts and nuts) kept the cell components intact as the effluent and influent ports introduced and expelled the feed water to and from the cell respectively. The influent port allowed feed water to flow into the cell and then exit the cell through the effluent port. Appendix C and Appendix D respectively display the MCDI cell component dimensions and a list of materials that were used for cell construction¹⁶³.

3.2.5.2 *Cell Assembly Procedure*

Assembly of the MCDI cell entailed screwing the gold-coated electrical contact disks (ECD) on the inner side of the HDPE housing plates. Then the graphite current collector was placed on the gold-coated ECD followed by fixing the rubber gasket on the HDPE bottom plate of the cell. Subsequently, the electrode was placed on top of the graphite with its active side faced upwards. Next, the cation exchange membrane was fixed onto the cell ensuring all bubbles under the surface were removed. The PVC/PET spacer was placed on the cation exchange membrane ensuring that the influent and effluent flow path holes were aligned with the gasket flow holes. The anion exchange membrane was positioned next. The electrode with the active side facing down towards the spacer was deposited next followed by another graphite current collector. The HDPE top plate was positioned onto the stack of components, ensuring that the flow paths are not obstructed. The top and bottom plates were then fastened using bolts, washers and nuts. This was done carefully to make certain that too much pressure was not placed on the cell causing the breakage of cell components. A torque of 0.2 N.m using a torque wrench was applied to the gold coated ECD. The MCDI cell was placed on a stainless steel stand, the influent and effluent feeds tubes connected and the conductivity meter was inserted

into the conductivity and temperature port of the cell. Lastly, the terminals of the power source were connected through the ECDs using Hirschmann crocodile clips.

3.2.5.3 Electrode Desalination Performance Testing

- Experimental Desalination Setup

Figure 3.10 shows the experimental MCDI setup for the desalination of water. (1) Autolab PGSTAT320N, (2) Computer recording conductivity and current, (3) MCDI cell, (4) Peristaltic pump, (5) Conductivity meter, (6) Feed water, Effluent reservoir. To transfer the feed saline water, with a concentration of $1 \text{ g}\cdot\text{L}^{-1}$ NaCl, from a 3 litre feed reservoir to the MCDI cell a Watson-Marlow Sci-Q 300 Series peristaltic pump was used. The feed water was introduced into the cell through a silicone tube, “flowed by” the electrodes as the desalination occurred. Utilising the Nova 1.9 software package, the Autolab PGSTAT320N was programmed to supply a voltage to the MCDI cell for a given time of 87-minutes, while the resulting current was recorded. Simultaneously, the conductivity and temperature of the desalted water were measured utilising a Knick SE 204 4-electrode sensor accompanied by its corresponding conductivity meter and utilising Paraly SW112 software to collect the data. The desalinated water exited the cell and was recovered in a reservoir. All desalination experiments were performed in single-pass mode.

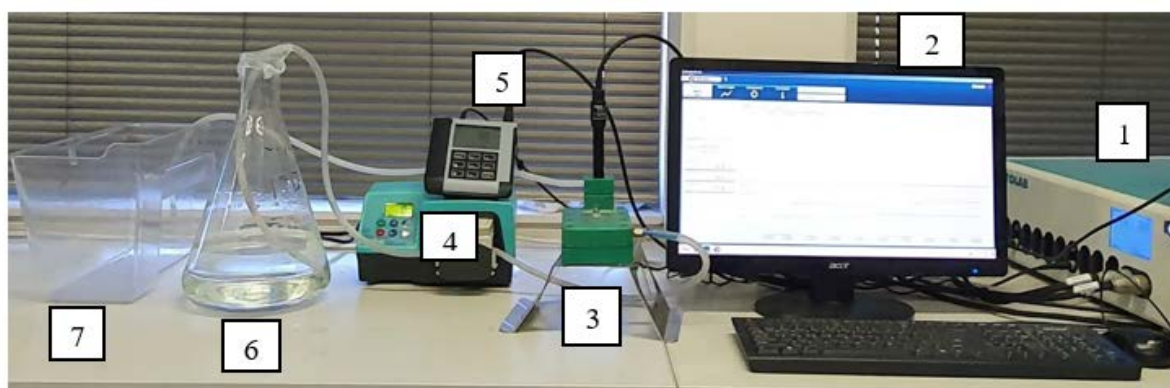


Figure 3.10: Image of MCDI setup¹⁶³

- Pre-Conditioning and Test Procedure

Produced electrodes were pre-treated by wetting before any adsorption-desorption measurements were executed. A feed solution of NaCl ($1\text{g}\cdot\text{L}^{-1}$) was prepared at the start of each desalination test. 3 g NaCl was weighed out into an Erlenmeyer flask with 3 L of mill-Q® ultrapure water. Nitrogen gas was used to flush the feed solution for 15 minutes to displace any dissolved oxygen that may result in the oxidation of the electrodes during the adsorption-desorption. Carbon electrode oxidation is undesired since it has a negative impact on the

performance and lifespan of a CDI system¹⁶⁴. The MCDI cell was assembled utilising the Cell Assembly Procedure described in 3.2.5.2 above. A constant voltage of 1.2 V for adsorption and -1.2 V for desorption was utilised for the adsorption-desorption measurements. The flow rate was set to 13 mL·min⁻¹ which corresponds to 9 rpm on the Watson-Marlow Sci-Q 300 peristaltic pump. All tests conducted were done in a single-pass method.

To evaluate each electrode pair, 7 adsorption-desorption cycles were conducted to pre-condition the MCDI electrodes. One pre-conditioning cycle ran for 360 seconds with 180 seconds adsorption (1.2V between anode and cathode) and 180 seconds desorption (-1.2V between anode and cathode). All desalination experiments were repeated three times in succession to determine the reproducibility of the MCDI cell.

Maximum salt adsorption capacity, capacitance and charge efficiency were determined by assessment of the conductivity, temperature, time and current data obtained from the measurement that succeeded the pre-conditioning procedure. The test consisted of 900 desorption seconds and 900 adsorption seconds. These times were selected based on results obtained from previous work on electrodes with similar dimensions and compositions. The results indicated complete electrode saturation and regeneration whilst using these times.

3.2.5.4 MCDI Metrics

Suss et al.⁴¹ explained in a review various metrics that can be utilised to evaluate the desalination performance of electrodes. In this section some of these metrics are listed and explained.

- SAC and mSAC

The salt adsorption capacity (SAC) is a metric used to evaluate the performance of MCDI cells. It is the salt adsorption per amount of active material in milligram per gram, which gives a measure of the salt adsorption performance of the electrodes. This value is dependent on the electrode material being studied, the charging voltage and the type of electrolyte and its corresponding concentration¹⁰⁷. The adsorption-desorption cycle can vary in duration, from very short (30 seconds) reaching only partial electrode saturation, to very long (up to 1500 seconds)¹²⁴ in order to measure the full electrode capacity. When the adsorption-desorption cycle is long enough to fully saturate the electrode, the maximum salt adsorption (mSAC) can be established. This is also known as the equilibrium salt adsorption capacity (eqSAC)⁴¹. The mSAC is an important metric to describe the MCDI cell performance as it is a measure of the maximum amount of salt adsorbed on an electrode in milligram per gram of electrode used in

the MCDI cell. The mSAC was calculated by integrating the reduction of salt concentration multiplied by the flowrate as a function of time multiplied by the molecular weight of NaCl divided by the mass of both electrodes, illustrated in Equation 3.7 below.

$$mSAC (mg \cdot g^{-1}) = \frac{Mw \times \int (C_i - C_o) \phi dt}{m_e} \quad \text{Equation 3.7}$$

Where:

- Mw is the molecular weight of NaCl 58.443 g·mol⁻¹
- C_i and C_o are the influent and effluent concentrations (mM) respectively
- φ is the flowrate (mL·min⁻¹)
- dt is the period of time during which charging occurred (min)
- m_e is the mass of both electrodes (g)

- Charge efficiency

Charge efficiency (λ) is defined as the ratio of charge equivalent to the total ions adsorbed at equilibrium over charge supplied to an electrode¹⁵¹. Charge efficiency would be unity if one salt compound is adsorbed from solution for each electron transferred from one electrode to the other. In practice, however, due to possible side reactions at the electrode surface, the charge efficiency tends to be less than 1. Charge efficiency is the ratio of the removed amount of ions multiplied by Faraday's constant to the total charge to the MCDI cell. It was calculated using Equation 3.8.

$$\text{Charge efficiency}(\lambda) = \frac{F \times C_{\text{esorp}}}{M_w} / Q_{\text{total}} \quad \text{Equation 3.8}$$

Where:

- F is Faraday's constant (F= 96 485 C·mol⁻¹)
- C_{esorp} is the electrosorption capacity of the electrodes (F)
- M_w is the molecular weight of NaCl 58.443 g·mol⁻¹
- Q_{total} is the total amount of charge applied during adsorption (C)

- Average salt adsorption rate

Since the mSAC only gives an idea of how much salt sorption is feasible, another metric is needed to provide information of the rate of salt sorption⁴¹. The average salt adsorption rate (ASAR) is the salt adsorption per cycle divided by the cycle time, which is the total duration of an adsorption and desorption cycle¹⁰⁷. This metric is reported in units of mg g⁻¹ min⁻¹, with “mg” referring to the mass of salt removed, “g” the mass of the active material of the electrode pair and “min” the charging time or total cycle time. ASAR can be calculated using Equation 3.9.

$$ASAR = \frac{SAC}{t}$$

Equation 3.9

Where:

- SAC is the salt adsorption capacity in $\text{mg} \cdot \text{g}^{-1}$
- t is the total cycle time in min

- Kim-Yoon for salt adsorption rate versus capacity

Kim and Yoon¹⁶⁵ proposed a new concept to evaluate the desalination performance in CDI called the CDI Ragone plot. This evaluates the desalination performance considering both the capacity and rate allowing for the intuitive acquisition of the overall desalination performance. In this plot the salt adsorption rate is plotted against the salt adsorption capacity. This ASAR vs SAC chart, later proposed as the “Kim-Yoon” (KY) diagram is a combination of the two key metrics in a single plot. This plot also allows for the optimal cell operational conditions, namely when both SAC and ASAR are close to their maximum attainable values. Figure 3.11 illustrates a Kim-Yoon plot obtained for a flow-by CDI cell with static film electrodes as a function of charging voltage.

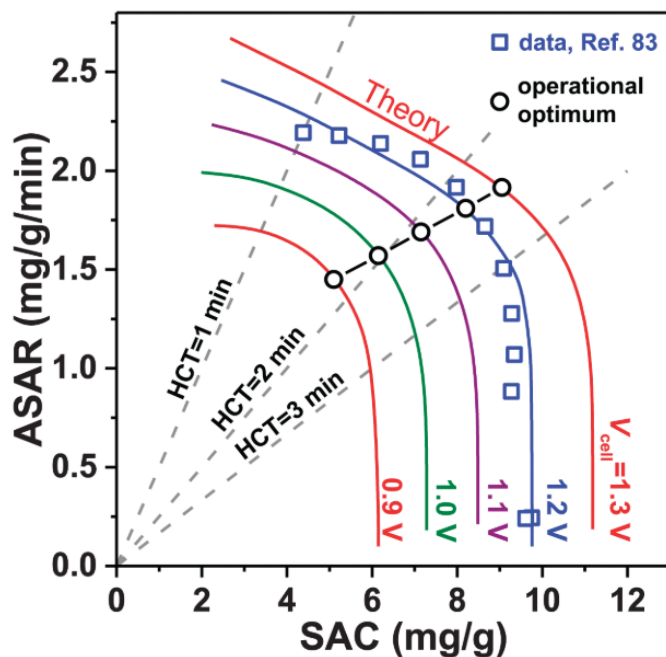


Figure 3.11: Kim-Yoon Plot for ASAR vs SAC⁴¹

4 Results and Discussion

In this chapter all results obtained for experimental work performed will be illustrated and discussed. Section 4.1 will focus on the results obtained related to the production of electrodes, using the different methods as shown in chapter 3. Section 4.2 will elaborate on the characterisation of the electrodes

4.1 Electrode Production

The results obtained for electrode production will be listed and discussed.

4.1.1 Samples produced

All slurries/inks were prepared as described in section 3.1. Table 4.1 lists the electrode samples produced in this study (as per Table 3.3) with its corresponding electrode weight and electrode pair weight.

Table 4.1: Electrode samples produced in this study with its corresponding electrode weight and electrode pair weight

Electrode code	Electrode materials	Composition weight ratio	Electrode production method ^{a)}	Electrode weight (g)	Electrode pair weight (g)
E1-S1-YP50-JNT45-CB	YP50:PVDF:CB	83:7:10	SIC	2.208	0.831
E2-I2-YP50-JNT45-CB	YP50:PVDF:CB	83:7:10	SC	6.390	1.413
E3-I3-YP50-JNT45-CB	YP50:PVDF:CB	83:7:10	IID ^{RT}	1.709	0.953
E4-I4-YP50-JNT45-CB	YP50:PVDF:CB	83:7:10	IID ^{HT}	1.811	1.178
E5-S5-YP80-SGDL-CB	YP80:PVDF:CB	83:7:10	SIC	1.257	0.688
E6-I6-YP80-SGDL-CB	YP80:PVDF:CB	83:7:10	IID ^{HT}	1.364	0.756
E7-I7-YP80-SGDL-CB	YP80:PVDF:CB	83:7:10	IID ^{RT}	1.863	0.852
E13-I13-YP50-JNT45-CB	YP50:PVDF:CB	80:10:10	SC	2.669	1.520
E14-S14-YP50-JNT45-CB	YP50:PVDF:CB	80:10:10	SIC	1.523	0.8788
E15-S15-YP80-JNT45-CB	YP80:PVDF:CB	80:10:10	IID ^{HT}	1.769	
E16-S16-YP80-JNT45-CB	YP80:PVDF:CB	80:10:10	SIC	1.333	
E17-I17-YP50-JNT45-CB	YP50:PVDF:CB	80:10:10	IID ^{HT}	2.071	1.228
E18-S18-YP80-JNT45-CB	YP80:PVDF:CB	80:10:10	SIC	0.942	0.942
E19-S19-YP80-JNT45-CB	YP80:PVDF:CB	80:10:10	SIC	0.929	0.929
E21-S21-YP80-JNT45-CB	YP80:PVDF:CB	80:10:10	SIC	0.865	0.865
E23-S23-YP80-JNT45-CB	YP80:PVDF:CB	80:10:10	SIC (130 °C) ^{b)}	1.627 (1.344) ^{c)}	0.795
E24-S24-YP80-JNT45-CB	YP80:PVDF:CB	80:10:10	SIC (250 °C) ^{b)}	1.517 (1.263) ^{c)}	0.775
E25-S25-YP80-JNT45-CB	YP80:PVDF:CB	80:10:10	SIC (350 °C) ^{b)}	1.693 (1.329) ^{c)}	0.834
E31-S31-YP80-JNT45-CB	YP80:PVDF:CB	80:10:10	SIC	1.593	0.961

^{a)} SIC=slurry infiltration by calendaring, IID=infiltration ink dropwise, ^{RT}=25±5 °C, ^{HT}=130±5 °C,

SC=spray-coating

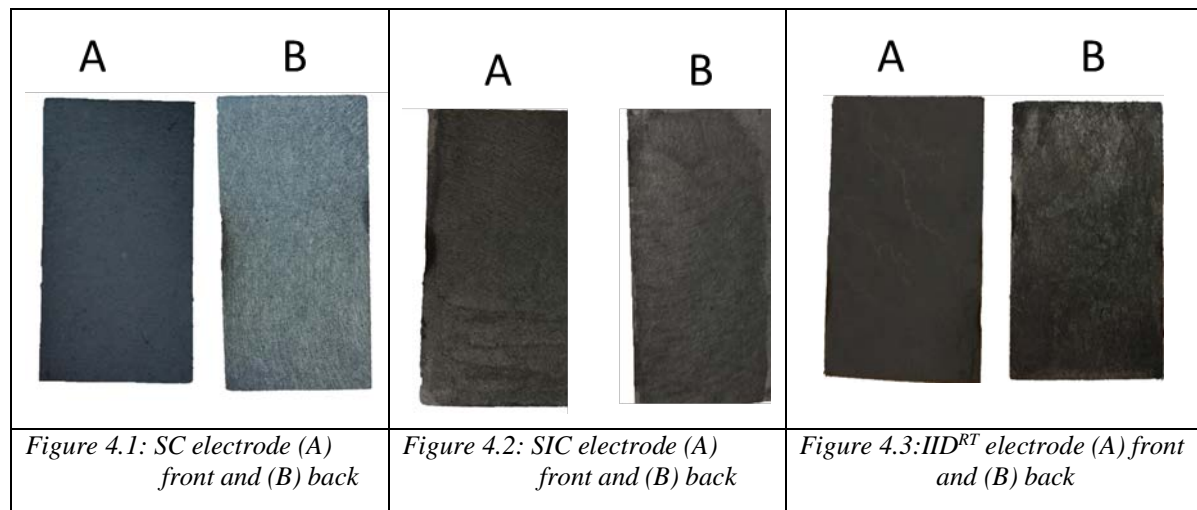
^{b)} Thermal treatment temperature

^{c)} Weight after thermal treatment

Electrode weight is defined as the weight of the electrode after production while electrode pair weight is the combined weight of 2 electrodes after being cut to size (79 mm x 39 mm).

From Table 4.1 it can be seen that electrodes produced via the slurry infiltration by calendaring method generally weighs less compared to electrodes fabricated using the infiltration ink dropwise and spray-coating methods. One of the reasons is that a substantial amount of slurry is left on the calendaring equipment.

Figure 4.1 shows a front (A) and back (B) side of a spray coated electrode. It is clear that the ink covers the front side only. The back side appears the same as the untreated substrate. On the contrary, the electrodes prepared by slurry infiltration by calendaring (SIC) and Ink Infiltration Dropwise (IID), see Figure 4.2 and Figure 4.3 respectively, show a great deal of ink/slurry penetration



As electrodes were being produced and the level of experience with each method increased, the weight gain of the electrode became more predictable. It also became clear that not all the solvent would evaporate at room temperature, even when the samples were left over night. Figure 4.4 shows the first attempt at producing the IID electrode at room temperature where all the ink was added without allowing drying periods in between. Figure 4.5 illustrates the optimised IID electrode at room temperature where the ink was added in small quantities to the substrate over a period of twenty-four hours to assure that the ink material would be transferred to the substrate

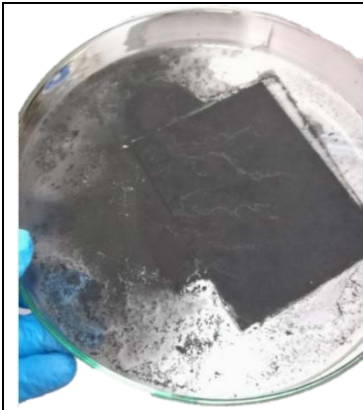


Figure 4.4: Infiltration ink dropwise electrode at $25 \pm 5 \text{ }^\circ\text{C}$



Figure 4.5: Figure 4.4: Improved Infiltration ink dropwise electrode at $25 \pm 5 \text{ }^\circ\text{C}$

4.1.2 Thermal treatment of electrodes

Figure 4.6 illustrates a TGA graph of an electrode which had an 80:10:10 (AC:PVDF:CB) composition. No phase changes is evident from the TGA, proving that no melting or crystallising changes occurred in the electrode. From the graph significant changes is observed at 130 °C and 250 °C. There is a 0.2 mg mass loss from 50 °C to 130 °C, which was attributed to DMAC solvent evaporation. At 250 °C there is a miniscule mass again of less than 0.025 mg, which may be attributed to analytical error. However, as the temperature increased above 250 °C the electrode seems to lose the mass it gained until it reaches the endpoint at 350 °C.

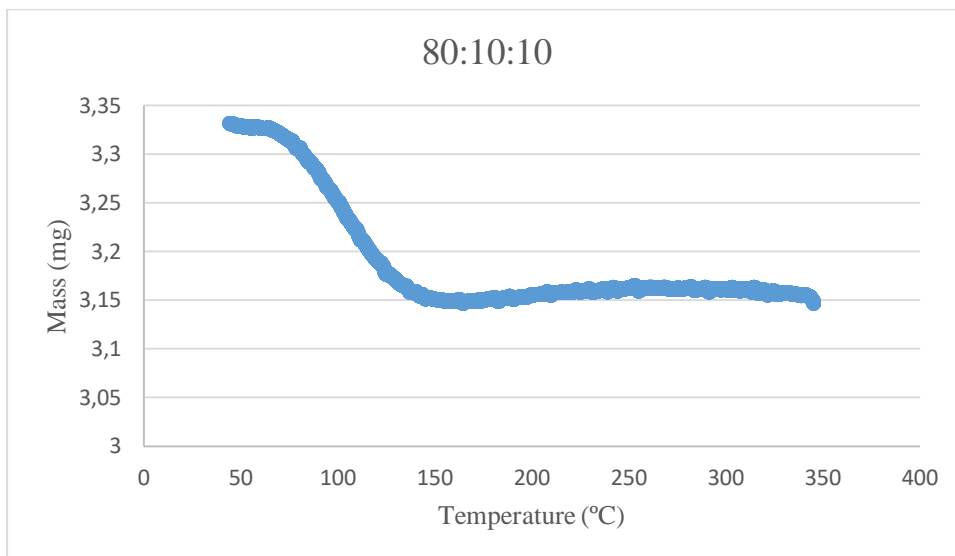


Figure 4.6: TGA Analysis of an electrode having an 80:10:10 composition

The TGA was important as it assisted the project in finding the optimal drying temperature for the electrode where all DMAC would be removed from the electrode, allowing the full surface of the activate carbon to become available for the capacitive deionization process.

4.2 Characterisation of electrodes

The results obtained from various characterisation techniques will be presented and discussed.

4.2.1 Electrode conductivity

According to Dong et al.¹⁶⁶ increased conductivity is beneficial for the fast transport of ions and the charge storage, which enhances the desalination performance. Table 4.2 lists the thickness and electrical conductivity for electrodes produced by different deposition methods. All electrodes were produced using substrate JNT45. Two different compositions of ink/slurry were applied; 83:7:10 (AC:PVDF:CB) and 80:10:10 (AC:PVDF:CB). As a reference, the conductivity of the untreated substrate JNT45 is also provided.

Table 4.2: Conductivity measurements of electrodes produced using 4 different deposition procedures and 2 different compositions

Electrode No	Deposition method	AC-YP80F	PVDF	CB	Thickness (cm)	Electrical Conductivity (S·cm ⁻¹)
		(%)	(%)	(%)		
JNT45	N/A	N/A	N/A	N/A	3.70E-02	61
E1	SIC	83	7	10	4.15E-02	49
E2	SC	83	7	10	5.25E-02	33
E3	IID ^{RT}	83	7	10	4.30E-02	43
E4	IID ^{HT}	83	7	10	5.00E-02	34
E13	SC	80	10	10	9.50E-02	21
E14	SIC	80	10	10	5.25E-02	30
E17	IID ^{HT}	80	10	10	7.00E-02	24

E1, produced using the SIC method, showcased the highest conductivity with a value of 49 S·cm⁻¹. E1 is 33% more conductive compared to E2, prepared using the spray-coating method. Thus, infiltrating the active material into the porous substrate instead of coating it on the surface is beneficial in terms of lowering the electrical resistance of the electrode. From E3 and E4, both produced using the IID method, it appeared that the temperature at which the electrode

was made had an impact on its conductivity. Preparing the electrode at a lower temperature (25 ± 10 °C) proved advantageous for the conductivity since it was 21% more conductive than when the electrode was prepared at a higher temperature (130 ± 10 °C). E2 and E4 only had a variance of $1 \text{ S}\cdot\text{cm}^{-1}$, both being prepared at higher temperatures (150 °C and 130 ± 10 °C, respectively). The faster evaporating solvent may have led to more active material being accumulated on the surface of the substrate, and thus created an electrode with a greater thickness. Since the substrate is the most conductive medium ($61 \text{ S}\cdot\text{cm}^{-1}$), it is expected that a substrate coated or impregnated with a less conductive medium will show an overall lower conductivity. Results for E13-E14 and E17 are consistent with what was observed for E1-E2 and E4 with an expected overall reduction of the conductivity. Increasing the PVDF (which is known to be an electrical insulator¹⁶⁷) binder ratio from 7 to 10 %, the conductivity was reduced by up to 39 % .

Thickness and conductivity measurements of electrodes on a SGDL substrate with an ink composition of 83:7:10 (AC:PVDF:CB) are listed in Table 4.3. The conductivity for the SGDL substrate is presented in the table with a value of $63 \text{ S}\cdot\text{cm}^{-1}$.

Table 4.3: Conductivity measurements of electrodes having different production methods with 83:7:10 composition on SGDL substrate

Electrode	Deposition method	Activated compound	Thickness	Electrical Conductivity
		Type	(cm)	($\text{S}\cdot\text{cm}^{-1}$)
SGDL	N/A	N/A	2.30E-02	63.2
E5	SIC	YP80F	2.45E-02	57
E6	IID ^{HT}	YP80F	3.20E-02	62
E7	IID ^{RT} R	YP80F	2.65E-02	53

The findings in Table 4.3 are in contradiction to those in Table 4.2. E5 was produced using the slurry infiltration by calendaring method and was expected to have the highest conductivity, if the trend in Table 4.2 were to be followed. However, this was not the case, although its conductivity value of $57 \text{ S}\cdot\text{cm}^{-1}$ is higher compared to E1, it was 8% less than E6 which was prepared using the infiltration ink dropwise method at high temperature. The reason for the contradiction could be the fact that a different substrate and activated carbon was used. It should be noted however that the SGDL substrate is mechanically not as strong as the JNT45. The stresses exerted onto the substrate during the calendaring process could have yielded a significant portion of broken fibres that could show a reduced conductivity. Unfortunately, there was no more SGDL sample left to calendar and test this hypothesis.

Table 4.4 tabulates the thickness and electrical conductivity for E23-E25. Treating the electrode at higher temperatures results in a minute decrease in the electrical conductivity. It can be concluded that thermal treatment at different temperatures does not have a significant impact on the electrical conductivity of electrodes.

Table 4.4: Conductivity and thickness of electrodes after thermal treatment at different temperatures

Electrode	Heat Treatment Temperature (°C)	Thickness (cm)	Electrical Conductivity (S·cm ⁻¹)
JNT45	N/A	3,70E-02	61
E23	130	3,75E-02	44
E24	250	3,95E-02	42
E25	350	3,85E-02	41

4.2.2 Contact angle measurements

A relation exists between contact angle measurements and the hydrophilic nature of the electrodes. A hydrophilic electrode is preferred as it can favour access of salty solution to the entire electrode resulting in an increased desalination performance. It should be noted that there are discrepancies in the contact angle measurements and its results should only be utilised to identify trends regarding homogeneity. Label “L” correlated to the angle of the droplet on the left side, subsequently, label “R” signified the angle of the droplet on the right side. A “front” of an electrode is the side to which the slurry/ink was applied also known as the active side in section 3.2.5.2 and a “back” side is the side to which no slurry/ink was applied.

Table 4.5 lists the contact angles for E4 as well as E13-E14 and E17. E4 had a composition of 83:7:10 (AC:PVDF:CB), utilising YP50F as the activated carbon and JNT45 as the substrate. E13-E14 and E17 had a composition 80:10:10 (AC:PVDF:CB), utilising YP50F as the activated carbon and JNT45 as the substrate. The contact angle of unmodified JNT45 substrate is also listed in the tables.

Table 4.5: Contact angle measurements of electrodes having different PVDF compositions

			Electrode 1 (°)		Electrode 2 (Duplicate) (°)		
			Front	Back	Front	Back	
Code	Deposition method	PVDF (%)	A	A	A	A	A (°)
JNT45	N/A	N/A	114	113	114	114	114
E4	IID ^{HT}	7	54	52	25	62	48
E13	SC	10	83	112	98	114	102
E14	SIC	10	94	113	95	104	102
E17	IID ^{HT}	10	88	103	80	104	94

With an average contact angle value of 114 °, it can be concluded that the unmodified JNT45 had a low wettability degree and a weak solid-liquid interaction.

From Table 4.5 it is evident that the amount of binder used impacts the hydrophilic nature. E4 and E17 were both produced using the infiltration ink dropwise method at 130 ± 5 °C while E4 had a PVDF composition of 7 % and E17 10 %. E4 with an average contact angle of 48 ° is more hydrophilic compared to E17 which had an average contact angle of 94 °. Adding more binder lowers the hydrophilic nature of the electrode. It should be noted that E4 was the first IID electrode produced at 130 ± 5 °C and the method of production was not optimised. This can be seen in the difference between the values of the front side of electrode 1 and electrode 2. Comparing E13-E14 and E17 the difference in the contact angles of electrode 1 and 2 a significantly less, this can be attributed to the method of production being optimised. From Table 4.5 it is observed that E17 which was produced via the IID method at a high temperature is the more hydrophilic, having a contact angle of 94° compared to E13 (101°) and E14 (102°). Thus, it can be concluded that the deposition method has an influence on the wettability properties of electrodes. From Table 4.5 it can be seen that the electrodes have a higher hydrophilicity on the front side of the electrode compared to the back side. This is to be expected since the slurry of activated material is applied only on one side of the substrate.

Table 4.6 tabulates the contact angle for electrodes having an ink composition of 80:10:10 (AC:PVDF:CB) and using YP80F as the active carbon. The deposition method used was slurry infiltration by calendaring and the substrate was JNT45 for E18-19 and E21. For these electrodes the mixing time of the slurry were investigated.

Table 4.6: Contact angle measurements of electrodes made with slurry having different mixing times

Electrode	Mixing time (min)	Electrode 1 (°)						Electrode 2 (Duplicate) (°)						A (°)
		Front			Back			Front			Back			
		L	R	A	L	R	A	L	R	A	L	R	A	
E18	120	63	68	66	92	98	95	61	61	61	96	97	97	80
E19	60	42	41	42	81	82	82	43	43	43	81	81	81	62
E21	30	49	46	48	70	70	70	42	45	44	61	61	61	56

L = Left side, R = Right side, A = Average from L and R

From Table 4.6 it is evident that mixing time has an impact on the wetting nature of the electrodes. The slurry used for E18 was mixed for 120 minutes resulting in this electrode being the more hydrophobic compared to E19 and E21. The contact angle for E18 was 23% and 30% more than that of E19 and E21, respectively. It is evident that the contact angles for the

electrode 1 and electrode 2 (duplicate) of each electrode sample listed in Table 4.6 are similar with only a few degrees variance, which confirms a reasonable reproducibility of the method. It is also evident that the contact angle the front side of the electrode is consistently smaller than the contact angle at the back side.

Contact angle measurements for E23-E25 are tabulated in Table 4.7 and also show that the electrodes have a higher hydrophilicity on the front side of the electrode compared to the back side. This is to be expected since the slurry of activated material is applied on the front side of the substrate.

Table 4.7: Contact angle of electrodes having different thermal treatment temperatures

		Electrode 1 (°)						Electrode 2 (Duplicate) (°)						A (°)
		Front			Back			Front			Back			
Electrode	Heat Treatment Temperature (°C)	L	R	A	L	R	A	L	R	A	L	R	A	A (°)
E23	130	35	37	36	43	43	43	34	37	36	52	59	56	43
E24	250	23	22	23	50	46	48	31	33	32	53	51	52	39
E25	350	0	0	0	0	0	0	0	0	0	0	0	0	0

From Figure 4.7 it can be seen that as the thermal treatment temperature increase from 130 to 350 °C, the contact angles decrease. E23 and E24 are considered to be highly wettable since they have average contact angles of 43° and 39°, respectively. E25, however, is considered perfectly wettable since its contact angle is 0°. Treating the electrode at higher temperatures results in an improvement in the capillary forces, which are responsible for pulling the liquid inside the particle¹⁶⁸. Another explanation for the perfect wetting nature of E25 is that when the electrode is treated at such a high temperature of 350 °C, the PVDF binder is to some extent altered chemically/physically¹⁶⁹. Sun and Feng¹⁷⁰ reported that thermally treating PVDF enhances the hydrophilicity of the binder. From Table 4.7 it can be seen that thermally treating an electrode results in improved hydrophilicity.



Figure 4.7: Contact angle measurements of E23-E25

It should be noted that when comparing the average contact angles of electrode 1 and electrode 2, the duplicate, in Table 4.5 there appears to be significant differences in their values. An

attempt was made to overcome this by passing an electrode more than once through the rolling press to ensure the slurry is more evenly distributed. This further strengthens the earlier statement regarding the discrepancies with contact angle measurements and how it should be utilised to identify trends such as homogeneity. The contact angle measurements listed in Table 4.6 and Table 4.7 shows that the electrodes are much more homogenous since the contact angles of electrode 1 and electrode 2 (duplicate) are very similar, with only a few degrees variance. The average left and right angles of 5 water droplets for the front and back side of an electrode are also listed in Table 4.6 and Table 4.7 when comparing these it can be seen that their angles are alike. This further strengthens the earlier statement claiming that passing an electrode six times through the rolling press is beneficial for the homogeneity of an electrode. However, more work needs to be done in order to prove this theory.

4.2.3 Specific surface area N₂ adsorption

BET analysis were performed for all carbonaceous materials and some electrodes that were fabricated in this thesis study. For the purpose of making a fair comparison, the surface area of all fabricated electrodes were normalised using the weight portion of the activated carbon of the sample. Normalised values are denoted in brackets with a superscript “n”. Figure 4.8 depicts the isotherms that were obtained for (A) YP-50F and (B) YP-80F. According to the International Union of Pure and Applied Chemistry (IUPAC) classification of adsorption isotherms¹⁷¹, YP-50F appears to have a reversible type I isotherm. This indicates the activated carbon is a microporous solid having a relatively small external surface area. The hysteresis loop at a relative pressure $P/P_0 = 0.4-0.9$ in (A) for YP-50F and $P/P_0 = 0.5-0.9$ for YP-80F showcases the mesoporous nature of the activated carbons. The initial part of the isotherms is credited to monolayer-multilayer adsorption. Both YP-50F and YP-80F appear to have a type H₄ hysteresis which is often associated with narrow slit pores including pores in the micropore range.

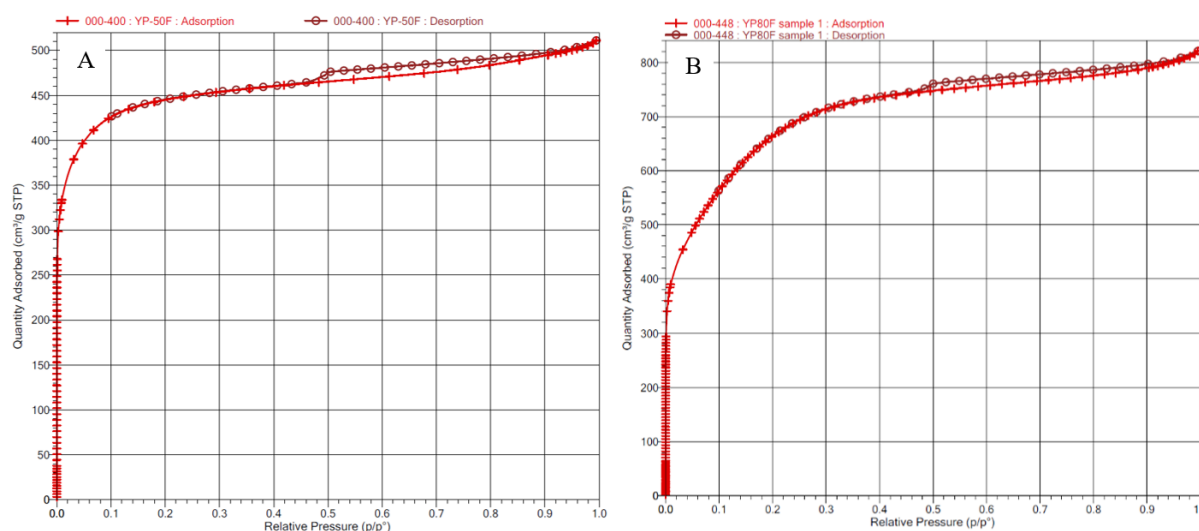


Figure 4.8: Isotherms of (A) AC-YP50F and (B) AC-YP80F

The two activated carbons used in this work YP50F and YP80F, had a surface area of $1680 \text{ m}^2 \cdot \text{g}^{-1}$ and $2285 \text{ m}^2 \cdot \text{g}^{-1}$, respectively. The obtained surface areas for the two activated carbons are in agreement with the values provided by the supplier (YP50F SA: $1500\text{-}1800 \text{ m}^2 \cdot \text{g}^{-1}$) and (YP80F SA: $2000\text{-}2500 \text{ m}^2 \cdot \text{g}^{-1}$). Table 4.8 and Table 4.9 show the specific surface area measured using the BET analysis for both the activated carbons and a number of electrodes. It is evident that YP50 has more micropore- than external- surface area, while YP80 has more external than micropore surface area. The BET surface area of JNT45 was also measured to determine whether a substrate contributes to the specific surface area of an electrode. The surface area of JNT45 was measured to be $7 \text{ m}^2 \cdot \text{g}^{-1}$, indicating that it does not contribute the surface area of the electrode. Table 4.8 shows CB does not contribute to SA of electrode and with an obtained value of $68 \text{ m}^2 \cdot \text{g}^{-1}$, it falls in line with the supplier.

Table 4.8: BET results for electrodes made through different deposition methods

Sample		Surface Area ($\text{m}^2 \cdot \text{g}^{-1}$)			
Name	Production method	Obtained	%	Micro-pore	External
CB (SSA: $50\text{-}80 \text{ m}^2 \cdot \text{g}^{-1}$)		68		69	0.00
YP50F (SA: $1500\text{-}1800 \text{ m}^2 \cdot \text{g}^{-1}$)		1680		1350	330
JNT45		7		0	7
E1-YP50-S1-JNT45	SIC	496 (876) ⁿ	52	413 (730) ⁿ	83 (146) ⁿ
E2-YP50-I2-JNT45	SC	465 (638) ⁿ	38	257 (353) ⁿ	207(285) ⁿ
E3-YP50-I3-JNT45	IID ^{RT}	571 (1332) ⁿ	79	468 (1092) ⁿ	103 (240) ⁿ
E4-YP50-I4-JNT45	IID ^{HT}	705 (1572) ⁿ	94	560 (1249) ⁿ	144 (323) ⁿ

^{a)} SIC=slurry infiltration by calendaring IID=infiltration ink dropwise, ^{RT} = $25 \pm 5 \text{ }^\circ\text{C}$, ^{HT} = $130 \pm 5 \text{ }^\circ\text{C}$, SC= spray-coated

ⁿ⁾ Normalised

The surface area of an electrode is significantly lower compared to the activated carbon used in that sample. It is for this reason that the surface area is normalised to account for the surface area of the active carbon.

Table 4.8 tabulates the BET results for electrodes having a composition of 83:7:10 (AC-YP50F:PVDF:CB) with JNT45 substrate. The activated carbon in the differently prepared electrodes appear to lose some of its original surface area. The surface areas of E1-E4 have been normalised to the weight fraction of its AC-YP50F content.

The normalised surface area of E1 was $876 \text{ m}^2 \cdot \text{g}^{-1}$ which is 52 % of its original surface area. E2 managed to only keep 38 % of its original surface area with a normalised surface area of $638 \text{ m}^2 \cdot \text{g}^{-1}$. E3 obtained a normalised surface area of $1332 \text{ m}^2 \cdot \text{g}^{-1}$, thus maintaining 79 % of its YP50F surface area. With a normalised surface area of $1572 \text{ m}^2 \cdot \text{g}^{-1}$, E4 retained 94 % of its YP50F surface area. The observed reduction in the specific surface area of the active material can be a result of the PVDF binder that is restricting access to some of the pores.

Figure 4.9 illustrates the BJH pore size distribution (PSD) for E1-E4. In 1951 Barret, Joyner and Halenda (BJH) developed the classical pore size model. This model is widely used for calculating pore size distributions over the mesoporous and part of the macropore range¹⁷².

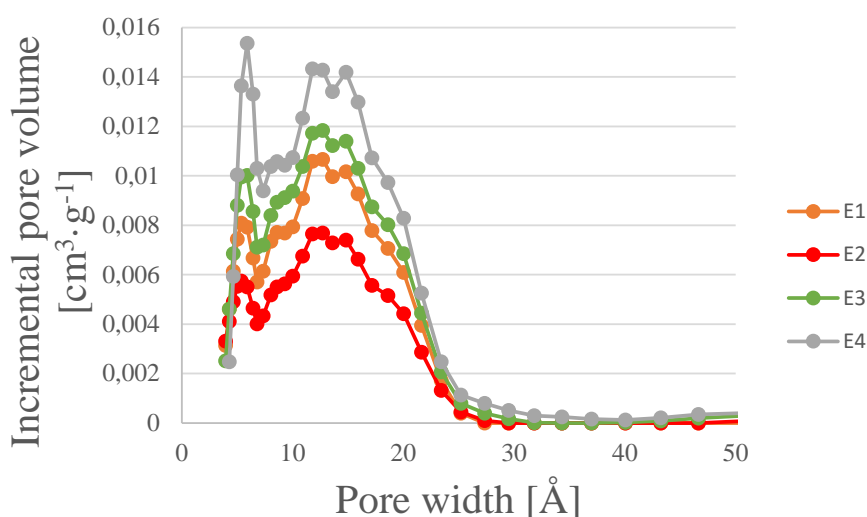


Figure 4.9: BJH pore size distribution for differently prepared electrodes

The PSD results presented in Figure 4.9 are in agreement with the BET surface areas for E1-E4 listed in Table 4.8. Since E1-E4 was made with YP50F, it is expected that it would favour smaller mesopores (2-20 Å). E4 has a sharp peak at 5.9 Å with an incremental pore volume of $0.015 \text{ cm}^3 \cdot \text{g}^{-1}$. The PSD for E1 appears to favour mesopores in the range of 10-23 Å with a

relatively small sharp peak at 5 Å. From Figure 4.9 it may be concluded that fabricating an electrode using the IID method at a high temperature is favourable for the pore size distribution.

BET results presented in Table 4.9 were measured at the Nelson Mandela University using a Micromeritics TriStar II 3020 Version 3.02.

Table 4.9: BET results for the different thermal treatment temperatures for E15 and E16

Sample			Surface Area (m ² ·g ⁻¹)			
Name	Deposition method	Thermal Treatment Temperature (°C)	Obtained	%	Micro-pore	External
JNT45		N/A	7			
CB (SSA: 50-80 m ² ·g ⁻¹)		N/A	68		69	0.00
YP80F (SA: 2000-2500 m ² ·g ⁻¹)			2285		373	1912
YP80F		130	2238		310	1928
YP80F		250	2242		358	1884
YP80F		350	2295		313	1982
E15-S15-YP80-JNT45-CB	IID ^{HT}	130	805(1976) ⁿ	86	106 (260) ⁿ	699 (1716) ⁿ
E15-S15-YP80-JNT45-CB	IID ^{HT}	250	813(1996) ⁿ	87	111 (272) ⁿ	702 (1724) ⁿ
E15-S15-YP80-JNT45-CB	IID ^{HT}	350	741(1821) ⁿ	80	102 (251) ⁿ	639 (1570) ⁿ
E16-S16-YP80-JNT45-CB	SIC	130	442(1610) ⁿ	70	31 (113) ⁿ	411 (1497) ⁿ
E16-S16-YP80-JNT45-CB	SIC	250	375(1362) ⁿ	60	26 (95) ⁿ	349 (1267) ⁿ
E16-S16-YP80-JNT45-CB	SIC	350	313(1139) ⁿ	50	23 (84) ⁿ	290 (1055) ⁿ

^{a)} SIC=slurry infiltration by calendaring IID=infiltration ink dropwise, ^{HT} = 130±5 °C

ⁿ⁾ Normalised

A sample of YP50F was also analysed, however the results obtained (1388 m²·g⁻¹) was not in line with the surface area provided by the supplier, due to the instrument not being suitable for microporous materials. The surface area results listed in Table 4.9 are for the thermal treatment of YP80F, E15 which was fabricated using the infiltration ink dropwise method at a high temperature and E16 which was made using the slurry infiltration by calendaring method. The ink for E15 and slurry for E16 were prepared by using an overhead stirrer for 60 minutes to complete the dry-mixing. E15 was wet-mixed using the ultrasonic bath and E16 was wet-mixed using the overhead stirrer for 60 minutes. As the thermal treatment temperature of YP80F increases from 130 °C to 250 °C and 350 °C, there is an increase of less than 1% increase in the surface area.

No real conclusion can be made about E15 (80:10:10 YP80F: PVDF:CB) which was made via the infiltration ink dropwise method at 130 ± 5 °C. This is because the surface area at 250 °C results in an electrode having the highest normalised surface area (1996 m²·g⁻¹), obtaining 87%

of its YP80F original surface area. Treatment at 350 °C retains 80 % of its original surface area with a normalised surface area of 1821 m²·g⁻¹ while E15 treated at 130 °C normalised surface area was 1976 m²·g⁻¹ which is 86 % of its original surface area.

The surface area of E16 (80:10:10 YP80F: PVDF:CB) which was made using the slurry infiltration by calendaring method of electrode production demonstrates a trend. As the temperature increases the surface area decreases. E15 treated at 130 °C has the highest normalised surface area with a value of 1610 m²·g⁻¹ and obtaining 70% of its original surface area. The percentage of surface area retained in terms of the activated carbon also decreased upon increasing the thermal treatment temperature.

All YP80F electrodes in Table 4.9 have a higher external surface area than the micropore surface area. For the thermal treatment of the electrodes, surface area seems to increase more when treated at the lower temperature of 130 °C with the exception of E15 which seems to favour thermal treatment at 250 °C. The reason why the surface area of an electrode seems to increase when thermally treated at lower temperatures is because of the PVDF binder. The melting point of the PVDF binder as well as the solid-state phase transitions of the PVDF changes when PVDF is crystalized at temperature higher than 155 °C¹⁷³. The PVDF can flow and block some of the pores when it melts which prohibits the N₂ from accessing these pores.

The wet mixing time of slurries were investigated to determine whether it has an impact on an electrodes characteristics. Table 4.10 shows that BET results for E18-E19 an E21 (80:10:10 YP80F:PVDF:CB) which were fabricated using the slurry infiltration by calendaring deposition method. The slurries for these electrodes were prepared using the devil shaker.

Table 4.10: BET results for electrodes having different ink mixing time

Sample		Surface Area (m ² ·g ⁻¹)			
Name	Mixing time (min)	Obtained	%	Micro-pore	External
CB (SSA: 50-80 m ² ·g ⁻¹)		68		69	0.00
YP80F (SA: 2000-2500 m ² ·g ⁻¹)		2285		373	1912
JNT 45		7		0	7
E18-YP80-S18-JNT45	120	493 (1497) ⁿ	66	39 (118) ⁿ	254 (1397) ⁿ
E19-YP80-S19-JNT45	60	584 (1610) ⁿ	70	51 (141) ⁿ	533 (1469) ⁿ
E21-YP80-S21-JNT45	30	567 (1716) ⁿ	75	48 (145) ⁿ	519 (1571) ⁿ

ⁿ = Normalized

E18 had a slurry with a wet mixing time of 120 minutes and is observed to have the lowest normalised surface area ($1497 \text{ m}^2 \cdot \text{g}^{-1}$). E19 has the second highest normalised surface area ($1610 \text{ m}^2 \cdot \text{g}^{-1}$) and its corresponding slurry was mixed for 60 minutes. E21 slurry had a mixing time of 30 minutes and was discovered to have the highest normalised surface area ($1716 \text{ m}^2 \cdot \text{g}^{-1}$). E18 obtained 66%, E19 achieved 70% and E21 75%.

Both E19 and E16 slurries were mixed for a total of 120 minutes (60 minutes dry-mix and 60 minutes wet-mix), however there is a difference in their obtained surface areas. E19 slurry was mixed using the devil shaker, while E16 was mixed using the overhead stirrer. From Table 4.10 it is evident that using the devil shaker for slurry mixing results in an electrode having a higher surface area compared to using an overhead stirrer. E19 managed to obtain 6% more of its original surface area compared to E16.

Table 4.11 summarises the N_2 adsorption results for the thermally treated electrodes at different temperatures. The surface area of the electrodes were normalised using the weight ratio of the activated carbon in order to make an impartial comparison. The normalised value of the surface area are identified in brackets. The electrodes that were fabricated had a composition of 80:10:10 (AC:PVDF:CB) utilising YP80F as the activated carbon on the JNT45 substrate.

Table 4.11: BET results for electrodes having different thermal treatment temperatures

Sample		Surface Area ($\text{m}^2 \cdot \text{g}^{-1}$)			
Name	Thermal treatment temperature ($^{\circ}\text{C}$)	Obtained	%	Micropore	External
JNT 45		7			
CB (SA: $50\text{-}80 \text{ m}^2 \cdot \text{g}^{-1}$)		68		69	0.00
YP80F (SA: $2000\text{-}2500 \text{ m}^2 \cdot \text{g}^{-1}$)		2285		373	1912
YP80F	130	2238		310	1928
YP80F	250	2242		358	1884
YP80F	350	2295		313	1982
E23	130	771 (1993) ⁿ	87	62 (160) ⁿ	709 (1833) ⁿ
E24	250	526 (1804) ⁿ	79	42 (144) ⁿ	484 (1660) ⁿ
E25	350	627 (1798) ⁿ	79	106 (304) ⁿ	521 (1494) ⁿ

ⁿ = Normalized

The activated carbon YP80F had a large BET surface area of $2238 \text{ m}^2 \cdot \text{g}^{-1}$, micropore and external surface area of 310 and $1928 \text{ m}^2 \cdot \text{g}^{-1}$ respectively. The surface area of all three electrodes produced were normalised to the weight fraction of YP80F. E23, which was thermally treated at $130 \text{ }^{\circ}\text{C}$ obtained a normalised surface area of $1993 \text{ m}^2 \cdot \text{g}^{-1}$ which is 87% of the original YP80F surface area. E24 retained 79% of YP80F's original surface area by having achieved a normalised surface area of $1804 \text{ m}^2 \cdot \text{g}^{-1}$. E25 obtained a normalised surface area of

1798 $\text{m}^2 \cdot \text{g}^{-1}$ which also corresponded to 79% of YP80F's original surface area. E25 was thermally treated at 350 °C while E24 was thermally treated at 250 °C but the variance in the normalised surface area of E25 and E24 are miniscule when compared to E23. This shows that when thermally treating at temperatures of 250 and 350 °C, much of the solvent would have already evaporated thus availing more surface area for ionic adsorption. The reason for E24 and E25 having a lower surface area than E23 could be ascribed to the melting of the PVDF binder as well as the solid-state phase transitions of the PVDF¹⁷³. The PVDF can flow and block some of the pores when it melts which prohibits the N_2 from accessing these pores.

Figure 4.10 illustrates the BJH pore distribution for E21 and E23.

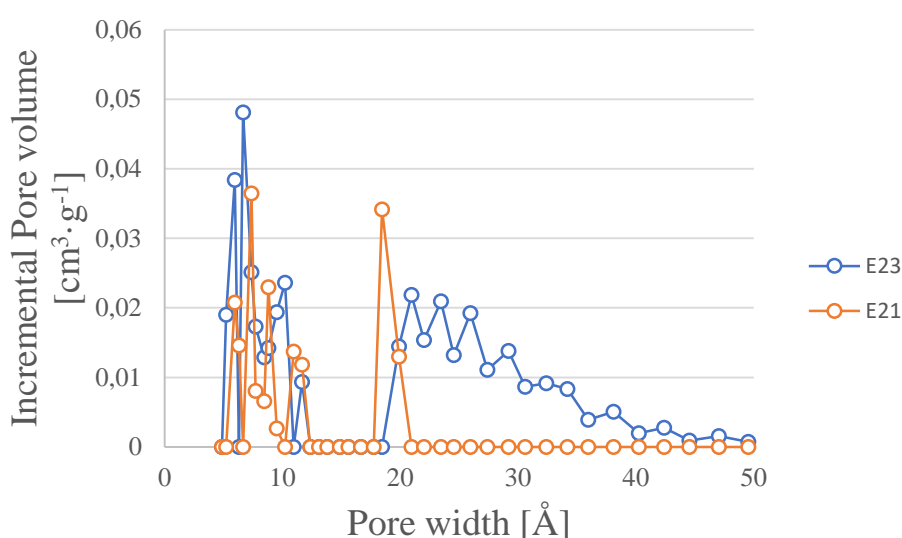


Figure 4.10: BJH pore size distribution for E21 and E23

From Figure 4.10 the presence of mesopores in both E21 and E23 is evident since the pore width varied between 5 and 50 Å. There appears to be no micropores in E21 and E23. This confirms the low micropore surface area listed in Table 4.10 and Table 4.11 for E21 and E23, respectively. E21 seems to favour smaller mesopores (5-13 Å) with a few larger mesopores at 20 Å. E23 has a more varied size range of mesopores (5-13 and 20-50 Å). Thermally treating an electrode results in not only the surface area being affected but also the pore size distribution. E21 had a normalised surface area of 1716 $\text{m}^2 \cdot \text{g}^{-1}$ while E23 achieved a normalised surface area of 1993 $\text{m}^2 \cdot \text{g}^{-1}$. From Figure 4.10 it is evident that thermally treating the electrode at 130 °C results in an increase in the pore volume, which is in agreement with the increase in BET surface area. E23 has a higher incremental pore volume compared to E21. For E21 the highest incremental pore volume is 0.04 $\text{cm}^3 \cdot \text{g}^{-1}$ at 7.36 Å. The highest incremental pore volume for

E23 is $0.05 \text{ cm}^3 \cdot \text{g}^{-1}$ at 6.65 \AA . According to Wang et al.¹¹⁸ mesopores increase electrosorption capacity.

4.2.4 Scanning electron microscopy

Figure 4.11 presents the SEM images of pure (A) activated carbon, (B) carbon black, (C) PVDF powders and (D) JNT45 substrate. From Figure 4.11 (A) it can be seen that AC-YP80F powder consisted of anisometric particles. Macroparticles, which have pores larger than 50 nm ¹⁶⁸, can be observed in the pure activated carbon sample.

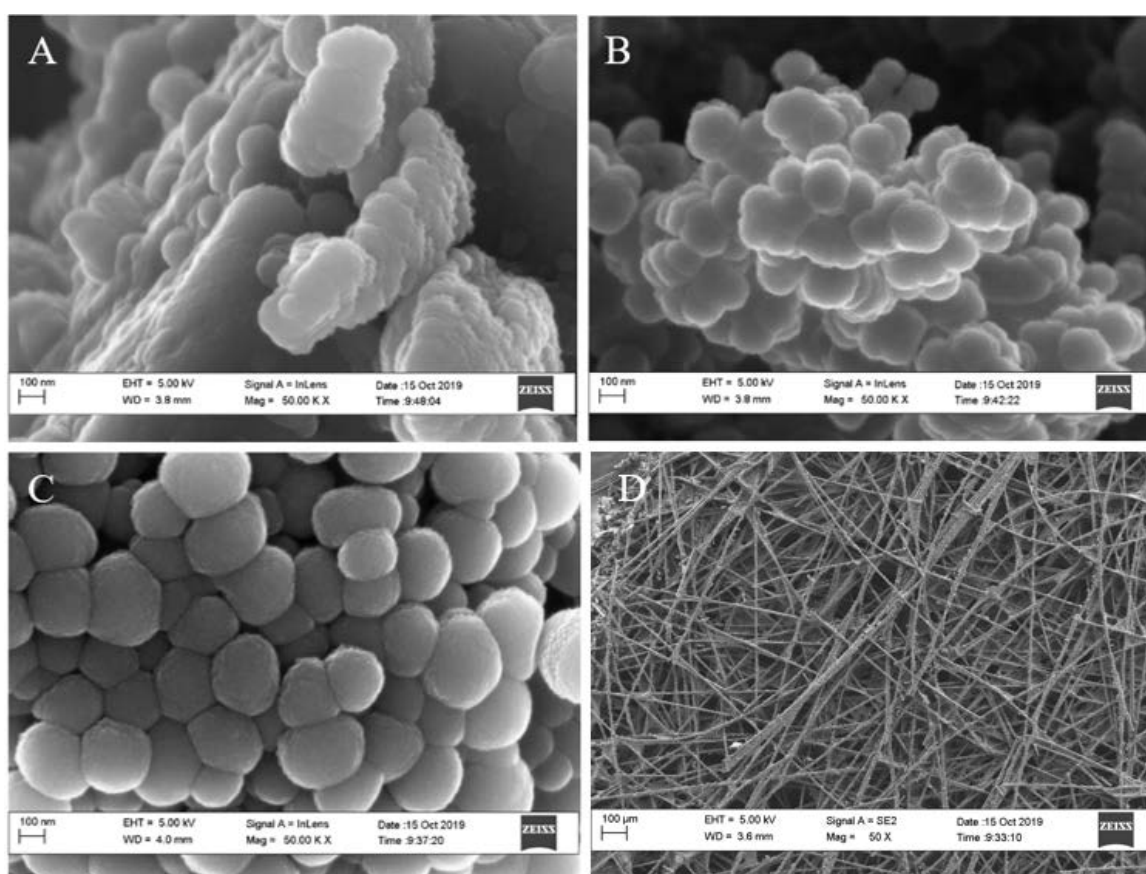


Figure 4.11: SEM images of pure (A) AC-YP80F, (B) CB, (C) PVDF powders and (D) JNT45 substrate

It can be noted in Figure 4.11 (B) that carbon black has an amorphous structure and its morphology portrays standard assembled spherical particles. Primary CB particles appear to be spherical, when they blended together they form aggregates and following the Van der Waals forces, aggregates connect forming agglomerates¹⁷⁴. Figure 4.11 (D) illustrates the porous JNT45 substrate. From (D) it can be seen that the sample has a high porosity due to the empty space between the elongated microfibrils. The width of 1 fibre was measured to be less than 10 μm . PVDF powder (Figure 4.11 (C)) consists of aggregates of small particles,

approximately 325 nm in size. A SEM image of activated carbon is shown in Figure 4.12 (A). The image illustrates the porous characteristics of activated carbon with the presence of some uneven cavities. A cavity is an open pore that communicates with the surface of a particle ¹⁷⁵. Figure 4.12 (B) clearly showcases the carbon black sitting inside the activated carbon cavities. Activated carbon is observed to be covered with spherical and non-spherical structures.

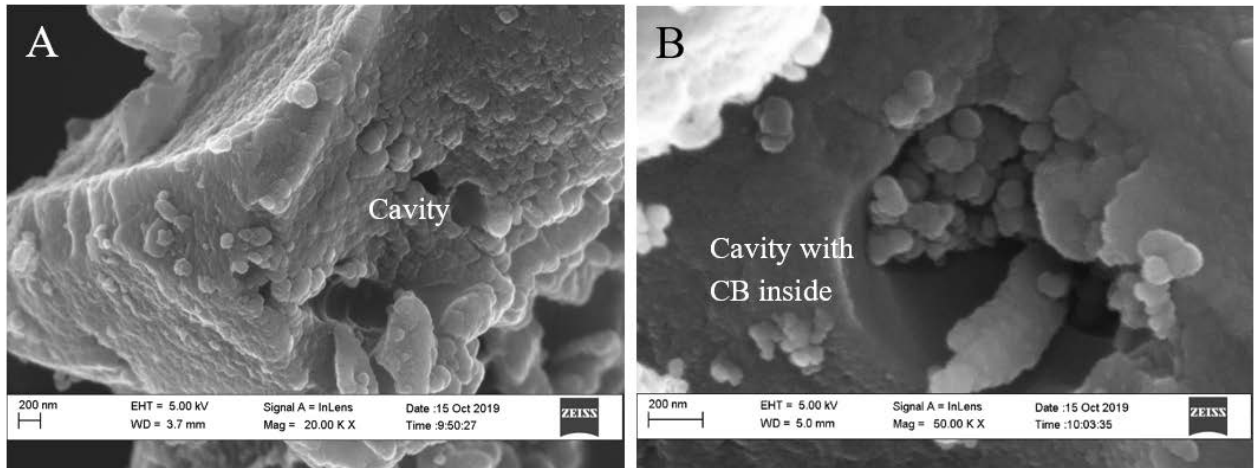


Figure 4.12: SEM images of (A) AC-YP80F with an empty cavity and (B) AC and CB 60 min dry mixture with CB sitting inside a cavity of AC

Figure 4.13 (A) depicts a SEM image of an electrode fabricated using the slurry infiltration by calendaring method and (B) presents a SEM image of an infiltration ink dropwise electrode. In (A) it is clear that the slurry penetrated into the substrate with some of the JNT45 fibres still visible. From (C) it can be noted that utilising the infiltration ink dropwise method of electrode production results in the ink covering the entire surface of the electrode with no fibres insight. From the SEM images there is no clear morphological difference between SIC and IID electrode.

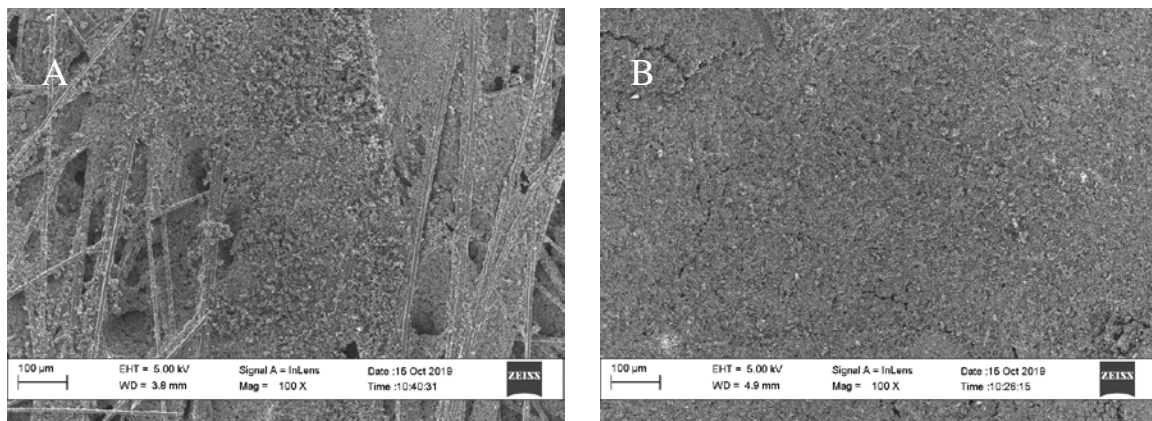


Figure 4.13: SEM images of (A) SIC electrode and (B) IID electrode

The SEM images of produced electrodes in Figure 4.14 show that the surface of the fabricated electrodes with irregular network-like aggregation of AC, carbon black and PVDF binder. Cavities can be also be seen in the SEM images. In Figure 4.14 (A) one can clearly see the carbon black agglomerates sitting just outside the entrance of the cavity while in (B) there appears to be a few cavities with no carbon black agglomerates. It should also be noted that the cavities in Figure 4.14 (B) seem to be smaller than those in (A).

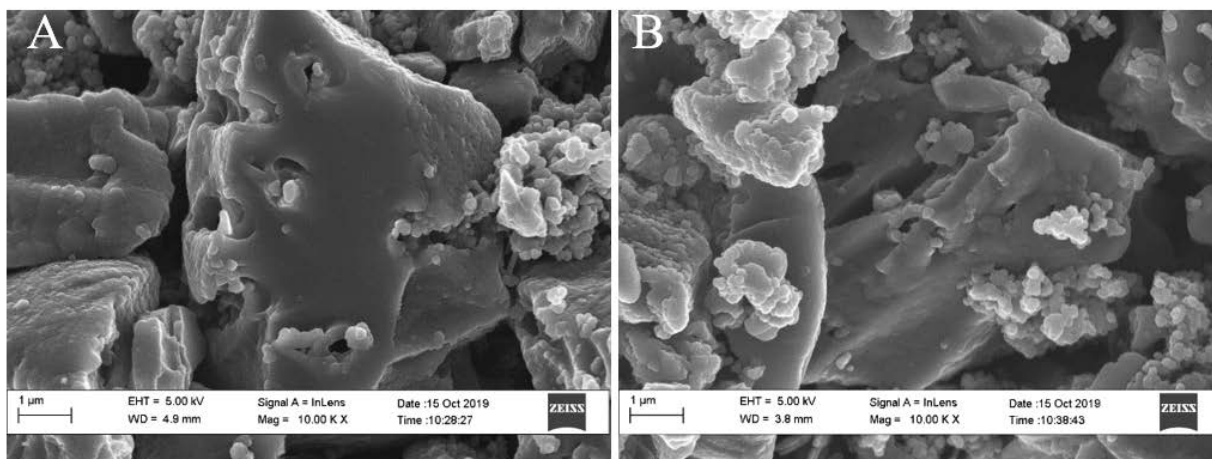


Figure 4.14: SEM images showing the cavities in (A) SIC and (B) IID electrodes

4.2.5 Electrode salt removal performance

In terms of salt adsorption- desorption performance; the maximum salt adsorption capacity and the Kim-Yoon diagram will be discussed separately.

4.2.5.1 Maximum salt adsorption capacity (mSAC)

Appendix E illustrates the CDI Data Analysis Excel sheet used to analyse the conductivity and current obtained from the Paraly and Nova softwares, respectively, in order to determine the mSAC values of the electrodes produced. All mSAC experiments were repeated three times and the average of the three is reported in this work. Figure 4.15 illustrates the conductivity and current vs time graph for E1. The first 7- adsorption and desorption cycles are the pre-conditioning cycles for the electrodes. The cycle that follows the pre-conditioning is used to determine the mSAC of the electrode.

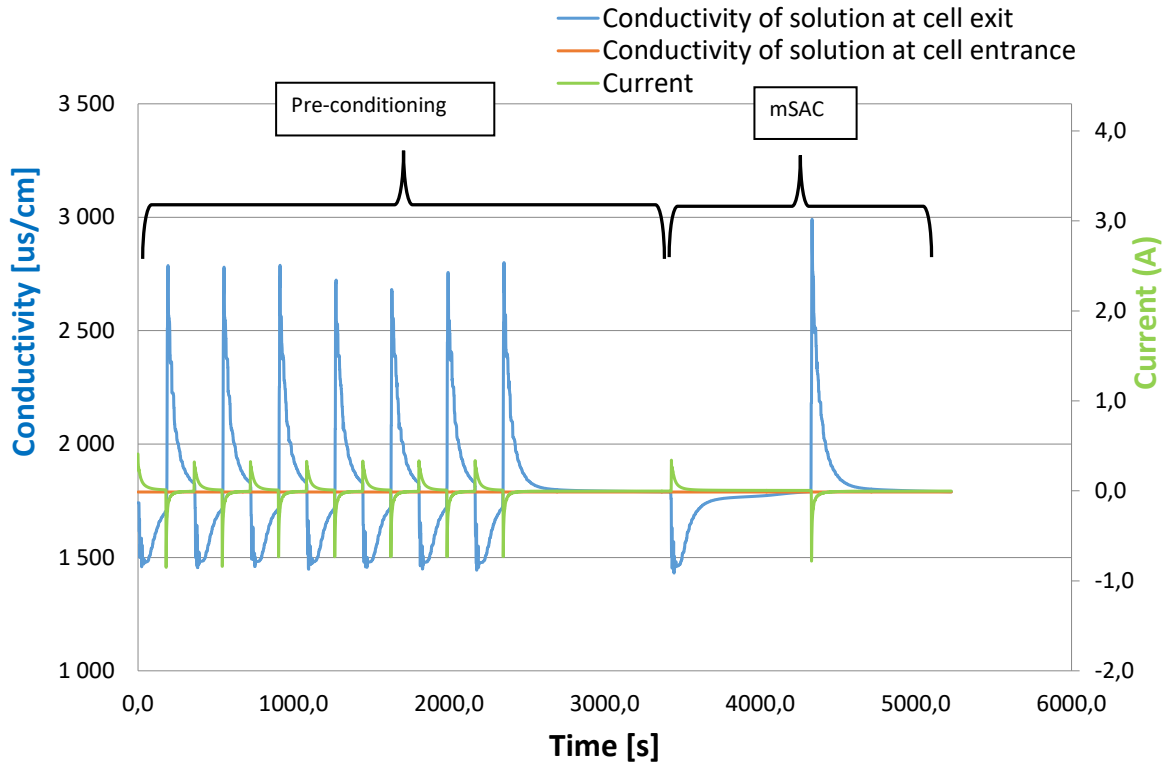


Figure 4.15: Conductivity and current graph vs time for E1

Table 4.12 compares the mSAC for electrodes having different deposition methods and different compositions.

Table 4.12: mSAC values of electrodes having different deposition methods

Electrode	CB (%)	PVDF (%)	Deposition method	mSAC ($\text{mg}\cdot\text{g}^{-1}$)
JNT45	N/A	N/A	N/A	0.423
E1-YP50-S1-JNT45	83	7	SIC	16.3
E2-YP50-I2-JNT45	83	7	SC	10.6
E3-YP50-I3-JNT45	83	7	IID ^{RT}	13.1
E4-YP50-I4-JNT45	83	7	IID ^{HT}	11.8
E13-YP50-I13-JNT45	80	10	SC	7.3
E14-YP50-S14-JNT45	80	10	SIC	13.6
E17-YP50-I17-JNT45	80	10	IID ^{HT}	12.5

E1-E4 had 7% PVDF binder. The mSAC of the JNT45 substrate is also listed in the table. JNT45 had a maximum salt adsorption capacity of $0.423 \text{ mg}\cdot\text{g}^{-1}$. This proves that the substrate does not contribute towards the desalination performance of the electrode and should not be included in the mSAC calculations. E1 which was produced by the slurry infiltration by calendaring method outperforms E2, E3 and E4 in-terms of mSAC despite the significant loss in the specific surface area. From literature it is reported that there is a direct relationship between the surface area of an electrode and its corresponding salt adsorption capacity,

meaning an electrode with a high BET surface area is expected to have a higher salt adsorption capacity^{118,130,176}. Although, there have been reports where electrodes would have a low BET surface area ($\sim 500 \text{ m}^2 \cdot \text{g}^{-1}$) while still having a better salt adsorption capacity ($0.21 \text{ mmol} \cdot \text{g}^{-1}$) compared to an electrode having a BET surface $\sim 1600 \text{ m}^2 \cdot \text{g}^{-1}$ with a corresponding SAC of $0.12 \text{ mmol} \cdot \text{g}^{-1}$ ¹²⁴. E4 was expected to show the highest mSAC because of its high BET surface area ($1572 \text{ m}^2 \cdot \text{g}^{-1}$). This anomaly can possibly be explained by the low conductivity of E4. Thus, assuming that a portion of the activated material was available in electrically isolated pockets within the electrode, it was accessible to N_2 gas but not to capacitance. Fabricating the electrode at a lower temperature is beneficial for the desalination capacity since the mSAC was for E3 was $1.9 \text{ mg} \cdot \text{g}^{-1}$ more than E4. E2 which was produced via the spray-coating method illustrated the lowest desalination performance with an mSAC of $10.6 \text{ mg} \cdot \text{g}^{-1}$, 35% less than E1.

Lu et al.¹⁵³ reported a spray-coating electrode with an electroadsorption capacity of $5.6 \text{ mg} \cdot \text{g}^{-1}$. Possible reason for this difference could be that Lu et al. made electrode with different parameters. The electrodes fabricated by Lu et al.¹⁵³ were made using a different binder, Polytetrafluoroethylene (PTFE) and had a composition of 85:15:5 (AC:PTFE:CB). Additionally, the PTFE suspension solution was made out to be 16 wt. % and the solvent used was ethanol. Of the three electrodes they produced, electrodes with the spray-coating presented the lowest desalination performance.

E13-E14 and E17 had a PVDF binder composition of 10 %. The electrode that was produced using the slurry infiltration by calendaring method exhibits the highest mSAC ($13.6 \text{ mg} \cdot \text{g}^{-1}$) compared to the electrode which was made using either the spray-coating (E13, $7.3 \text{ mg} \cdot \text{g}^{-1}$) or infiltration ink dropwise method. (E17, $12.5 \text{ mg} \cdot \text{g}^{-1}$). When comparing these electrodes to what was discussed from the findings in Table 4.12, it can be concluded that the addition of more binder is not favourable for increased desalination performance. Using the same deposition method there is a 17% decrease in the desalination performance when changing the composition from 83:7:10 to 80:10:10 (AC:PVDF:CB). According to Zornitta et al.¹⁷⁷ the thickness of an electrode has an influence on the electroadsorption process since it may affect the transport of diffusion in the interparticle pores and the electrochemical activity within the porous sample. The most significant increase in thickness occurs when the electrode is made by spray-coating the active ingredients onto the surface of the substrate. The reason for the increased thickness is that ink is coated on top of the substrate instead of penetrating inside. There is a 45% increase in the electrode thickness when changing the composition from 83:7:10

to 80:10:10. In turn, the mSAC value decreases by 31%. The increase in electrode thickness and decrease in mSAC can be attributed to more PVDF binder being present in the electrodes which block more pores.

Table 4.13 shows the mSAC values for electrodes produced utilising different deposition methods with an 83:7:10 (AC:PVDF:CB) composition on the SGDL substrate.

Table 4.13: mSAC values of Electrodes with different deposition methods on SGDL substrate

Electrode	Deposition method	mSAC (mg·g ⁻¹)
E5-S5-YP80-GDL38AA-CB	SIC	8.8
E6-I6-YP80-GDL38AA-CB	IID ^{HT}	8.6
E7-I7-YP80-GDL38AA-CB	IID ^{RT}	9.8

The values are significantly lower compared to what was discussed previously. This could be a result of a different substrate being used (SGDL) which does not allow for the storage of as much ions as the JNT45 substrate. The fibrous networks of the two substrates may differ, therefore differing the porosity, which permits for the accommodation of varying slurry amounts. Interestingly, for the SGDL substrate, the infiltration ink dropwise at room temperature achieves the highest desalination capacity with a value of 9.8 mg·g⁻¹ compared to when the electrode was made using the slurry infiltration by calendaring method (8.8 mg·g⁻¹).

The mSAC values for electrodes having different ink mixing times with an 80:10:10 (AC:PVDF:CB) composition, utilising YP80F as the activated carbon on the JNT45 substrate are illustrated in Figure 4.16. From the graph it is evident that the ink mixing time has an impact on the desalination performance of the electrode. Four different mixing times were investigated; 15, 30, 60 and 120 minutes, to determine whether it has an impact on the performance on the electrode. From those four, mixing the ink for 30 minutes resulted in an electrode with the highest desalination capacity showcasing an mSAC value of 16 mg·g⁻¹. Mixing for an additional 30 minutes caused the desalination capacity to lower to 12.1 mg·g⁻¹. Ink mixing for 120 minutes caused the desalination performance to further decrease to 11.2 mg·g⁻¹. Mixing the ink for longer periods of time results in the de-agglomeration of the active materials which break the agglomerates of CB formed on AC (see Figure 4.12). CB is known to improve the conductivity of the electrode and increased conductivity is beneficial for the fast transport of ions and the charge storage, which enhances the desalination performance¹⁶⁶. Thus, if the CB-AC particles start to de-agglomerate the CB breaks away from the AC, lowering the conductivity and as a consequence the desalination performance.

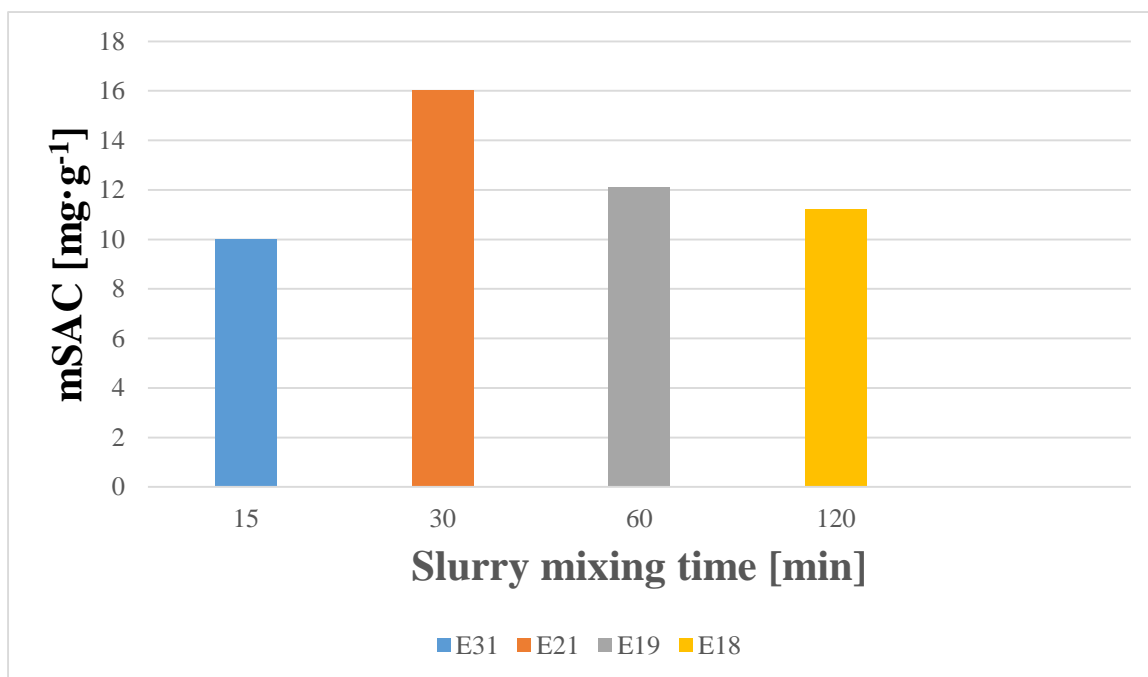


Figure 4.16: mSAC values of electrodes having different slurry mixing times

Figure 4.17 depicts the mSAC values for E23-E25 which have different thermal treatment temperatures.

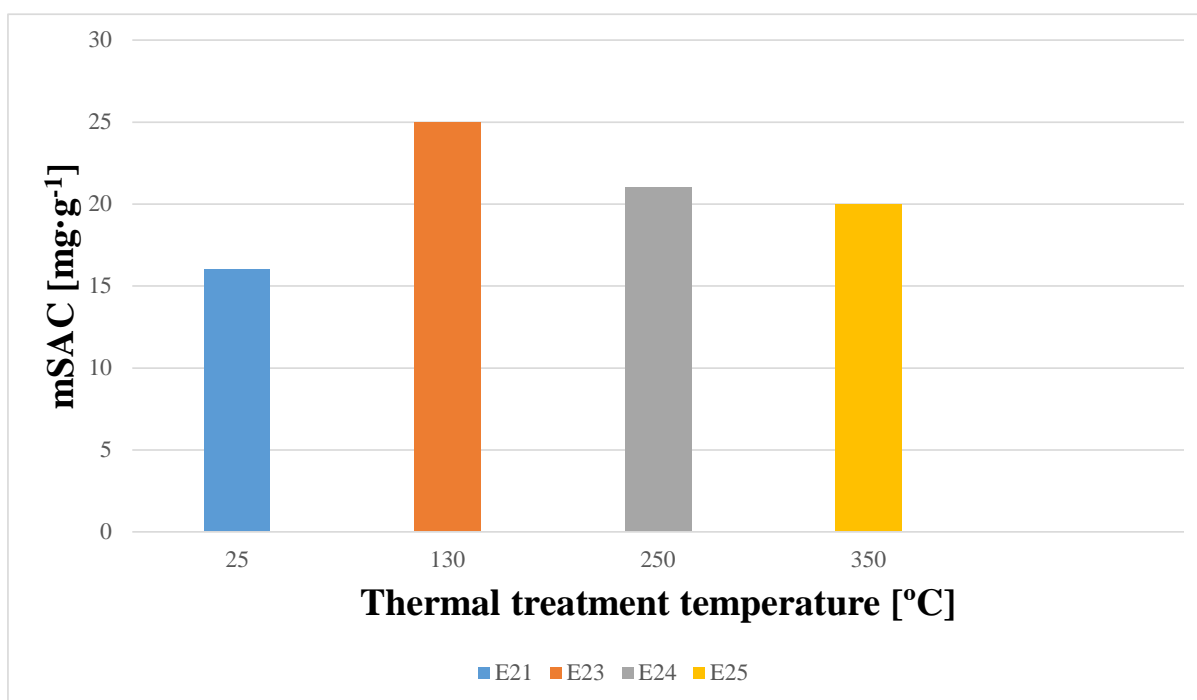


Figure 4.17: mSAC values of electrodes with different thermal treatment temperatures

E23 exhibits the highest desalination capacity with a calculated mSAC of $24.6 \text{ mg}\cdot\text{g}^{-1}$, followed by E24 and E25 with mSAC values of 20.9 mg and $20.1 \text{ mg}\cdot\text{g}^{-1}$, respectively. Thermally treating the electrodes to $130 \text{ }^\circ\text{C}$ results in a significant improvement in the desalination performance when comparing to electrodes that were not thermally treated. There is $0.8 \text{ mg}\cdot\text{g}^{-1}$ difference between the mSAC of E24 and E25. E23-E25 had the same composition, activated carbon, slurry mixing time and substrate as E21. It was also fabricated using the slurry infiltration by calendaring method, and can thus, compared fair comparison can be made. From Figure 4.16 it is known that E21 had a desalination capacity of $16 \text{ mg}\cdot\text{g}^{-1}$. When thermally treated at $130 \text{ }^\circ\text{C}$, the desalination capacity of an electrode made under the same conditions improved by 35% from $16 \text{ mg}\cdot\text{g}^{-1}$ to $24.6 \text{ mg}\cdot\text{g}^{-1}$. At this temperature of $130 \text{ }^\circ\text{C}$ much of the DMAC solvent that was used in the electrode production would have evaporated, thus opening up more of the pores for ionic adsorption in the electrode. This is verified in the TGA analysis shown in Figure 4.6. As the thermal treatment temperature is increased to 250 and $350 \text{ }^\circ\text{C}$ from $130 \text{ }^\circ\text{C}$, there is an improvement in the mSAC by 23% and 20%, respectively. In Figure 4.18 the adsorption-desorption curves for E21, and E23-E25 were superimposed.

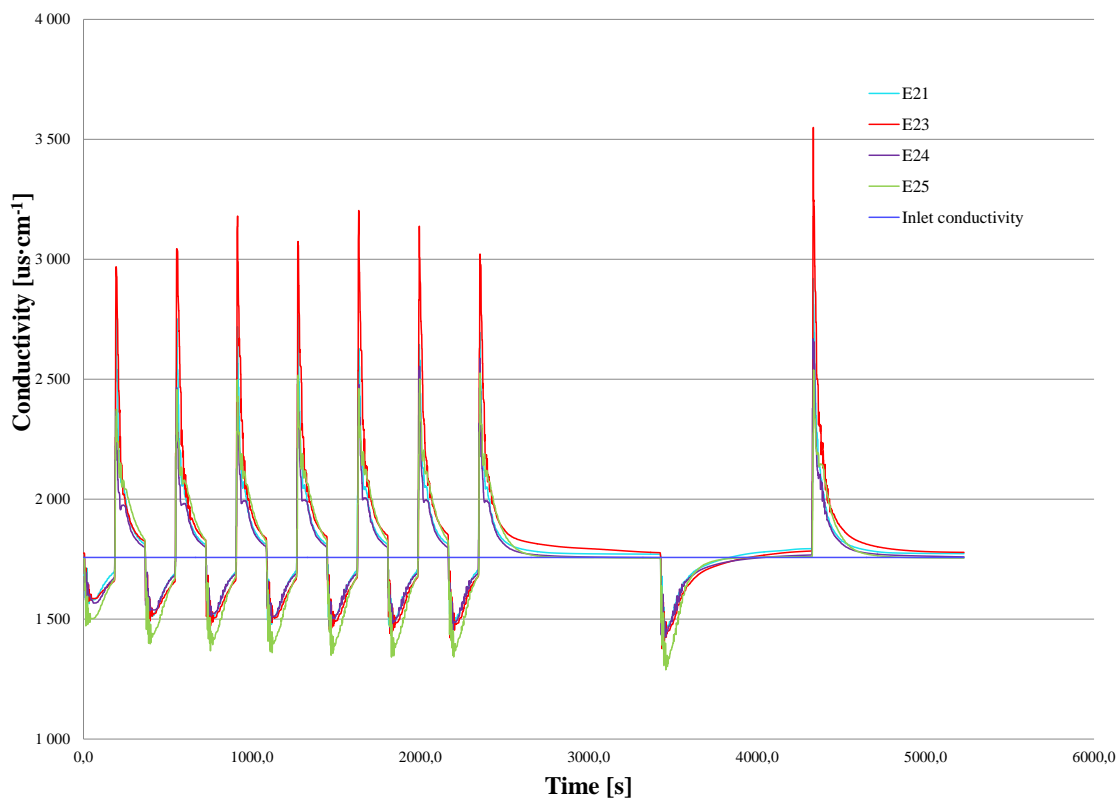


Figure 4.18: Conductivity vs time graph for electrodes having different thermal treatment temperatures

4.2.5.2 Kim-Yoon for salt adsorption rate versus capacity

Figure 4.19 shows the Kim-Yoon plot for E21 in the MCDI cell illustrated in section 3.2.5.1. In order to obtain the results in the figure below, adsorption-desorption measurements were executed using different half cycle times (HTC) of 1, 1.5, 2, 3 and 5 minutes with a feed flow rate of $13 \text{ mL} \cdot \text{min}^{-1}$ was used. The small black squares represent the corresponding ASAR and SAC values of each HTC. The black line on the Kim-Yoon plot shows the expected pattern of the ASAR vs SAC values at 1.2 V. the maximum ASAR value achieved was $2.74 \text{ mg} \cdot \text{g}^{-1} \cdot \text{min}^{-1}$ at 1 minute HTC with a SAC of $5.5 \text{ mg} \cdot \text{g}^{-1}$. $10.8 \text{ mg} \cdot \text{g}^{-1}$ was the highest SAC achieved with an ASAR value of $1.08 \text{ mg} \cdot \text{g}^{-1} \cdot \text{min}^{-1}$. For 1.2 V, the optimum HTC was observed to be 2 minutes, having ASAR and SAC values of $2.11 \text{ mg} \cdot \text{g}^{-1} \cdot \text{min}^{-1}$ and $6.3 \text{ mg} \cdot \text{g}^{-1}$. Before it was reported that E21 had an mSAC of $16 \text{ mg} \cdot \text{g}^{-1}$. From the Kim-Yoon results below it appears as though the adsorption capacity has decreased. At this point in time, it is unclear why the capacity of the electrode decreased.

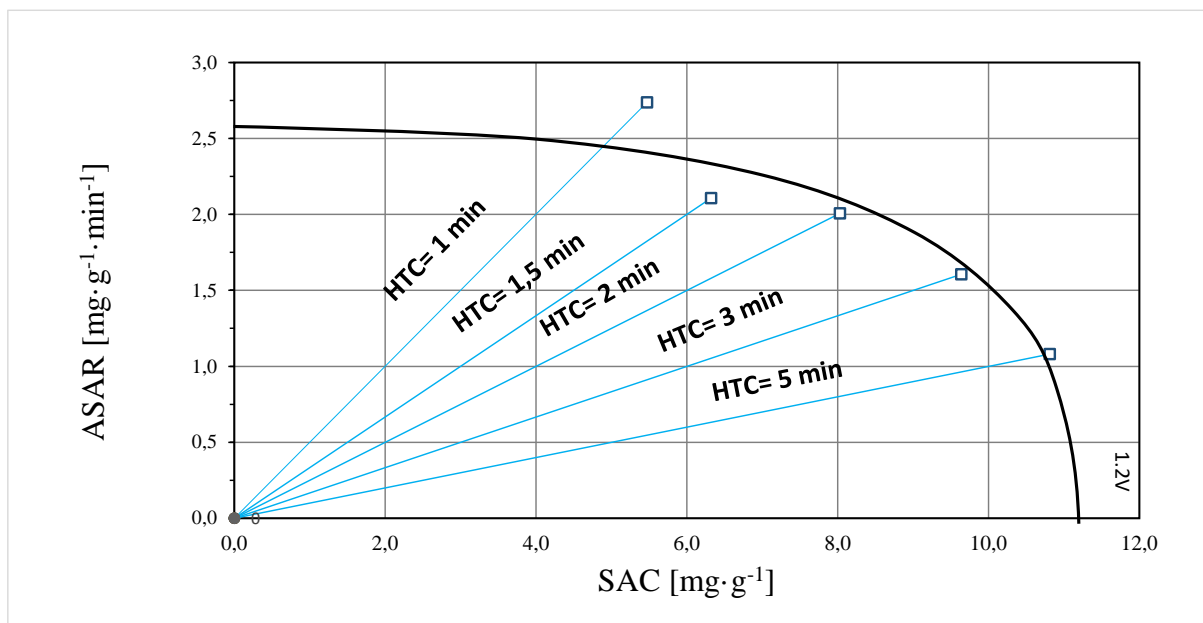


Figure 4.19: Kim-Yoon plot for E21

5 Conclusion and Future Work

This chapter concludes all the work that was done for this thesis study and future work that may be done.

5.1 Conclusion

Different fabrication methods were employed to make electrodes, namely, slurry infiltration by calendaring (SIC), infiltration ink dropwise (IID) and spray-coating (SC). Various techniques were used in order to characterise the electrodes that were fabricated, electrode conductivity using the four-point-probe method, and contact angle to determine the hydrophilic/hydrophobic nature of the electrodes, N₂ adsorption to determine the specific surface area of the carbonaceous materials and electrodes, and scanning electron microscopy to investigate the morphology of activated carbon, carbon black, PVDF and the prepared samples. The objective of the study was to optimise the ink/slurry composition, optimise the CDI electrodes manufacturing technique, analyse the electrode properties and link these properties to the synthesis variables

It was established that the different deposition methods require different amounts of solvent. Making use of a calendaring machine to deposit the active materials into the substrate, a slurry was made, which required a relative small amount of solvent. In the case of spray-coating or infiltration ink dropwise, an ink was prepared requiring 10 times higher solvent content to improve the flow properties.. Two different stirring mechanisms were investigated, an overhead stirrer with controllable speed and the devil shaker, where the only controllable parameter was the mixing time. The transition from the overhead stirrer to the devil shaker was made due to the fact that when mixing using the overhead stirrer not all of the ingredients would partake in the mixing and would often need to be hand agitated first before continuing with the overhead stirrer. A holder was designed in-house at SAIAMC to hold the syringe during the mixing of the ink/slurry.

For the SIC method of electrode production, the only controllable parameter when making the electrode was the thickness which was adjusted by changing the gap spacing between the rollers, which was kept constant in this work (0.03 cm). Two different temperatures were investigated when electrodes were fabricated utilising the IID method, 25 ± 10 °C and 130 ± 10 °C. When making electrodes using the SC method, all inks first were ultra-sonicated for 30 minutes.

- Findings related to optimisation of electrical conductivity

The four-point probe method was adopted in order to determine the electrode conductivity. The apparatus used for these measurements were designed and fabricated in-house at SAIAMC. Electrodes prepared using the SIC method exhibited the highest electrical conductivity. Electrodes prepared at low temperatures resulted in having the lowest conductivity. The SGDL substrate results in the electrodes having the highest conductivity overall. Mixing time has an impact on the conductivity. Mixing the ink for 30 minutes results in an electrode having the highest conductivity compared to when the ink is mixed for either 60 or 120 minutes.

- Findings related to optimisation of the wettability

The results obtained from the contact angle measurements, reveal that the electrode production method has an impact on the hydrophilic nature of the resulting electrode. Generally speaking the electrodes produced using the infiltration ink dropwise method at high temperature showed the lowest contact angle. It was established that producing electrodes at higher temperatures is favourable for the hydrophilic nature of the electrode. Treating the electrode at 350 °C yielded perfect wetting since the contact angle of the electrode was 0°. The composition and substrate also influences the hydrophilic nature of the electrode. A decrease in PVDF- to -carbon ratio tends to increase the hydrophilic nature of the electrode. An electrode composition with a minimum of 10% PVDF is, however, advisable to render a mechanically stable electrode. Electrodes become 100% wettable when exposed to temperatures of 350 °C. Utilising the SGDL substrate results in higher contact angle measurements. The mixing time of the ink, results in the electrodes having varied wetting capabilities. Prolonged mixing of the electrode slurry results in a reduction of the hydrophilicity, and mixing time under 60 minutes would therefore be preferred.

Findings related to optimisation of the normalised specific surface areas

- Findings related to optimisation of the surface area

N₂ adsorption analysis provided information on the surface area of the electrodes, which were all normalised to the weight fraction of the corresponding activated carbon that was used. It was found that using the IID method of electrode production at high temperature resulted in an electrode retaining 92% of its original surface area. SC resulted in the

electrode having the lowest surface area, only retaining 38% of its original surface area value.

- Findings related to electrode morphology

SEM images of the pure powders used in this thesis work gave more insight into the structure, pore size, particle size and the presence of aggregates. SEM micrographs of the 60 min dry mixture of activated carbon and carbon black showcased the carbon black agglomerates sitting inside the cavities present in the activated carbon. SEM images of slurry infiltration by calendaring and infiltration ink dropwise fabricated electrodes presented the irregular network –like aggregation of activated carbon, carbon black and PVDF binder.

- Findings related to electrode salt adsorption / desorption capacity

The maximum salt adsorption (mSAC) capacity was considered as the most important performance parameter for the produced electrodes. It can be concluded that using the SIC method of electrode production generally resulted in higher desalination capacity compared to when the electrode is made using IID or SC. An ink mixing time of 30 minutes has shown to be optimal. The effect of thermal treatment was investigated. An optimal mSAC was achieved with electrodes treated at 130 °C. By comparing the electrode substrate, JNT45 was mechanically more stable and appeared more suitable than the SGDL substrate.

The Kim-Yoon plot for E21 was presented. This was done to determine the optimal average salt adsorption rate (ASAR) and salt adsorption capacity (SAC). Five different half cycle times (HTC) of 1, 1.5, 2, 3 and 5 minutes with a feed flow rate of 13 mL·min⁻¹ was used. The maximum ASAR value achieved was 2.74 mg·g⁻¹·min⁻¹ at 1 minute HTC with a SAC of 5.5 mg·g⁻¹. 10.8 mg·g⁻¹ was the highest SAC achieved with an ASAR value of 1.08 mg·g⁻¹·min⁻¹. For 1.2 V, the optimum HTC was observed to be 2 minutes, having ASAR and SAC values of 2.11 mg·g⁻¹·min⁻¹ and 6.3 mg·g⁻¹.

- Summary of conclusions

The objectives of this study was achieved through the optimisation of a range of electrode fabrication processes and procedures. The highest recorded mSAC in this research work

was $24.6 \text{ mg}\cdot\text{g}^{-1}$, in line with the best purely capacitive electrodes in published literature.

This optimised electrode was synthesised by selecting:

- The slurry infiltration by calendaring produce rather than IID or ink spray technology
- The JNT45 substrate over SGDL
- YP80 over YP50 as active carbon material
- An ink mixing time of 30 minutes rather than 60 or 120 minutes
- A thermal treatment at $130 \text{ }^\circ\text{C}$

5.2 Future Works

Based on the analysis and conclusion of this research study, a number of suggestions regarding the future research direction are listed below:

- Investigate the use of MnO_2 as an anode to overcome the oxidation of carbon anodes.
- Study the long term operation of MCDI.
- Deposition of active materials directly onto a graphite current collector.
- Examine the operational parameters that would affect the Kim-Yoon diagram such as applying different potentials.
- Perform contact angle, electrode conductivity and surface area analysis on electrodes after the desalination experiment.
- Investigate constant current mode of operation.
- Thermal treatment of electrodes in different atmospheres.
- Electrochemical Impedance Spectroscopy (EIS) to determine the resistance of the MCDI cell.

6 Bibliography

1. Kaushal, S. S., Gold, A. J. & Mayer, P. M. Land use, climate, and water resources-global stages of interaction. *Water (Switzerland)* **9**, 815 (2017).
2. Mekonnen, M. M. & Hoekstra, A. Y. Sustainability: Four billion people facing severe water scarcity. *Science Advances* **2**, 1–7 (2016).
3. Guarino, A. S. The Economic Implications of Global Water Scarcity. *Research In Economics And Management* **2**, 51 (2017).
4. Liu, J., Hertel, T. W., Taheripour, F., Zhu, T. & Ringler, C. Water Scarcity and International Agricultural Trade. (2013).
5. World Water Assessment Programme (United Nations), and U.-W. *Water in a changing world. Earthscan* vol. 1 (2009).
6. Naik, P. K. Water crisis in Africa: myth or reality? *International Journal Of Water Resources Development* **33**, 326–339 (2017).
7. Anderson, M. A., Cudero, A. L. & Palma, J. Electrochimica Acta Capacitive deionization as an electrochemical means of saving energy and delivering clean water . Comparison to present desalination practices : Will it compete ? *Electrochimica Acta* **55**, 3845–3856 (2010).
8. Hanjra, M. A. & Qureshi, M. E. Global water crisis and future food security in an era of climate change. *Food Policy* **35**, 365–377 (2010).
9. Birdsall, N. & Sachs, J. *SUMMARY DEVELOPMENT REPORT 2003 Millennium Development*. (2003).
10. Mara, D., Lane, J., Scott, B. & Trouba, D. Sanitation and health. *PLoS Medicine* **7**, (2010).
11. Dieter, C. A., Maupin, M. A., Caldwell, R. R., Harris, M. A., Ivahnenko, T. I., Lovelace, J. K., Barber, N.L., & Linsey, K. . *Water Availability and Use Science Program: Estimated Use of Water in the United States In 2015. Geological Survey*

- Circular* (2018).
12. Eniscuola energy & environment. Water uses.
<http://www.eniscuola.net/en/argomento/water-knowledge/uses/water-consumption/>
(2014). (Accessed: 31st October 2019)
 13. Jhariya, D. C., Khan, R. & Thakur, G. S. Impact of Mining Activity on Water Resource : An Overview study Impact of Mining Activity on Water Resource : An Overview study. (2016).
 14. Prosser, I., Wolf, L. & Littleboy, A. Water in mining and industry. *Water: Science And Solutions For Australia* 135–146 (2011).
 15. Green, P. A., Vörösmarty, C. J., Harrison, I., Farrell, T., Sáenz, L. & Fekete, B. M. Freshwater ecosystem services supporting humans: Pivoting from water crisis to water solutions. *Global Environmental Change* **34**, 108–118 (2015).
 16. Schoeman, J. J. & Steyn, A. Investigation into alternative water treatment technologies for the treatment of underground mine water discharged by Grootvlei Proprietary Mines Ltd into the Blesbokspruit in South Africa. *Desalination* **133**, 13–30 (2001).
 17. Luo, A. K., Hou, Y. & Hu, X. Y. Mining influence on underground water resources in arid and semiarid regions. *IOP Conference Series: Earth and Environmental Science* vol. 113 012131 (IOP Publishing, 2018).
 18. Rekacewicz, P. Freshwater resources: volume by continent - Vital Water Graphics.
<http://www.unep.org/dewa/vitalwater/article32.html> (2006). (Accessed: 12th December 2018)
 19. Davies, B. Glaciers and climate change - Antarctic Glaciers.
<http://www.antarcticglaciers.org/glaciers-and-climate/glacier-recession/glaciers-and-climate-change/> (2017). (Accessed: 12th December 2018)
 20. Reeder, E. The Effect Global Warming Has on Icebergs | Sciencing.
<https://sciencing.com/effect-global-warming-icebergs-22880.html> (2017). (Accessed: 12th December 2018)
 21. Buytaert, W. Glacier melt and water security | Grantham Institute – Climate Change and the Environment | Imperial College London.

- <https://www.imperial.ac.uk/grantham/our-work/impacts-and-adaptation/ipcc-working-group-ii/water-security-and-flood-risk/glacier-melt-and-water-security/>. (Accessed: 12th December 2018)
22. Kundzewicz, Z. W., Krysanova, V., Benestad, R. E., Hov, Ø., Piniewski, M. & Otto, I. M. Uncertainty in climate change impacts on water resources. *Environmental Science And Policy* **79**, 1–8 (2018).
 23. Wang, X., Zhang, J., Shahid, S., Guan, E., Wu, Y., Gao, J. & He, R. Adaptation to climate change impacts on water demand. *Mitigation And Adaptation Strategies For Global Change* **21**, 81–99 (2016).
 24. Shahid, S. & Hazarika, M. K. Groundwater drought in the northwestern districts of Bangladesh. *Water Resources Management* **24**, 1989–2006 (2010).
 25. Nicholson, S. & Chong, D. Jumping on the human rights bandwagon: How rights-based linkages can refocus climate politics. *Global Environmental Politics* **11**, 121–136 (2011).
 26. Wang, X. jun, Zhang, J. yun, Yang, Z. feng, Shahid, S., He, R. min, Xia, X. hui & Liu, H. wei. Historic water consumptions and future management strategies for Haihe River basin of Northern China. *Mitigation And Adaptation Strategies For Global Change* **20**, 371–387 (2013).
 27. Kundzewicz, Z. W., Mata, L. J., Arnell, N. W., Döll, P., Jimenez, B., Oki, T., Şen, Z. & Shiklomanov, I. The implications of projected climate change for freshwater resources and their management resources and their management. *Hydrological Sciences Journal* **53**, 3–10 (2008).
 28. Parry, M., Evans, a, Rosegrant, M. W. & Wheeler, T. R. *Climate Change and Hunger Responding to the Challenge*. Reading vol. 78 (World Food Programme, 2009).
 29. Zhuang, X. W., Li, Y. P., Nie, S., Fan, Y. R. & Huang, G. H. Analyzing climate change impacts on water resources under uncertainty using an integrated simulation-optimization approach. *Journal Of Hydrology* **556**, 523–538 (2018).
 30. Maxmen, A. Cape Town scientists prepare for ‘Day Zero’: As water crisis brews, researchers plan to modify studies and prioritize public health. *Nature* vol. 554 13–14

- (2018).
31. The Lancet Planetary Health. Water crisis in Cape Town: a failure in governance. *The Lancet Planetary Health* vol. 2 e95 (2018).
 32. Yasin, A. S., Mohamed, I. M. A., Park, C. H. & Kim, C. S. Design of novel electrode for capacitive deionization using electrospun composite titania/zirconia nanofibers doped-activated carbon. *Materials Letters* **213**, 62–66 (2018).
 33. The Department of Water and Environmental Regulation. Understanding salinity. <http://www.water.wa.gov.au/water-topics/water-quality/managing-water-quality/understanding-salinity> (2017). (Accessed: 19th February 2020)
 34. Australian Water Association. *What is desalination?* http://www.nwc.gov.au/__data/assets/pdf_file/0015/36411/Urban-Performance-Report-2012-13.pdf (2018). (Accessed: 16th March 2018)
 35. Zarzo, D. & Prats, D. Desalination and energy consumption. What can we expect in the near future? *Desalination* **427**, 1–9 (2018).
 36. National Ground Water Association. *What is brackish water?* http://www.ngwa.org/media-center/briefs/documents/brackish_water_info_brief_2010.pdf (2010). (Accessed: 16th March 2018)
 37. Alencherry, T., A.R., N., Ghosh, S., Daniel, J. & Venkataraghavan, R. Effect of increasing electrical conductivity and hydrophilicity on the electrosorption capacity of activated carbon electrodes for capacitive deionization. *Desalination* **415**, 14–19 (2017).
 38. Mubita, T. M., Porada, S., Biesheuvel, P. M., van der Wal, A. & Dykstra, J. E. Capacitive deionization with wire-shaped electrodes. *Electrochimica Acta* **270**, 165–173 (2018).
 39. Qi, Z. & Koenig, G. M. Review Article: Flow battery systems with solid electroactive materials. *Journal Of Vacuum Science & Technology B, Nanotechnology And Microelectronics: Materials, Processing, Measurement, And Phenomena* **35**, 040801 (2017).

40. Lee, B., Park, N., Kang, K. S., Ryu, H. J. & Hong, S. H. Enhanced Capacitive Deionization by Dispersion of CNTs in Activated Carbon Electrode. *ACS Sustainable Chemistry & Engineering* **6**, 1572–1579 (2018).
41. Suss, M. E., Porada, S., Sun, X., Biesheuvel, P. M., Yoon, J. & Presser, V. Water desalination via capacitive deionization: what is it and what can we expect from it? *Energy Environ. Sci* **8**, 2296 (2015).
42. Roelofs, S. H., Kim, B., Eijkel, J., Han, J., Van Den Berg, A. & Odijk, M. Capacitive deionization on-chip as a method for microfluidic sample preparation. *Lab On A Chip* **15**, 1458–1464 (2015).
43. Seo, S. J., Jeon, H., Lee, J. K., Kim, G. Y., Park, D., Nojima, H., Lee, J. & Moon, S. H. Investigation on removal of hardness ions by capacitive deionization (CDI) for water softening applications. *Water Research* **44**, 2267–2275 (2010).
44. Porada, S., Feng, G., Suss, M. E. & Presser, V. Capacitive deionization in organic solutions: Case study using propylene carbonate. *RSC Advances* **6**, 5865–5870 (2016).
45. Remillard, E. M., Shocron, A. N., Rahill, J., Suss, M. E. & Vecitis, C. D. A direct comparison of flow-by and flow-through capacitive deionization. *Desalination* **444**, 169–177 (2018).
46. Suss, M. E. Size-Based Ion Selectivity of Micropore Electric Double Layers in Capacitive Deionization Electrodes. **164**, 270–275 (2017).
47. Dashtpour, R. & Al-zubaidy, S. N. Energy Efficient Reverse Osmosis Desalination Process. *International Journal Of Environmental Science And Development* **3**, (2012).
48. Abdel-Aal, E. A., Farid, M. E., Hassan, F. S. M. & Mohamed, A. E. Desalination of Red Sea water using both electrodialysis and reverse osmosis as complementary methods. *Egyptian Journal Of Petroleum* **24**, 71–75 (2015).
49. Veerapaneni, S., Long, B., Freeman, S. & Bond, R. Reducing energy consumption for seawater desalination. *Journal-American Water Works Association* **99**, 95–106 (2007).
50. Víctor-Ortega, M. D., Ochando-Pulido, J. M., Hodaifa, G. & Martínez-Ferez, A. Ion exchange as an efficient pretreatment system for reduction of membrane fouling in the purification of model OMW. *Desalination* **343**, 198–207 (2014).

51. Parise, T. Water Desalination. <http://large.stanford.edu/courses/2011/ph240/parise2/> (2012). (Accessed: 27th April 2018)
52. Imbrogno, J. & Belfort, G. Membrane Desalination: Where Are We, and What Can We Learn from Fundamentals? *Annual Review Of Chemical And Biomolecular Engineering* **7**, 29–64 (2016).
53. Zhao, D., Xue, J., Li, S., Sun, H. & Zhang, Q. dong. Theoretical analyses of thermal and economical aspects of multi-effect distillation desalination dealing with high-salinity wastewater. *Desalination* **273**, 292–298 (2011).
54. Van der Bruggen, B. & Vandecasteele, C. Distillation vs. membrane filtration: Overview of process evolutions in seawater desalination. *Desalination* **143**, 207–218 (2002).
55. Mistry, K. H., Antar, M. A., John, H. & Lienhard, V. An improved model for multiple effect distillation. *Desalination And Water Treatment* **51**, 807–821 (2014).
56. Ophir, A. & Lokiec, F. Advanced MED process for most economical sea water desalination. *Desalination* **182**, 187–198 (2005).
57. Al-Wazzan, Y. & Al-Modaf, F. Seawater desalination in Kuwait using multistage flash evaporation technology - Historical overview. *Desalination* **134**, 257–267 (2001).
58. The Healthy House. Reverse Osmosis Provides Pure Water on Tap - The Healthy House. <https://www.healthy-house.co.uk/water/drinking-water-filters/reverse-osmosis-water-filters>. (Accessed: 8th October 2018)
59. Fane, A. G. (Tony). A grand challenge for membrane desalination: More water, less carbon. *Desalination* **426**, 155–163 (2018).
60. Epsztein, R., Shaulsky, E., Dizge, N., Warsinger, D. M. & Elimelech, M. Role of Ionic Charge Density in Donnan Exclusion of Monovalent Anions by Nanofiltration. *Environmental Science And Technology* **52**, 4108–4116 (2018).
61. Chen, L. L., Moon, J. H., Ma, X., Zhang, L., Chen, Q., Chen, L. L., Peng, R., Si, P., Feng, J., Li, Y., Lou, J. & Ci, L. High performance graphene oxide nanofiltration membrane prepared by electrospraying for wastewater purification. *Carbon* **130**, 487–494 (2018).

62. Boo, C., Wang, Y., Zucker, I., Choo, Y., Osuji, C. O. & Elimelech, M. High Performance Nanofiltration Membrane for Effective Removal of Perfluoroalkyl Substances at High Water Recovery. *Environmental Science & Technology* **52**, 7279–7288 (2018).
63. Nanofiltration - fumatech GmbH. <https://www.fumatech.com/EN/Membrane-processes/Process%2Bdescription/Nanofiltration/index.html>. (Accessed: 22nd August 2019)
64. Van Der Bruggen, B., Koninckx, A. & Vandecasteele, C. Separation of monovalent and divalent ions from aqueous solution by electrodialysis and nanofiltration. *Water Research* **38**, 1347–1353 (2004).
65. Liu, G., Jin, W. & Xu, N. Graphene-based membranes. *Chemical Society Reviews* **44**, 5016–5030 (2015).
66. Koenig, S. P., Wang, L., Pellegrino, J. & Bunch, J. S. Selective Molecular Sieving through Porous Graphen. *Nature Nanotechnology* **7**, 728 (2012).
67. Grosjean, R., Delacroix, S., Gouget, G., Beaunier, P., Ersen, O., Ihiwakrim, D., Kurakevych, O. & Portehault, D. High pressures pathway toward boron-based nanostructured solids. *Dalton Transactions* **47**, 7634–7639 (2017).
68. Al-zoubi, H., Mohammad, A. W. & Hilal, N. Modelling the Effects of Nanofiltration Membranes properties on system cost Assessment for Desalination Applications system cost assessment for desalination applications. *Desalination* **206**, 215–225 (2007).
69. Crini, G. & Lichtfouse, E. Advantages and disadvantages of techniques used for wastewater treatment. *Environmental Chemistry Letters* **17**, 145–155 (2019).
70. Pintar, A., Batista, J. & Levec, J. Integrated ion exchange/catalytic process for efficient removal of nitrates from drinking water. *Chemical Engineering Science* **56**, 1551–1559 (2001).
71. Víctor-Ortega, M. D., Ochando-Pulido, J. M. & Martínez-Ferez, A. Ion exchange system for the final purification of olive mill wastewater: Performance of model vs. real effluent treatment. *Process Safety And Environmental Protection* **103**, 308–314

- (2016).
72. WasteWater System. WasteWater System: Ion Exchange Application in Wastewater Treatment. <http://www.wastewatersystem.net/2011/08/ion-exchange-application-in-wastewater.html> (2011). (Accessed: 7th October 2018)
 73. Dang, T., Huntsberger, D. S. & Kitteringham, B. A. Using membrane contactors for CO₂ removal to extend resin bed life. *Ultrapure Water* **20**, 20–23 (2003).
 74. Caetano, M., Valderrama, C., Farran, A. & Cortina, J. L. Phenol removal from aqueous solution by adsorption and ion exchange mechanisms onto polymeric resins. *Journal Of Colloid And Interface Science* **338**, 402–409 (2009).
 75. Fu, F. & Wang, Q. Removal of heavy metal ions from wastewaters: A review. in *Journal of Environmental Management* vol. 92 407–418 (2011).
 76. Dabrowski, A., Hubicki, Z., Podko Scielny, P. & Robens, E. Selective removal of the heavy metal ions from waters and industrial wastewaters by ion-exchange method.
 77. Gode, F. & Pehlivan, E. Removal of chromium(III) from aqueous solutions using Lewatit S 100: The effect of pH, time, metal concentration and temperature. *Journal Of Hazardous Materials* **136**, 330–337 (2006).
 78. Bolto, B., Dixon, D. & Eldridge, R. Ion exchange for the removal of natural organic matter. *Reactive And Functional Polymers* **60**, 171–182 (2004).
 79. Tripathi Neha. The Disadvantages of Ion Exchange | Sciencing. <https://sciencing.com/disadvantages-ion-exchange-8092882.html> (2017). (Accessed: 7th October 2018)
 80. Voutchkov, N. Energy use for membrane seawater desalination – current status and trends. in *Desalination* vol. 431 2–14 (2018).
 81. Fang, C. H., Liu, P. I., Chung, L. C., Shao, H., Ho, C. H., Chen, R. S., Fan, H. T., Liang, T. M., Chang, M. C. & Horng, R. Y. A flexible and hydrophobic polyurethane elastomer used as binder for the activated carbon electrode in capacitive deionization. *Desalination* **399**, 34–39 (2016).
 82. Chen, P. A., Cheng, H. C. & Wang, H. P. Activated carbon recycled from bitter-tea

- and palm shell wastes for capacitive desalination of salt water. *Journal Of Cleaner Production* **174**, 927–932 (2018).
83. Li, M. & Park, H. G. Pseudocapacitive Coating for Effective Capacitive Deionization. (2018).
 84. Wang, H. Low-energy desalination. *Nature Nanotechnology* **13**, 273–274 (2018).
 85. Ghaffour, N., Missimer, T. M. & Amy, G. L. Technical review and evaluation of the economics of water desalination: Current and future challenges for better water supply sustainability. *Desalination* **309**, 197–207 (2013).
 86. Lachish, U. Optimizing the Efficiency of Reverse Osmosis Seawater Desalination. in (2002).
 87. Zarzo, D. & Prats, D. Desalination and energy consumption. What can we expect in the near future? *Desalination* **427**, 1–9 (2018).
 88. Kadaj, E. & Bosleman, R. Chapter 11 - Energy Recovery Devices in Membrane Desalination Processes. *Renewable Energy Powered Desalination Handbook* (ed. Gude, V. G.) 415–444 (Butterworth-Heinemann, 2018).
 89. AlMarzooqi, F. A., Al Ghaferi, A. A., Saadat, I. & Hilal, N. Application of Capacitive Deionisation in water desalination: A review. *Desalination* **342**, 3–15 (2014).
 90. Welgemoed, T. J. & Schutte, C. F. Capacitive Deionization TechnologyTM: An alternative desalination solution. *Desalination* **183**, 327–340 (2005).
 91. Jones, E., Qadir, M., van Vliet, M., Smakhtin, V. & Kang, S. The state of desalination and brine production: A global outlook. *Science Of The Total Environment* **657**, 1343–1356 (2019).
 92. Huyskens, C., Helsen, J., Groot, W. J. & De Haan, A. B. Cost evaluation of large-scale membrane capacitive deionization for biomass hydrolysate desalination. *Separation And Purification Technology* **146**, 294–300 (2015).
 93. Almarzooqi, F. A., Al Ghaferi, A. A., Saadat, I. & Hilal, N. Application of Capacitive Deionisation in water desalination: A review. (2014).
 94. Cosin. Desalination Technologies and Economics: CAPEX, OPEX &

- Technological Game Changers. *Mediterranean Regional Technical Meeting Marseille CMI, December 12-14 2016* (2016).
95. Advisian. The Cost of Desalination - Advisian. <https://www.advisian.com/en-gb/global-perspectives/the-cost-of-desalination> (2018). (Accessed: 23rd August 2019)
 96. Blair, J. & Murphy, G. Electrochemical Demineralization of Water with Porous Electrodes of Large Surface Area. (University of Oklahoma, 1960).
 97. Reid, G. W. *Field operation of a 20 gallons per day pilot plant unit for electrochemical desalination of brackish water*. (University of Michigan Library, 1968).
 98. Johnson, A. M. & Newman, J. Desalting by Means of Porous Carbon Electrodes. *Journal Of The Electrochemical Society* **118**, 510–517 (1971).
 99. Farmer, J. C., Fix, D. V., Mack, G. V., Pekala, R. W. & Poco, J. F. Capacitive Deionization of NaCl and NaNO₃ Solutions with Carbon Aerogel Electrodes. *J. Electrochem. Soc. V. Gutmann And E. Vychera, Inorg. Nucl. Chem. Lett. J. Electroanal. Chem* **143**, 159–169 (1996).
 100. Li, H., Gao, Y., Pan, L., Zhang, Y., Chen, Y. & Sun, Z. Electrosorptive desalination by carbon nanotubes and nanofibres electrodes and ion-exchange membranes. *Water Research* **42**, 4923–4928 (2008).
 101. Farmer, J. C., Fix, D. V., Mack, G. V., Pekala, R. W. & Poco, J. F. The use of capacitive deionization with carbon aerogel electrodes to remove inorganic contaminants from water. (1995).
 102. Biesheuvel, P. M., Bazant, M. Z., Cusick, R. D., Hatton, T. A., Hatzell, K. B., Hatzell, M. C., Liang, P., Lin, S., Porada, S., Santiago, J. G., Smith, K. C., Stadermann, M., Su, X., Sun, X., Waite, T. D., van der Wal, A., Yoon, J., Zhao, R., Zou, L., *et al.* Capacitive Deionization -- defining a class of desalination technologies. *arXiv preprint arXiv:1709.05925* (2017).
 103. Andelman, M. & Gregory, W. Charge Barrier Flow-through Capacitor. 1–16 (2004).
 104. Livermore, L., Suss, M. E., Baumann, T. F., Bourcier, W. L., Spadaccini, C. M., Rose, K. A., Santiago, J. G. & Stadermann, M. Capacitive desalination with flow-through

- electrodes Capacitive desalination with flow-through electrodes †. **5**, 11–12 (2012).
105. Jeon, S. Il, Park, H. R., Yeo, J. G., Yang, S., Cho, C. H., Han, M. H. & Kim, D. K. Desalination via a new membrane capacitive deionization process utilizing flow-electrodes. *Energy And Environmental Science* **6**, 1471–1475 (2013).
106. Porada, S., Borchardt, L., Oschatz, M., Bryjak, M., Atchison, J. S., Keesman, K. J., Kaskel, S., Biesheuvel, P. M. & Presser, V. Direct prediction of the desalination performance of porous carbon electrodes for capacitive deionization†. *Energy & Environmental Science* **12**, 3700–3712 (2013).
107. Dykstra, J. E. Desalination with porous electrodes. (Wageningen University, 2018).
108. Jia, B. & Zhang, W. Preparation and Application of Electrodes in Capacitive Deionization (CDI): a State-of-Art Review. (2011).
109. Porada, S., Zhao, R., Van Der Wal, A., Presser, V. & Biesheuvel, P. M. Review on the science and technology of water desalination by capacitive deionization. *Progress In Materials Science* **58**, 1388–1442 (2013).
110. Zhao, R., Van Soestbergen, M., Rijnaarts, H. H. M., Van Der Wal, A., Bazant, M. Z. & Biesheuvel, P. M. Time-dependent ion selectivity in capacitive charging of porous electrodes. (2012).
111. Biesheuvel, P. M., Porada, S., Levi, M. & Bazant, M. Z. Attractive forces in microporous carbon electrodes for capacitive deionization. *Journal Of Solid State Electrochemistry* **18**, 1365–1376 (2014).
112. Arafat, H. A., Franz, M. & Pinto, N. G. Effect of Salt on the Mechanism of Adsorption of Aromatics on Activated Carbon †. (1999).
113. Porada, S., Borchardt, L., Oschatz, M., Bryjak, M., Atchison, J. S., Keesman, K. J., Kaskel, S., Biesheuvel, P. M. & Presser, V. Direct prediction of the desalination performance of porous carbon electrodes for capacitive deionization. *Energy And Environmental Science* **6**, 3700–3712 (2013).
114. Biesheuvel, P. M., Porada, S., Levi, M. & Bazant, M. Z. Attractive forces in microporous carbon electrodes for capacitive deionization. *Journal Of Solid State Electrochemistry* **18**, 1365–1376 (2014).

115. Jia, B. & Zhang, W. Preparation and Application of Electrodes in Capacitive Deionization (CDI): a State-of-Art Review. *Nanoscale Research Letters* **11**, 1–25 (2016).
116. Hou, C. H., Huang, J. F., Lin, H. R. & Wang, B. Y. Preparation of activated carbon sheet electrode assisted electrosorption process. *Journal Of The Taiwan Institute Of Chemical Engineers* **43**, 473–479 (2012).
117. Zou, L., Li, L., Song, H. & Morris, G. Using mesoporous carbon electrodes for brackish water desalination. *Water Research* **42**, 2340–2348 (2008).
118. Wang, G., Qian, B., Dong, Q., Yang, J., Zhao, Z. & Qiu, J. Highly mesoporous activated carbon electrode for capacitive deionization. *Separation And Purification Technology* **103**, 216–221 (2013).
119. Zhao, R., Porada, S., Biesheuvel, P. M. & Van der Wal, A. Energy consumption in membrane capacitive deionization for different water recoveries and flow rates, and comparison with reverse osmosis. *Desalination* **330**, 35–41 (2013).
120. Porada, S., Weingarth, D., Hamelers, H. V. M., Bryjak, M., Presser, V. & Biesheuvel, P. M. Carbon flow electrodes for continuous operation of capacitive deionization and capacitive mixing energy generation †. (2014).
121. Porada, S., Sales, B. B., Hamelers, H. V. M. & Biesheuvel, P. M. Water Desalination with Wires. *J. Phys. Chem. Lett* **3**, (2012).
122. Suss, M. E., Porada, S., Sun, X., Biesheuvel, P. M., Yoon, J. & Presser, V. Water desalination via capacitive deionization: what is it and what can we expect from it? *Energy Environ. Sci* **8**, 2296 (2015).
123. Xu, P., Drewes, J. E., Heil, D. & Wang, G. Treatment of brackish produced water using carbon aerogel-based capacitive deionization technology. *Water Research* **42**, 2605–2617 (2008).
124. Porada, S., Weinstein, L., Dash, R., Van Der Wal, A., Bryjak, M., Gogotsi, Y. & Biesheuvel, P. M. Water desalination using capacitive deionization with microporous carbon electrodes. *ACS Applied Materials And Interfaces* **4**, 1194–1199 (2012).
125. Avraham, E., Noked, M., Bouhadana, Y., Soffer, A. & Aurbach, D. Limitations of

- Charge Efficiency in Capacitive Deionization. *Journal Of The Electrochemical Society* **156**, P157 (2009).
126. Avraham, E., Noked, M., Cohen, I., Soffer, A. & Aurbach, D. The Dependence of the Desalination Performance in Capacitive Deionization Processes on the Electrodes PZC. *Journal Of The Electrochemical Society* **158**, P168 (2011).
 127. Cohen, I., Avraham, E., Noked, M., Soffer, A. & Aurbach, D. Enhanced Charge Efficiency in Capacitive Deionization Achieved by Surface-Treated Electrodes and by Means of a Third Electrode. *J. Phys. Chem. C* **115**, (2011).
 128. Suss, M. E., Biesheuvel, P. M., Baumann, T. F., Stadermann, M. & Santiago, J. G. In Situ Spatially and Temporally Resolved Measurements of Salt Concentration between Charging Porous Electrodes for Desalination by Capacitive Deionization. *Environ. Sci. Technol* **48**, 39 (2014).
 129. Lee, J. B., Park, K. K., Eum, H. M. & Lee, C. W. Desalination of a thermal power plant wastewater by membrane capacitive deionization. *Desalination* **196**, 125–134 (2006).
 130. Liu, Y., Pan, L., Xu, X., Lu, T., Sun, Z. & Chua, D. H. C. Enhanced desalination efficiency in modified membrane capacitive deionization by introducing ion-exchange polymers in carbon nanotubes electrodes. *Electrochimica Acta* **130**, 619–624 (2014).
 131. Dorji, P., Choi, J., Inhyuk, D., Phuntsho, S. & Hong, S. Membrane capacitive deionisation as an alternative to the 2nd pass for seawater reverse osmosis desalination plant for bromide removal. *Desalination* **433**, 113–119 (2018).
 132. Yeo, J. H. & Choi, J. H. Enhancement of nitrate removal from a solution of mixed nitrate, chloride and sulfate ions using a nitrate-selective carbon electrode. *Desalination* **320**, 10–16 (2013).
 133. Zhao, Y., Wang, Y., Wang, R., Wu, Y., Xu, S. & Wang, J. Performance comparison and energy consumption analysis of capacitive deionization and membrane capacitive deionization processes. *DES* **324**, 127–133 (2013).
 134. Zhao, R., Satpradit, O., Rijnaarts, H. H. M., Biesheuvel, P. M. & Van Der Wal, A. Optimization of salt adsorption rate in membrane capacitive deionization. *Water*

- Research* **47**, 1941–1952 (2013).
135. Biesheuvel, P. M., Zhao, R., Porada, S. & van der Wal, A. Theory of membrane capacitive deionization including the effect of the electrode pore space. *Journal Of Colloid And Interface Science* **360**, 239–248 (2011).
 136. Kim, Y. J. & Choi, J. H. Improvement of desalination efficiency in capacitive deionization using a carbon electrode coated with an ion-exchange polymer. *Water Research* **44**, 990–996 (2010).
 137. Lee, J.-Y., Seo, S.-J., Yun, S.-H. & Moon, S.-H. Preparation of ion exchanger layered electrodes for advanced membrane capacitive deionization (MCDI). *Water Research* **45**, 5375–5380 (2011).
 138. Presser, V., Dennison, C. R., Campos, J., Knehr, K. W., Kumbur, E. C. & Gogotsi, Y. The electrochemical flow capacitor: A new concept for rapid energy storage and recovery. *Advanced Energy Materials* **2**, 895–902 (2012).
 139. Hatzell, K. B., Iwama, E., Ferris, A., Daffos, B., Urita, K., Tzedakis, T., Chauvet, F., Taberna, P. L., Gogotsi, Y. & Simon, P. Capacitive deionization concept based on suspension electrodes without ion exchange membranes. *Electrochemistry Communications* **43**, 18–21 (2014).
 140. Sook, K., Cho, Y., Yeon, K., Yang, S., Hee, M. & Kook, D. Applied Surface Science Membrane-spacer assembly for flow-electrode capacitive deionization. *Applied Surface Science* **433**, 437–442 (2018).
 141. Porada, S., Bryjak, M., Van Der Wal, A. & Biesheuvel, P. M. Electrochimica Acta Effect of electrode thickness variation on operation of capacitive deionization. *Electrochimica Acta* **75**, 148–156 (2012).
 142. Zhao, R., Biesheuvel, P. M. & Van Der Wal, A. Energy consumption and constant current operation in membrane capacitive deionization. *Energy And Environmental Science* **5**, 9520–9527 (2012).
 143. Kang, J., Kim, T., Jo, K. & Yoon, J. Comparison of salt adsorption capacity and energy consumption between constant current and constant voltage operation in capacitive deionization. *Desalination* **352**, 52–57 (2014).

144. Chen, Y. A., Fan, C. S. & Hou, C. H. Optimizing the energetic performance of capacitive deionization devices with unipolar and bipolar connections under constant current charging. *Journal Of The Taiwan Institute Of Chemical Engineers* **93**, 201–210 (2018).
145. Dykstra, J. E., Porada, S., van der Wal, A. & Biesheuvel, P. M. Energy consumption in capacitive deionization – Constant current versus constant voltage operation. *Water Research* **143**, 367–375 (2018).
146. Choi, J. H. Comparison of constant voltage (CV) and constant current (CC) operation in the membrane capacitive deionisation process. *Desalination And Water Treatment* **56**, 921–928 (2015).
147. Ahmad, F., Khan, S. J., Jamal, Y., Kamran, H., Ahsan, A., Ahmad, M. & Khan, A. Desalination of brackish water using capacitive deionization (CDI) technology. *Desalination And Water Treatment* **57**, 7659–7666 (2016).
148. Srimuk, P., Halim, J., Lee, J., Tao, Q., Rosen, J. & Presser, V. Two-Dimensional Molybdenum Carbide (MXene) with Divacancy Ordering for Brackish and Seawater Desalination via Cation and Anion Intercalation. *ACS Sustainable Chemistry And Engineering* **6**, 3739–3747 (2018).
149. Kim, Y. J., Hur, J., Bae, W. & Choi, J. H. Desalination of brackish water containing oil compound by capacitive deionization process. *Desalination* **253**, 119–123 (2010).
150. Weinstein Lawrence & Dash Ranjan. *Capacitive Deionisation: Challenges and Opportunities*. http://www.fujifilmmembranes.com/images/DWR_article_1213.pdf (2013). (Accessed: 29th August 2019)
151. Ahmed, M. A. & Tewari, S. Capacitive deionization: Processes, materials and state of the technology. in *Journal of Electroanalytical Chemistry* vol. 813 178–192 (2018).
152. Kwade, A. & Haselrieder, W. Effect of Electrode and Cell Production Steps on Lithium-Ion Battery Cell Performance and Costs. *AABC Europe* (2017).
153. Lu, G., Wang, G., Wang, P. H., Yang, Z., Yan, H., Ni, W., Zhang, L. & Yan, Y. M. Enhanced capacitive deionization performance with carbon electrodes prepared with a modified evaporation casting method. *Desalination* **386**, 32–38 (2016).

154. Seyam, A. M., Oxenham, W. & Theyson, T. *Antistatic and electrically conductive finishes for textiles. Functional Finishes for Textiles: Improving Comfort, Performance and Protection* (Woodhead Publishing Limited, 2014).
155. Akinlabi, E. T. & Akinlabi, S. A. *Friction stir welding of dissimilar metals. Advances in Friction-Stir Welding and Processing* (Elsevier, 2014).
156. Chandra, H., Allen, S. W., Oberloier, S. W., Bihari, N., Gwamuri, J. & Pearce, J. M. Open-source automated mapping four-point probe. *Materials* **10**, 1–17 (2017).
157. Mao, N. Wettability - an overview ScienceDirect Topics. *Advances in Technical Nonwovens* <https://www.sciencedirect.com/topics/materials-science/wettability/pdf> (2016). (Accessed: 14th April 2019)
158. Brunauer, S., Emmett, P. H. & Teller, E. Adsorption of Gases in Multimolecular Layers. *Journal Of The American Chemical Society* **60**, 309–319 (1938).
159. Hanaor, D. A. H., Ghadiri, M., Chrzanowski, W. & Gan, Y. Scalable surface area characterization by electrokinetic analysis of complex anion adsorption. *Langmuir* **30**, 15143–15152 (2014).
160. Arenas-Lago, D., Rodríguez-Seijo, A., Andrade Couce, L. & Vega, F. A. Multianalytical approach for the assessment of toxic element distribution in soils from mine and quarry areas. *Assessment, Restoration and Reclamation of Mining Influenced Soils* 33–62 (Academic Press, 2017).
161. Liu, K., Ostadhassan, M. & Cai, J. Characterizing Pore Size Distributions of Shale. *Petrophysical Characterization and Fluids Transport in Unconventional Reservoirs* 3–20 (Elsevier, 2019).
162. Bogner, A., Jouneau, P.-H., Thollet, G., Basset, D. & Gauthier, C. A history of scanning electron microscopy developments: Towards “wet-STEM” imaging.
163. Bladergroen, B., Hlabano-moyo, B., Bel, M., Nyabanga, S., Dzingwe, B., Bonnet, C., Smith, N. & Cordonnier, M. *CAPACITIVE DEIONIZATION AS A LOW COST DESALINATION TECHNOLOGY*. (2018).
164. Zhang, C., He, D., Ma, J., Tang, W. & Waite, T. D. Faradaic reactions in capacitive deionization (CDI) - problems and possibilities: A review. *Water Research* **128**, 314–

- 330 (2018).
165. Kim, T. & Yoon, J. CDI ragone plot as a functional tool to evaluate desalination performance in capacitive deionization. *RSC Advances* **5**, 1456–1461 (2015).
 166. Dong, Q., Wang, G., Qian, B., Hu, C., Wang, Y. & Qiu, J. Electrospun composites made of reduced graphene oxide and activated carbon nanofibers for capacitive deionization. *Electrochimica Acta* **137**, 388–394 (2014).
 167. Polyvinylidene fluoride | chemical compound | Britannica.com.
<https://www.britannica.com/science/polyvinylidene-fluoride>. (Accessed: 4th November 2019)
 168. Aslan, M., Zeiger, M., Jäckel, N., Grobelsek, I., Weingarth, D. & Presser, V. Improved capacitive deionization performance of mixed hydrophobic/hydrophilic activated carbon electrodes. *Journal Of Physics Condensed Matter* **28**, 114003 (2016).
 169. Liang, Y., Cheng, S., Zhao, J., Zhang, C., Sun, S., Zhou, N., Qiu, Y. & Zhang, X. Heat treatment of electrospun Polyvinylidene fluoride fibrous membrane separators for rechargeable lithium-ion batteries. *Journal Of Power Sources* **240**, 204–211 (2013).
 170. Sun, C. & Feng, X. Enhancing the performance of PVDF membranes by hydrophilic surface modification via amine treatment. *Separation And Purification Technology* **185**, 94–102 (2017).
 171. Sing, K. S. W. Commission on colloid and surface chemistry including catalysis subcommittee on reporting gas adsorption data-reporting physisorption data for gas/solid systems. *Pure & Appl. Chem* **54**, 2201–2218 (1982).
 172. Groen, J. C., Peffer, L. A. A. & Pérez-Ramírez, J. Pore size determination in modified micro- and mesoporous materials. Pitfalls and limitations in gas adsorption data analysis. *Microporous And Mesoporous Materials* **60**, 1–17 (2003).
 173. Gregorio, R. & Capitão, R. C. Morphology and phase transition of high melt temperature crystallized poly(vinylidene fluoride). *Journal Of Materials Science* **35**, 299–306 (2000).
 174. López-de-Uralde, J., Ruiz, I., Santos, I., Zubillaga, A., Bringas, P. G., Okariz, A. & Guraya, T. Automatic morphological categorisation of carbon black nano-aggregates.

International Conference on Database and Expert Systems Applications vol. 6262 LNCS 185–193 (Springer, 2010).

175. Gao, X., Omosebi, A., Landon, J. & Liu, K. Dependence of the Capacitive Deionization Performance on Potential of Zero Charge Shifting of Carbon Xerogel Electrodes during Long-Term Operation. *Journal Of The Electrochemical Society* **161**, E159–E166 (2014).
176. Chen, Z., Zhang, H., Wu, C., Luo, L., Wang, C., Huang, S. & Xu, H. A study of the effect of carbon characteristics on capacitive deionization (CDI) performance. (2018).
177. Zornitta, R. L., Lado, J. J., Anderson, M. A. & Ruotolo, L. A. M. Effect of electrode properties and operational parameters on capacitive deionization using low-cost commercial carbons. *Separation And Purification Technology* **158**, 39–52 (2016).

Appendix A

Different materials and reagents utilised¹⁶³

Chemical/Material	Specifications	Purpose	Supplier
YP50F	Activated carbon 1500-1800 m ² ·g ⁻¹	Electrode ingredient that increases surface area	Kuraray Co. Ltd., Germany
YP80F	Activated carbon 2000-2500 m ² ·g ⁻¹	Electrode ingredient that increases surface area	Kuraray Co. Ltd., Germany
PVDF	Polyvinylidene difluoride	Acts as a binder Provide uniformity in the electrode	Sigma Aldrich Pty. Ltd., South Africa
N,N-DMAC	N,N-Dimethylacetamide, 99.8% purity	Dissolve the binder	Sigma Aldrich Pty. Ltd., South Africa
Super-p CB	Carbon Black	Additive to increase electro-conductivity of the electrode	Alfa Aesar, Germany
NaCl	Sodium Chloride 99.5% purity	To prepare feed solution for desalination experiments	KIMIX, South Africa
JNT45	Carbon substrate, 80 g·m ⁻² area weight	Electro-conductive backbone of the electrode	JNTG Co. Ltd., Korea
SGL 28 AA	Carbon substrate 55 g·m ⁻² area weight	Electro-conductive backbone of the electrode	SGL Carbon, Germany
SGL 29 AA	Carbon substrate 40 g·m ⁻² area weight	Electro-conductive backbone of the electrode	SGL Carbon, Germany
SGL 38 AA	Carbon substrate 75 g·m ⁻² area weight	Electro-conductive backbone of the electrode	SGL Carbon, Germany
SGL 39 AA	Carbon substrate 50 g·m ⁻² area weight	Electro-conductive backbone of the electrode	SGL Carbon, Germany
N₂	Nitrogen gas, 99.999% ultra-high purity	To create an inert environment	Afrox Ltd., South Africa
Fumasep FAA-3-PE-30	Anion exchange membrane	To prevent contamination of the anode during the discharge cycle	Fumatech, Germany
Fumasep E-620-PE	Cation exchange membrane	To prevent contamination of the cathode during the discharge cycle	Fumatech, Germany

Appendix B

List of equipment utilised¹⁶³

Equipment	Specifications	Purpose	Supplier
Autolab	Autolab PGSTAT 8256 potentiostat/galvanostat 100 mA to 10 nA current range	Electrode performance: Chronoamperometry	Metrohm Autolab BV, NL
Micromeritics 3 Flex Surface	1.3×10^{-9} to 1.0 P/P ₀ analysis range 1 micropore port	Electrode development: Surface area & Porosity	Micromeritics, USA
Conductivity meter	Portavo 904 X Knick SE 204 4- electrode sensor measuring range: 0.05 to 500 mS·cm ⁻¹	Electrode performance	Mecosa Pty Ltd, SA
MCDI cell	MCDI cell produced in-house 39 mm x 79 mm area Flow-by mode	Electrode performance	SAIAMC, SA
Milli-Q Integral water	Resistivity 18.2 MΩ·cm Flowrate 2 mL·min ⁻¹ TOC ² ≤5 ppb	Electrode performance: ultrapure water for electrolyte preparation	Merck KGaA, Germany
Rolling Press	MSK-HRP-MR100A Electric precision 4" width rolling press with dual micrometre	Electrode development: slurry infiltration	MTI Corporation, USA
Overhead stirrer	Z2D15	Electrode development: Ink preparation	Ningbo Zhongda Co.,Ltd, China
Devil shaker	Classic Shaker Model number: RD-5153-00 Counter Base	Electrode development: Ink preparation	Red Devil Equipment Co., USA
Holder	Holder for ink preparation, produced in- house	Electrode development: Ink preparation	Wake Engineering, SA
4-Point Probe	4-Point Probe produced in-house	Electrode performance: Conductivity	SAIAMC, South Africa
	Digital multimeter DT9205A	Electrode performance: measures voltage	RS Components, South Africa
	Power Supply EA-PSI 8032-10T	Electrode performance: supplies current	RS Components, South Africa
Ultrasonic bath	Bandelin Sonorex RK 514 BH 325 x 300 x 200 (tank dimensions)	Electrode development: Ultra sonication of electrode ink	Monitoring & Control Laboratories Pty Ltd, SA
Spray coating machine	SONO-TEK ExactaCoat Benchtop Coating Sytem	Electrode development: Electrode ink spraying	Sono-tek Corporation, USA
Peristaltic pump	Watson-Marlow Sci-Q 300	To pump the feed solution through the CDI cell	Dune Engineering, South Africa
Graphtec Cutting pro	FCX2000(VC) 36"×24" 920 mm × 610 mm Max cutting force-Tool 1: 500 gf	To cut electrodes into required area	Graphtec America Inc., USA
Contact angle analyser	Contact angle setup, produced in-house	Electrode performance: Hydrophilicity/hydroph obicity	Wake Engineering, South Africa
	Proline Plus mechanical adjustable volume pipette 20-200 μL	Drop water droplet on electrode	

Appendix C

MCDI cell components and dimensions¹⁶³

<p><i>CDI/MCDI cell top plate</i></p>	<p><i>CDI/MCDI bottom plate</i></p>	<p><i>Gold coated SS contact points</i></p>
<p><i>Graphite current collector</i></p>	<p><i>Carbon electrode</i></p>	<p><i>Spacer</i></p>
<p><i>Lower/Upper gasket, &</i></p>	<p><i>Cation exchange membrane</i></p>	<p><i>Anion exchange membrane</i></p>

Appendix D

List of equipment/components used in assembling the cell¹⁶³

Material/Component	Specifications	Supplier
Bolt & nuts	M5 Bolts and M5 nuts 5 mm inner diameter 53 mm bolt length	Parow bolt and tool, South Africa
Influent/effluent port	Festo Pneumatic straight threaded-to-tube adapter M6 male push in 6 mm	Festo Fittings, South Africa
HDPE top plate	150 × 90 × 25 mm (L × W × H)	Maizey plastics Pty Ltd, South Africa
HDPE bottom plate	150 × 90 × 20 mm (L × W × H)	Maizey plastics Pty Ltd, South Africa
Conductivity meter port (mounted on HDPE top plate)	40 × 40 × 45 (L × W × H) 15.3 inner diameter	SAIAMC, South Africa
Gold coated stainless steel plates	Stainless steel 304/316 38 mm disc diameter 10 mm threaded shaft	Goldfinger Electroplating, South Africa
Graphite	79 × 39 × 2 mm (L × W × H)	SAIAMC, South Africa
Carbon electrode	79 × 39 mm (L × W)	JNT
Silicone gasket	130 × 60 × 1 mm (L×W×H)	Cape Town Rubber, South Africa
Anion exchange membranes	Fumasep FAA-3-PE-30 94-96 % selectivity 0.2-0.7 Ωcm ² specific area resistance	Fumatech, Germany
Cation exchange membranes	Fumasep E-620-PE 98-99 % selectivity 0.3-0.9 Ωcm ² specific area resistance	Fumatech, Germany
PVC/PET spacer	130 × 60 mm Thickness: 0.30 mm and 0.50 mm	Fumatech, Germany
Stainless steel stand	155 × 95 × 40 mm (L×W×H)	WAKE engineering, South Africa
Torque Wrench	2882 Torque Vario-S 0.1-0.6 N.m	Wiha Werkzeuge GmbH, Germany

Appendix E

Excel sheet used to analyse conductivity and current data obtained from the Paraly and Nova software, respectively

CDI Data Analysis E29 #1 11 03 2019 - Excel

FILE HOME INSERT PAGE LAYOUT FORMULAS DATA REVIEW VIEW

AF17

Time	Cond.	T	NCond.	Conc	Cond/dT	Current	Sorp	Cycle	Normalized to 20degC	Sorp**	Cycle	Filtered time	Δ Filtered time
[s]	[μS/cm]	[°C]	[μS/cm]	[mg/l]	[C/s]	[C/s]	#	#	[μS/cm]	#	#	[min]	[min]
0	1774.255	20.0	1775.2	961.3	39.0	2.05E-01	1	1	1776.2	-1.0	1	0	0
0	1.156	1774.255	20.0	1775.2	961.2	39.0	1.76E-01	1	1776.2	-1.0	1	186	186
0	2.169	1774.255	20.0	1775.1	961.2	39.0	1.43E-01	1	1776.2	-1.1	1	366	180
0	3.183	1774.255	20.0	1775.1	961.2	39.0	1.37E-01	1	1776.2	-1.1	1	546	179
0	4.197	1774.255	20.0	1775.1	961.2	39.0	1.25E-01	1	1776.2	-1.1	1	727	182
0	5.211	1774.255	20.0	1775.1	961.2	39.0	1.17E-01	1	1776.2	-1.1	1	907	179
0	6.224	1767.060	20.0	1767.9	957.3	38.8	1.15E-01	1	1776.2	-8.3	1	1086	179
0	7.238	1697.500	20.0	1698.3	919.0	37.3	1.03E-01	1	1776.2	-77.9	1	1267	180
0	8.252	1675.850	20.0	1676.6	907.1	36.8	1.04E-01	1	1776.2	-99.6	1	1446	179
0	9.266	1675.850	20.0	1676.6	907.1	36.8	9.36E-02	1	1776.2	-99.6	1	1628	182
0	10.28	1671.574	20.0	1672.3	904.8	36.7	9.55E-02	1	1776.2	-103.9	1	1807	179
0	11.294	1618.137	20.0	1618.8	875.4	35.6	8.62E-02	1	1776.2	-157.4	1	1988	180
0	12.308	1686.803	20.0	1687.5	913.1	37.1	8.9E-02	1	1776.2	-88.7	1	2165	177
0	13.322	1686.803	20.0	1687.5	913.1	37.1	8.10E-02	1	1776.2	-88.7	1	2346	180
0	14.336	1712.394	20.0	1713.0	927.1	37.6	8.33E-02	1	1776.2	-63.2	1	3423	1078
0	15.35	1951819	20.0	1952.4	938.9	34.1	7.82E-02	1	1776.2	-223.8	1	4156	732
0	16.364	1694.589	20.0	1695.1	917.3	37.2	7.86E-02	1	1776.2	-81.1	1	5227	1072
0	17.379	1694.589	20.0	1695.1	917.3	37.2	7.87E-02	1	1776.2	-81.1	1		
0	18.393	1656.453	20.0	1657.0	896.3	36.4	7.43E-02	1	1776.2	-119.2	1		
0	19.407	1598.789	20.0	1599.2	864.6	35.1	7.59E-02	1	1776.2	-176.9	1		
0	20.421	1624.059	20.0	1624.5	878.5	35.7	7.08E-02	1	1776.2	-151.7	1		
0	21.435	1623.448	20.0	1623.8	878.1	35.7	7.29E-02	1	1776.2	-152.3	1		
0	22.449	1623.448	20.0	1623.8	878.1	35.7	6.74E-02	1	1776.2	-152.3	1		
0	23.463	1623.167	20.0	1623.5	878.0	35.7	7.00E-02	1	1776.2	-152.7	1		
0	24.477	1622.216	20.0	1622.5	877.4	35.6	6.46E-02	1	1776.2	-153.6	1		
0	25.49	1628.428	20.0	1628.7	880.8	35.8	6.73E-02	1	1776.2	-147.5	1		
0	26.504	1628.428	20.0	1628.7	880.8	35.8	6.33E-02	1	1776.2	-147.5	1		
0	27.518	1601.744	20.0	1602.0	866.1	35.2	6.46E-02	1	1776.2	-174.2	1		
0	28.532	1576.642	20.0	1576.9	852.3	34.6	6.37E-02	1	1776.2	-193.3	1		
0	29.546	1643.834	20.0	1644.0	889.2	36.1	6.27E-02	1	1776.2	-132.1	1		
0	30.56	1574.289	20.0	1574.4	851.0	34.6	6.32E-02	1	1776.2	-201.7	1		
0	31.574	1574.289	20.0	1574.4	851.0	34.6	5.95E-02	1	1776.2	-201.7	1		
0	32.588	1621.490	20.0	1621.6	876.9	35.6	6.15E-02	1	1776.2	-154.6	1		
0	33.602	1600.876	20.0	1601.0	865.6	35.2	5.75E-02	1	1776.2	-175.2	1		
0	34.616	1596.520	20.0	1596.6	863.2	35.1	5.97E-02	1	1776.2	-173.6	1		
0	35.631	1596.520	20.0	1596.6	863.2	35.1	5.55E-02	1	1776.2	-173.6	1		
0	36.645	1595.816	20.0	1595.9	862.8	35.1	5.78E-02	1	1776.2	-180.3	1		
0	37.659	1595.458	20.0	1595.5	862.6	35.1	5.44E-02	1	1776.2	-180.7	1		
0	38.673	1596.427	20.0	1596.4	863.1	35.1	5.59E-02	1	1776.2	-179.8	1		
0	39.687	1595.297	20.0	1595.3	862.4	35.0	5.45E-02	1	1776.2	-180.9	1		
0	40.701	1595.297	20.0	1595.3	862.4	35.0	5.42E-02	1	1776.2	-180.9	1		
0	41.715	1598.823	20.0	1598.8	864.4	35.1	0.055084229	1	1776.2	-177.4	1		
0	42.729	1604.495	20.0	1604.4	867.5	35.2	5.25E-02	1	1776.2	-171.8	1		
0	43.743	1578.572	20.0	1578.5	853.2	34.7	0.053955078	1	1776.2	-197.7	1		
0	44.757	1578.572	20.0	1578.5	853.2	34.7	5.08E-02	1	1776.2	-197.7	1		
0	45.771	1601.007	20.0	1600.9	865.5	35.2	5.27E-02	1	1776.2	-175.3	1		
0	46.784	1588.925	20.0	1588.8	858.9	34.9	4.94E-02	1	1776.2	-187.4	1		
0	47.798	1585.183	20.0	1585.0	856.8	34.8	5.15E-02	1	1776.2	-191.2	1		
0	48.812	1585.183	20.0	1585.0	856.8	34.8	4.84E-02	1	1776.2	-191.2	1		

Step 1
Fill in the EXPERIMENTAL DETAILS below and COPY and PASTE converted raw data on Time, Cond, Temp and Current in the Yellow fields on the right.

EXPERIMENTAL DETAILS

ELECTRODE CODE:	NS-I29-NS-YP80-INT45
Year of experiment	2019
Month of experiment	March
Day of experiment	11
File name	CDI E29-NS-I29-NS-YP80
Total dry electrode weight:	0.7947 [g]
Electrode Support weight:	0.5246 [g]
Active electrode weight:	0.2701 [g]
Feed concentration:	961.8138 [mg/L]
Flow rate	9 [rpm]
Flow rate	0.22 [mL/s]
Flow rate	0.21 [mg NaCl/s]
Length of the 7h ads cycle	380 s
NaCl input during 7h Ads cycle	37.44 [mg NaCl]
Ads fraction 7h Ads cycle	0.113
NaCl ads during 7h ads cycle	4.22 [mg NaCl]
SAC (7h ads cycle)	15.64 [mg/g]
NaCl des during 6h des cycle	6.78 [mg NaCl]
SAC (6h des cycle)	25.11 [mg/g]
Length of the mSAC ads cycle	732
NaCl input during 7h Ads cycle	151.86 [mg NaCl]
Ads fraction mSAC Ads cycle	0.049
NaCl ads during 7h ads cycle	7.42 [mg NaCl]
mSAC	27.49 [mg/g]
Torque	0.2 [Nm]

RESULTS

mSAC	27.487 [mg/g]
SAC 7h Ads cycle	15.642 [mg/g]
Ads Salt (based on conductivity m)	0.127 [mmol]
Adsorption charge (based on curr)	0.187 [mmol]

DATA ANALYSIS

sorp n°	Area Cou	Area C/m	Des time	Ads time	Acc Charge [C]
1	-27690	326818	186	186	8.49
2	45248	316161	180	180	-8.10
3	-34626	314385	179	179	10.01
4	54053	317937	182	182	-9.47
5	-36296	314385	179	179	10.22
6	53637	314385	179	179	-9.87
7	-35404	316161	180	180	10.08
8	53051	314385	179	179	-9.91
9	-35832	317937	182	182	10.26
10	56236	314385	179	179	-10.16
11	-36391	316161	180	180	10.29
12	56316	310832	177	177	-10.26
13	-35678	316161	180	180	10.32
14	75424	1888083	1078	1078	-13.62
15	-62695	1282405	732	732	18.06
16	86703	1877426	1072	1072	-14.98

Conductivity and current vs time

